Master Mechanical Engineering
Engineering Fluid Dynamics, 469
Graduation Assignment 2-B Energy

Validation of Taylor's Frozen Turbulence hypothesis for simplified wind modeling

Version 1, 12/04/2025

Maxim C. Peters (s1577220)

01/11/2023 - 29/04/2025, 40 EC

University of Twente supervisor:
dr.ir. Arne van Garrel

2-B Energy supervisors:
ir. Gerardo González Miranda
ir. Martijn Wilpshaar

UNIVERSITY OF TWENTE.

2BENERGY

This report is confidential until 07/10/2025

Abstract

Wind turbines constantly react and adjust their blades to changes in the incoming wind which are detected through monitoring the measured blade loading and rotor speed. Accurate and real-time predictions of the flow allow for more pro-active behavior resulting in improved efficiency and lowered blade loading. In previous research a simplified wind model has been constructed aiming to predict the short-term incoming wind field. This research focuses on validating the most important underlying assumption: Taylor's Frozen Turbulence hypothesis. Using Large Eddy Simulation data, several cases of varying atmospheric stability and mean wind speed were analyzed. The analysis mostly focuses on the longitudinal cross-correlation at the delay where the turbulent perturbations would arrive if they were advected with the mean flow. The analysis is applied to the entire temporal velocity signal, and on velocity signals where a specific frequency band of interest is isolated through a coherence analysis. Estimates for the validity distance, serving as a rough guideline, are provided based on several criteria: a cut-off cross-correlation, an auto-correlation cut-off and the integral length scale.

Contents

Nomenclature

Abbreviations and acronyms

ABL	Atmospheric Boundary Layer
DNS	Direct Numerical Simulation
IEC	International Electrotechnical Commission
IPC	Individual Pitch Control
LES	Large-Eddy Simulation
LiDAR	Light Detection and Ranging
RANS	Reynolds-Averaged Navier-Stokes
SFS	Subfilter-scale
TFTH	Taylor's Frozen Turbulence Hypothesis
TKE	Turbulence Kinetic Energy
UKF	Unscented Kalman Filter

Mathematical notation and operators

$\bar{\square}$	Mean
$\breve{\square}$	Non-dimensionalized variable
$\Delta\square$	Finite difference
$\frac{\partial\square}{\partial\square}$	Partial derivative
$\frac{\mathrm{D}\square}{\mathrm{D}\square}$	Material derivative
$\frac{\mathrm{d}\square}{\mathrm{d}\square}$	Derivative
$\hat{\square}$	Characteristic scale parameter
$\mathcal{F}$	Fourier transform
$\sigma_\square$	Standard deviation
$\square'$	(Turbulent) fluctation
$\square^\Delta$	Subfilter-scale quantity
$\square_0$	Constant or reference quantity
$\tilde{\square}$	Filtered quantity
$\underline{\underline{\square}}$	Matrix, 2^{nd}-order tensor
$\underset{\sim}{\square}$	Vector, 1^{st}-order tensor

Constants and variables (Latin symbols)

$\mathcal{V}$	Specific volume	m^3/kg
$\underline{\underline{R}}$	Rigid-body rotation tensor	s^{-1}
$\underline{\underline{S}}$	Strain-rate tensor	s^{-1}
$\underset{\sim}{u}$	Velocity vector	m/s
$\underset{\sim}{V}$	Velocity vector in planetary reference frame	m/s
a	Azimuth	
c_p	Specific heat capacity at constant pressure	J/(kg·K)
C_s	Smagorinsky coefficient for the SFS-stress	
c_v	Specific heat capacity at constant volume	J/(kg·K)
D_s	Smagorinsky coefficient for the SFS-heat flux	
E	Energy	J
e	Specific internal energy	J/kg
e_k	Specific kinetic energy	J/kg
F	Body force	N
f	Frequency	Hz
f	Specific force, acceleration due to body force	$\mathrm{m/s}^2$
g	Gravitational acceleration	$\mathrm{m/s}^2$
h	Specific enthalpy	J/kg
I	Turbulence intensity	
k	Specific turbulence kinetic energy	$\mathrm{m}^2/\mathrm{s}^2$
k_t	Thermal conductivity	W/(m·K)
L	Flow length scale	m

l_0	Length scale of large eddies	m	u, u_1	Longitudinal velocity	m/s
L_x	Integral length scale (longitudinal)	m	u_*	Friction velocity	m/s
N	Quantity		u_0	Velocity scale of large eddies	m/s
P	Total kinematic pressure	m^2/s^2	u_η	Kolmogorov velocity scale	m/s
p	Pressure, mechanical pressure	N/m^2	u_p	Phase speed	m/s
P^*	Modified kinematic pressure	m^2/s^2	v, u_2	Transverse velocity	m/s
p^*	Modified pressure	N/m^2	w, u_3	Vertical velocity	m/s
Q	Volumetric heat	W/m^3	x, x_1	Longitudinal length	m
q	Heat flux	W/m^2	y, x_2	Transverse length	m
R	Specific gas constant	J/(kg·K)	z, x_3	Vertical length	m
$R_{\square,\square}$	Covariance (velocity)	m^2/s^2	Eu	Euler number	
S	Spectral density	(m/s)/Hz	Fr	Froude number	
T	Temperature	K	Re	Reynolds number	
t	Time	s	Ri_B	Bulk Richardson number	
T_x	Integral time scale (longitudinal)	s	Ro	Rossby number	

Constants and variables (Greek symbols)

α	Thermal diffusivity	m^2/s	ϕ	Phase	
β	Thermal expansion coefficient	K^{-1}	ρ	Density	kg/m^3
Δ	LES cutoff length scale	m	$\rho_{\square,\square}$	Correlation coefficient	
δ_{ij}	Kronecker delta		τ	Delay	s
η	Kolmogorov length scale	m	τ_0	Time scale of large eddies	s
γ^2	Magnitude-squared coherence		τ_η	Kolmogorov time scale	s
κ	Wavenumber	m^{-1}	θ	Potential temperature	K
λ	Wavelength	m	$\underline{\sigma}$	Stress tensor	N/m^2
μ	Dynamic viscosity	kg/(m·s)	$\underline{\tau}$	Shear stress tensor	N/m^2
ν	Kinematic viscosity, momentum diffusivity	m^2/s	$\underline{\tau}^\Delta$	Deviatoric part of the SFS-stress tensor, residual stress tensor	m^2/s^2
ν_θ	Eddy thermal diffusivity	m^2/s	$\underset{\sim}{\Omega}$	Rotation vector	s^{-1}
ν_T	Turbulent eddy viscosity	m^2/s	$\underset{\sim}{\omega}$	Vorticity	s^{-1}
ω	Angular velocity	s^{-1}	ε	Specific energy dissipation rate	m^2/s^3
ϕ	Latitude		ε_{ijk}	Levi-Civita symbol	

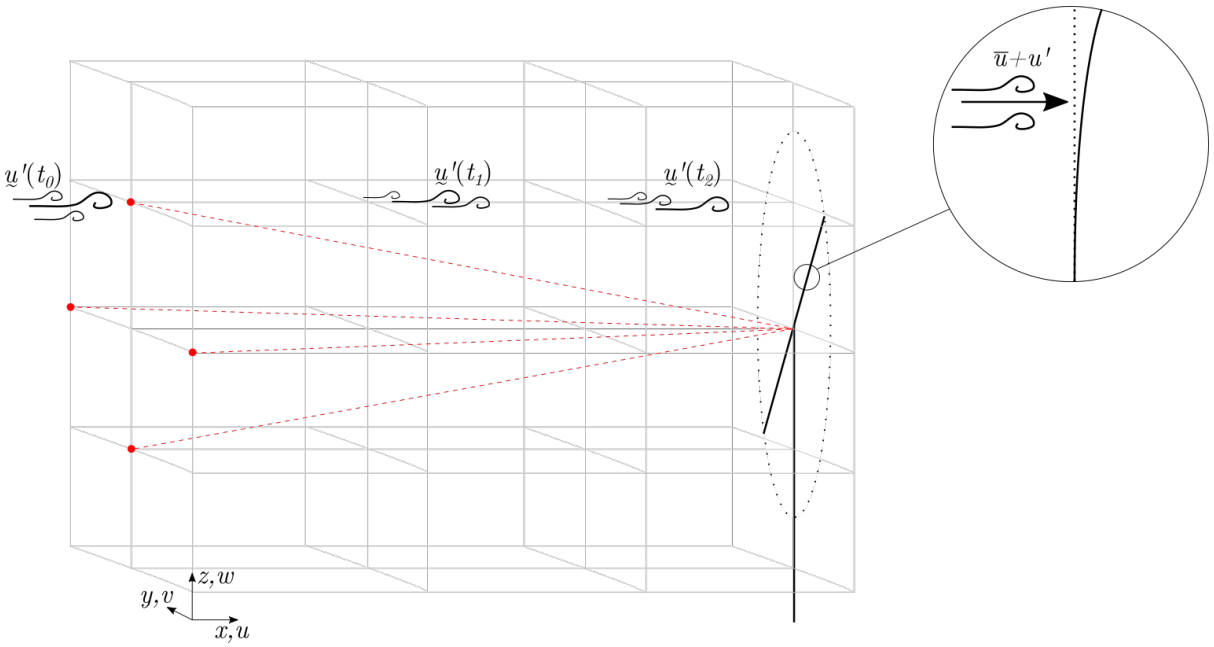

Figure 1.1: Schematic representation of the wind measurement and prediction

1 Introduction

With the European Union aiming for climate-neutrality in 2050 through the European Green Deal[1], the need for renewable energy is ever-present. Renewable energy sources like wind energy are a vital part of this mission. In 2024 around 9% of the global electricity is produced by wind energy and is forecast to increase to 12% by 2028[2]. Continuous improvements to wind turbines and their supporting systems increase their efficiency, reliability and economic viability. Whether these changes are small and gradual or large and sudden, their influence will not be negligible purely due to the size of the wind energy industry.

One possible area of improvement is in more accurately predicting the incoming wind. As the flow is rarely constant and homogeneous, local changes in the flow velocity impact the loading and energy output of the turbine. Figure 1.1 shows a schematic representation of the evolving wind perturbations, $\underset{\sim}{u}'(t)$, approaching the turbine and increasing the load on the blades. Modern wind turbines typically have individual pitch control (IPC) which allows each blade to be rotated depending on the incoming flow, effectively changing the angle of attack of the airfoil[3]. This can reduce the forces on the blades and increase the power output, allowing for cheaper blades due to a reduced maximum loading of the blades for a similar or higher power output. IPC-controllers generally react indirectly to the incoming flow by monitoring the measured blade loading and rotor speed. In order to improve these pitch controllers the incoming flow must be known or at least accurately predicted. Creating a system that can provide these predictions in real-time is non-trivial due to the complexity of the flow, the large region of interest, response time of the pitching systems and measurement difficulty. All these factors must taken into account, because making no prediction is better than a false prediction.

Pitching systems typically have a pitch rate in the order of only several degrees per second and therefore have a certain response time[4]. This requires a wind prediction model to look ahead in time and, consequently, looking ahead in space, as shown by the red measurement points in Figure 1.1. Upstream wind measurements should be combined with a wind evolution model to provide the necessary lead time. LiDAR (Light Detection And Ranging) systems are able to measure wind velocity at a distance and are therefore a promising measurement system. It is, however, not without disadvantages or challenges. LiDAR suffers from the cyclops issue as they only measure the velocity in the direction of the beam. They are therefore unable to decompose the measured velocity in a longitudinal and transverse component with regards to the turbine. This effect can be mitigated

pre-emptively or after the fact. By using multiple LiDAR systems that measure from significantly different locations the cyclops issue can be reduced or completely solved. Otherwise, a model must be applied to the measurement to construct an estimate of the velocity components. In its most basic form this involves measuring several points and assuming an equal transverse velocity to be able to decompose the measured radial velocities.

A measurement system in itself is not enough to provide an accurate representation of the flow on the rotor plane. The upstream measurements do not match with the flow on the rotor plane due to evolution of the wind field, as indicated by the evolving eddies in Figure 1.1. Gusts, wind direction changes and turbulence are some of the effects that can greatly alter the flow as represented by the upstream measurements compared to the flow once it reaches the rotor plane. Another important effect is the influence of the turbine on the flow upstream as the turbine acts as an obstacle in the flow. This blockage effect or turbine induction must be taken into account to accurately translate the measurements to a wind estimation.

Many models have been developed and researched in order to accurately and efficiently predict the wind field. These models originate from a wide range of approaches; in varying degrees they have a basis in fluid dynamics or are more based on signal processing. The complexity of existing models varies by just as much.

Prediction models that mostly stem from signal-processing are Dunne et al.[5] and Bossanyi[6]. Both constructed a feed-forward control system based on LiDAR. The latter also aimed to include wind evolution through adding a de-correlation to the coherence functions. Guillemin et al.[7] based their approach on longitudinal and transverse correlation in combination with a discrete-time Kalman filter to solve the optimization problem of combining measurements, spatial and temporal relations. Machine-learning is employed by Stock-Williams et al.[8] through the use of a Gaussian Process Regression with jointly normally distributed variables. Sagredo et al.[9] reconstruct a wind field purely based on the LiDAR measurements and an inverse-distance-weighting interpolation. The model constructed by Borraccino et al.[10] is more based on fluid dynamics. It consists of a a stationary, homogeneous flow model based on wind shear profiles and a simple induction model.

Another model with a foundation in fluid dynamics is a model by Towers and Jones[11]. In previous research[12] a model based on this research was constructed. In its core the model is a system of nonlinear advection equations that are computed with a first-order implicit discretization scheme. These equations are derived from the Navier-Stokes equations and simplified through a series of assumptions. An Unscented Kalman Filter (UKF) is used to propagate the equations in time. The filter compares and corrects its predictions based on the LiDAR measurements it receives in real-time. The model contains a plethora of parameters that can be tuned in order to improve the accuracy, complexity and computation cost of the model.

However, at a fundamental level the accuracy of the model depends greatly on the validity of the assumptions made. Making an assumption without verifying whether it can reasonably be made can have large consequences, potentially invalidating the predictions. Validation of these assumptions starts with determining which assumptions have the potential to not be applicable in the intended environment. A method or validation strategy can then be conceived; some assumptions are not very restrictive and can be validated based on existing literature, others must be validated for the specific use-case using measurements or detailed simulations. Ideally the validation provides a specific operation envelope where, fundamentally, the model can be used. The aforementioned wind model constructed in previous research formed the basis of this thesis, but the results could apply to any other model making similar assumptions.

2 Atmospheric boundary layer

The system of equations used in the simplified wind model was derived through applying a series of assumptions to the fundamental equations of fluid dynamics, the Navier-Stokes equations[12]. After assuming the fluid to be Newtonian, isotropic and incompressible the Navier-Stokes equations are specified for the atmospheric boundary layer (ABL):

Continuity:
$$\frac{\partial u_j}{\partial x_j} = 0 \tag{2.1}$$

Momentum:
$$\frac{\partial u_i}{\partial t} + u_j \frac{\partial u_i}{\partial x_j} = -\frac{1}{\rho_0}\frac{\partial p^*}{\partial x_i} + \frac{\partial}{\partial x_j}\left(\nu\left(\frac{\partial u_i}{\partial x_j} + \frac{\partial u_j}{\partial x_i}\right)\right) + \delta_{i3} g \left(\frac{\theta - \theta_0}{\theta_0}\right) + f_{Cor,i} + f_i \qquad \text{for } i = 1, 2, 3 \tag{2.2}$$

Potential temperature:
$$\frac{\mathrm{D}\theta}{\mathrm{D}t} = \frac{1}{\rho_0 c_p}\left(\frac{p_0}{p}\right)^{R/c_p}\left(-\frac{\partial q_j}{\partial x_j} + \tau_{ij}\frac{\partial u_i}{\partial x_j} + Q\right) \tag{2.3}$$

Appendix A.1 shows some useful forms of the Navier-Stokes equations and Appendix A.2 shows the complete derivation of the ABL-equations.

These ABL-equations capture the important transport phenomena in the region of the atmosphere where the earth's surface has a direct influence on the flow[13]. Friction with the surface, terrain features and heat transfer to or from the surface are examples of such influences. The affected flow layer thickness is in the order of one kilometer and, as such, wind turbines, with a hub height in the order of 100 meters, are located decidedly inside this region.

The momentum equation (Equation 2.2) contains the advection terms on the left and a number of forcings on the right. These forcing terms include, from left to right, the influence of pressure and shear stress, but also a buoyancy term and the Coriolis force imparted by the earth's rotation. Any other forcing terms are contained in the catch-all term f_i and can be specified when they are required. The effect of buoyancy is one of the driving forces of turbulence in the ABL. The sun heats the earth's surface during the day which transfers heat to the contacting air causing the warmer air to rise in the surrounding colder, and therefore less dense, air. However, the ABL-equations are derived using the incompressibility assumption and therefore prohibiting any flow effects caused by density fluctuations. This paradox is usually avoided by assuming the Boussinesq approximation: density variations are only allowed in the gravity/buoyancy term. The buoyancy is represented by a difference in potential temperature and gravity is included in the modified pressure.

Equation 2.3 shows the terms influencing the potential temperature of a flow parcel; conductive heat transfer through the boundary, viscous heating and a catch-all volumetric heating term. Heat transferring from or to the earth's surface is represented by the first term on the right.

These forcing terms can generate turbulence in the flow; solar heating causes large eddies of buoyant convective air to rise and mix, viscous effects cause a wind shear, obstacles can introduce turbulent wakes or large-scale winds can introduce pressure-gradients. These same terms can also act to destroy or reduce turbulent eddies; viscous effects dissipate turbulent kinetic energy to progressively smaller scales converting it to heat, and buoyancy can also act as a restoring force by opposing convective motions[13].

In order to determine whether the dominant terms will generate or counteract turbulence, the atmosphere is usually classified based on its (static) stability. Unstable or convective atmospheric stability causes the flow to become or remain turbulent. Stable atmospheric stability forces a flow to eventually become or remain laminar. The potential temperature profile is an indicator of the atmospheric stability as it shows the lapse rate and consequently whether buoyancy will act as a turbulence-generating or -stabilizing force[13].

3 Wind model

For the simplified wind model to be run in real-time, further simplifications to the ABL-equations are required. The conservation of energy equation for an incompressible fluid, as represented by the potential temperature equation (Equation 2.3), can be decoupled from the continuity and momentum equation if the flow can be considered inviscid or the kinematic viscosity can be considered to be independent of temperature.

Through applying a scale analysis and only maintaining the characteristic terms, the dominant effects are captured and any other effects are neglected. Appendix A.3 shows the derivation starting with non-dimensionalizing the ABL-equations and applying the characteristic scale parameters as shown in Tables 3.1-3.2. Note that the kinematic viscosity is listed in the table of constants, as the fluctuation due to temperature changes is in the order of 10^{-6} m^2/s in the temperature range of interest and, as such, does not influence the result of the scale analysis.

Table 3.1: Constants (orders of magnitude)

ρ_0	$\sim 10^0$	kg/m^3	density (air)
ν	$\sim 10^{-5}$	m^2/s	kinematic viscosity (air)
g	$\sim 10^1$	m/s^2	gravitational acceleration
2ω	$\sim 10^{-4}$	rad/s	planetary rotation speed

Table 3.2: Characteristic scale parameters

$\hat{x}$	$\sim 10^2$	m	longitudinal length scale
$\hat{y}$	$\sim 10^2$	m	transversal length scale
$\hat{z}$	$\sim 10^1$	m	vertical length scale
$\hat{u}$	$\sim 10^1$	m/s	longitudinal velocity scale
$\hat{v}$	$\sim 10^1$	m/s	transverse velocity scale
$\hat{w}$	$\sim 10^{-2}$	m/s	vertical velocity scale
$\hat{p}^*$	$\sim 10^1$	Pa	modified pressure fluctuation scale
$\left(\frac{\hat{\delta\Theta}}{\Theta}\right)$	$\sim 10^{-1}$	–	relative temperature fluctuation scale
$\hat{t}$	$\sim \hat{x}/\hat{u}$	s	time scale

The scale analysis leads to the two-dimensional non-linear advection equations which form the core of the wind model:

$$\frac{\partial u_i}{\partial t} + u_j \frac{\partial u_i}{\partial x_j} = 0 \qquad \text{for } i = 1, 2 \tag{3.1}$$

Compared to the ABL-equations (Equations 2.1-2.3) the pressure-, viscous- and buoyancy terms have been neglected and the vertical velocity is also gone, effectively neglecting subsidence. Only the advection terms in the horizontal plane remain. The potential temperature equation is also decoupled from the continuity and momentum equation due to neglecting the viscous effects. Furthermore, any turbulent structures are assumed to be advected with the mean flow without any evolution through Taylor's frozen turbulence hypothesis.

These assumptions form the basis of the model and must be validated in order for the model to be considered representative. In the previous study these assumptions were considered valid based on available literature. Any assumptions made to derive the ABL-equations, like incompressibility, will not be further investigated as they are deemed sufficiently covered by existing research. This report focuses on the validation of the most fundamental assumption made in the wind model: Taylor's Frozen Turbulence Hypothesis.

Flow characterization using dimensionless numbers

Based on the parameters of Tables 3.1-3.2, the flow can be characterized using a number of dimensionless numbers. These dimensionless numbers give an insight in the dominant effects in the flow. This is taken from the previous study[12] and shown here again.

- The Euler number is the ratio of pressure forces to inertial forces. It can also be viewed as the ratio between the static pressure and the dynamic pressure:

$$\mathrm{Eu} = \frac{\text{pressure forces}}{\text{inertial forces}} = \frac{\hat{p}^*}{\rho_0 \hat{u}^2} \sim \frac{10^1}{10^0 \cdot (10^1)^2} = 10^{-1} \tag{3.2}$$

  The inertial forces are therefore more important than the pressure forces.

- The Reynolds number is the ratio between the inertial forces and the viscous forces:

$$\mathrm{Re}_{\hat{x}} = \frac{\text{inertial forces}}{\text{viscous forces}} = \frac{\rho_0 \hat{u}\hat{x}}{\mu} = \frac{\hat{u}\hat{x}}{\nu} \sim \frac{10^1 \cdot 10^2}{10^{-5}} = 10^8 \tag{3.3}$$

  The inertial forces are clearly much more important than the viscous forces.

- The Rossby number is the ratio between the inertial forces and the Coriolis force:

$$\mathrm{Ro} = \frac{\text{inertial forces}}{\text{Coriolis forces}} = \frac{\hat{u}}{f\hat{x}} = \frac{\hat{u}}{2\omega \sin(\phi)\hat{x}} \sim \frac{10^1}{10^{-4} \cdot 10^2} = \frac{10^3}{\sin(\phi)} \tag{3.4}$$

  As $\sin(\phi)$ depends on latitude, the magnitude of the Rossby number can vary. It will range from $10^3 \to \infty$ for the possible values of $\sin(\phi)$. This shows that the inertial forces are much more important than the Coriolis force.

- The Froude number only appears in the vertical momentum equation and is the ratio between the inertial forces and the gravitational forces:

$$\mathrm{Fr} = \frac{\text{inertial forces}}{\text{gravitational forces}} = \frac{\hat{u}}{\sqrt{g\hat{x}}} \sim \frac{10^1}{\sqrt{10^1 \cdot 10^2}} = 10^{-1/2} \tag{3.5}$$

  The gravitational forces are more important than the inertial forces in the vertical momentum equation.

4 Wind data

In order to validate the assumptions underlying the simplified wind model, representative wind field data is needed. This requires understanding what options are available to obtain this data and what constitutes representative data and which flow effects must be present in this data in order to be suitable as validation data.

4.1 Measurements vs. simulations

Wind field data can generally be acquired in two ways; through real-world measurements or through utilizing a much more accurate simulation model. Either method has advantages and disadvantages. In theory, real measurements offer the most accurate representation of the flow at the measurement locations and are the easiest to use for specific locations. This immediately presents one of the major drawbacks: the very limited control over the environment and difficulty of isolating specific influences on the flow and maintaining of generality. Other issues are the influence of the measurement device on the flow and measurement noise, though these issues may be mitigated if properly prepared for. The last major drawback of real measurements is the limited number of spatial measurements that can realistically be obtained at the same time instant. It is practically impossible to obtain spatially dense measurements over a sizeable area. Attempting to do so risks increasing the effect of the measurement devices on the actual flow or being prohibitively expensive. The limited amount of spatial data then makes statistical relevance an important aspect of the research.

The other approach to obtain wind data consists of utilizing higher-accuracy and -complexity numerical simulations. These simulations should capture more effects and model the flow better compared to the simplified wind model. To validate a number of assumptions, it is, of course, essential that the higher-complexity simulation does not make use of these assumptions. Compared to real-life measurements, simulations allow unparalleled control in terms of eliminating external factors, isolating specific effects and data quantity. The pitfalls of simulations are inherent; there is a risk of creating non-physical flows if the wrong simulation type is chosen or its setup is wrong. Making the correct choice of simulation type and settings is vital to ensure the data is usable and all important effects are captured. The trade-off with simulations of higher accuracy and rigor is usually their computation time. For the current research, where wind data with high fidelity in spatial and temporal terms is required, using a higher-accuracy simulation is preferred.

Validating Taylor's frozen turbulence hypothesis for use in the wind model requires the simulation type to be able to represent turbulence to an appropriate degree. Due to the pitch rate of a typical wind turbine pitching system and the limited energy contained in high-frequency turbulent structures, the large-scale turbulent structures are of interest for the validation. Not all simulation types are able to provide the sufficient data. Choosing the right simulation type requires understanding the nature and structure of turbulence and which simulation types are able to represent turbulence in some capacity.

Nature and structure of turbulence

In contrast to most laminar flows, turbulent flows are difficult to solve due to their unstable nature. Small disturbances in laminar flows are dissipated through viscous effects ensuring the stability of the flow. When these viscous effects are no longer strong enough to dissipate small disturbances, these disturbances grow into unstable and chaotic flow patterns, eventually leading to a fully turbulent flow. The Reynolds number is the indicator of a flow's stability behavior. As shown in the previous section (Equation 3.3), it is the ratio between the inertial forces and the viscous forces. The inertial forces supply the flow with kinetic energy driving and sustaining the unstable, swirling motions called eddies, which are counteracted by the viscous forces. For high Reynolds numbers, where the inertial forces dominate, flows are or eventually become turbulent. The critical Reynolds number, above which flows transition to turbulent flows, lies between $2 \cdot 10^3$ and 10^6, depending on the specific flow[14].

Turbulence is characterized by being chaotic, diffusive, dissipative and rotational. The chaotic nature makes it difficult to solve the flow deterministically, but time-averaged or statistical quantities can be derived. The diffusivity of turbulence entails rapid mixing and increased rates of mass-, momentum- and heat transfer. This is realized through the characteristic structure of turbulence; the flow consisting of eddies of varying length- and time scales swirling and rapidly mixing the fluid. These eddies have non-zero vorticity that increases with strain-rate, known as vortex stretching. The stretching of eddies in one direction causes them to shrink in the other two and eventually pinch into several smaller-size eddies (see Appendix A.1.3). Vortex stretching is crucial to the energy transfer of the larger-scale eddies to the smaller sizes. When the eddies get progressively smaller, the viscous effects become more important; the kinetic energy contained in the eddies gets dissipated to internal energy through molecular viscosity.

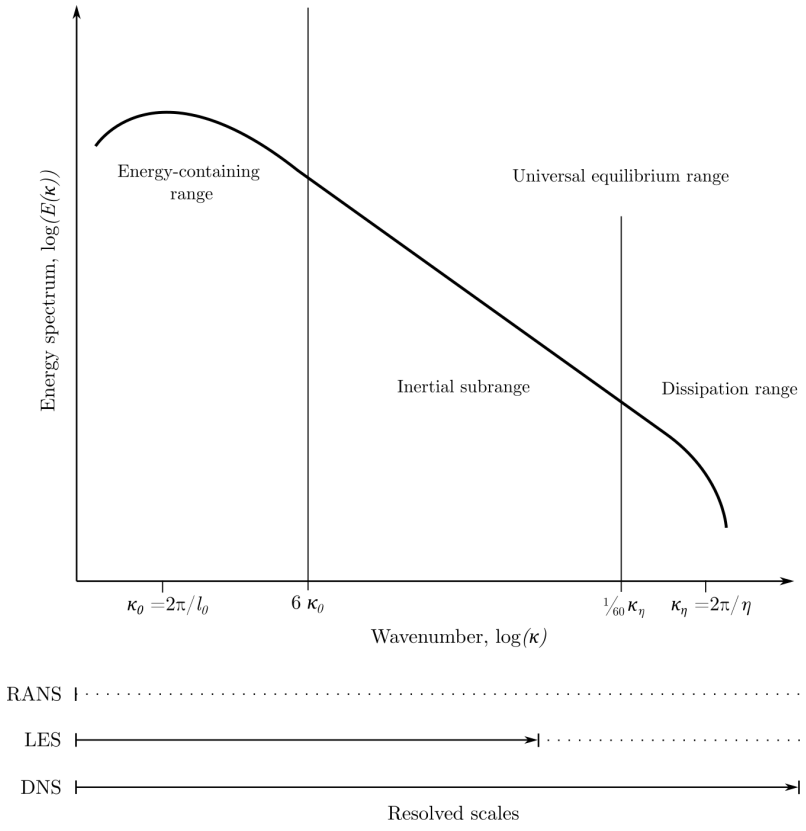

Figure 4.1: Turbulent kinetic energy spectrum

Figure 4.1 shows the aforementioned structure of turbulence in high-Reynolds-number flows through the turbulence energy spectrum. It shows how kinetic energy is transferred from the large-scale eddies towards the smaller sizes in the so-called energy cascade. The spectrum can be divided into three distinct regions based on three Kolmogorov hypotheses[15]:

1. The *energy-containing range* consists of the largest-scale eddies containing the bulk of the kinetic energy. In this region turbulent kinetic energy is produced. These eddies, with length scale l_0, are comparable to the flow scales, L, and are greatly affected by the boundary conditions of the flow. Their velocity scale is in the order of the root-mean-square of the turbulent velocity fluctuations. This region shows highly anisotropic behavior and the Reynolds number of these eddies is very large, meaning this region is practically inviscid[15].

2. Based on Kolmogorov's hypothesis of local isotropy and of similarity, there must be a region where, due to chaotic scale reduction, the turbulent motions are statistically isotropic and with a universal form based solely on the kinematic viscosity, ν, and the energy dissipation rate, ε. This is the *dissipation range* containing the small-scale eddies characterized by the Kolmogorov scales; the Kolmogorov length and velocity scales, η and u_η respectively, are both defined in terms of the kinematic viscosity and dissipation rate. These scales are small enough such that their Reynolds number is low, indicating a viscosity-dominated region where kinetic energy is dissipated to internal energy. The ratios between the large-eddy scales and the Kolmogorov scales can be determined, based on the dissipation rate, to be[15]:

$$\frac{\eta}{l_0} \sim \mathrm{Re}^{-3/4}, \qquad \frac{u_\eta}{u_0} \sim \mathrm{Re}^{-1/4}, \qquad \frac{\tau_\eta}{\tau_0} = \frac{\eta/u_\eta}{l_0/u_0} \sim \mathrm{Re}^{-1/2} \tag{4.1}$$

3. In-between the energy-containing range and the dissipation range must be separate region based on Kolmogorov's second hypothesis on similarity. This region, the *inertial subrange* should show a universal form and be determined solely by the dissipation rate. Both the inertial subrange and the dissipation range have a universal form and together constitute the *universal equilibrium range*, where eddies are small enough to be able to return to a dynamic equilibrium with the energy transferred to them by the large-scale eddies. The inertial subrange is still practically inviscid and, just like the in the energy-containing range, kinetic energy is transferred to smaller scales through vortex stretching. As there is no sink of kinetic energy, all energy transferred to this range must also be transferred out of this range (to the dissipation range), explaining why this region is defined by only the dissipation range. The energy spectrum follows a power law in this region[15]:

$$E(\kappa) \sim \varepsilon^{2/3}\kappa^{-5/3} \tag{4.2}$$

   The inertial subrange length scales span roughly between $\frac{1}{6}l_0$ and 60η[15].

4.2 Simulation types

Several simulation options will be discussed in order to determine the best fit. Most of them solve the Navier-Stokes equations for the mean flow and capture turbulence in some way.

Direct Numerical Simulations (DNS) computes turbulent flows by solving the complete Navier-Stokes system. It is therefore the most accurate simulation. This accuracy comes at a cost: potentially extreme computation times. In order to correctly solve the Navier-Stokes system for a turbulent flow, all relevant scales of the flow must be represented; all the way down to the Kolmogorov scales. For some turbulence cases like wall flows, the relevant scales can be even smaller[16]. As shown by Equation 4.1, these scales are inversely proportional to the Reynolds number. For the required three-dimensional wind data, the spatial grid would scale with $n{\cdot}\mathrm{Re}^{9/4}$, where n is the required number of grid points spanning the smallest flow scale in one direction. With a Reynolds number in the order of 10^8, the spatial grid would scale with $n{\cdot}10^{18}$. Without even considering the

fact that the equations will have to be integrated in time, where the time steps also scale inversely with Reynolds number, generating the wind data using DNS is completely unfeasible.

With a clear need for a turbulence model to avoid having to resolve all the way to the smallest eddy-scales, an obvious candidate would be **Reynolds-Averaged Navier-Stokes (RANS)**. Where DNS resolves all turbulent scales, RANS aims to only resolve the mean flow. This requires separating the mean-flow quantities from the turbulent fluctuation. The Navier-Stokes equations therefore have their flow variables split, using Reynolds decomposition, into the time-averaged mean, $\overline{u}$, and the time-dependent fluctuation, $u'(t)$[16]. When applied to the momentum equation, the mean-momentum equation (also known as the Reynolds equation) is similar to the original Navier-Stokes equation, except for the appearance of the Reynolds stresses. This term appears when taking the mean of the nonlinear advective term in the momentum equation and applying the Reynolds decomposition[15]:

$$\frac{\partial}{\partial x_j}\overline{u_i u_j} = \frac{\partial}{\partial x_j}\overline{(\overline{u}_i + u'_i)(\overline{u}_j + u'_j)} = \overline{u}_j \frac{\partial \overline{u}_i}{\partial x_j} + \frac{\partial}{\partial x_j}\overline{u'_i u'_j} \tag{4.3}$$

Where the last term contains the velocity covariances known as the Reynolds stresses[15]. The Reynolds stress is the turbulent momentum flux acting like a stress by deforming a hypothetical fluid cube through the different velocities on opposite faces[13]. The mean-flow equations are now not only dependent on the mean-flow variables, but also the fluctuations. This makes the system underdefined and provides a closure problem. In order to avoid computing the full time-dependent flow field, a turbulence model is utilized to approximate the Reynolds stresses and relate them to the mean-flow variables. The approximation models all introduce a modeling error, which is therefore inherent to RANS. Several models exist, with a differing complexity and accuracy, from the basic mixing-length model via the eddy-viscosity models to the complex Reynolds stress model[14]. Turbulent-viscosity models (and its derivatives) relate the Reynolds stress to the mean rate of deformation and introduce the turbulent viscosity ν_T. These models assume isotropy for the entire turbulent spectrum, presenting a drastic departure from reality for the large scales which are (highly) anisotropic. Some of the more complex models are based on rapid distortion theory which only assumes isotropy for the initial case[15]. The much-reduced computational load of RANS compared to DNS, therefore comes at a significant cost in accuracy.

In-between the computationally expensive DNS and the lower-accuracy RANS is **Large Eddy Simulations (LES)**. The goal of a large-eddy simulation is to obtain an explicit description of the large-scale turbulent motions containing the energy-producing mechanisms of momentum and heat flux. The small-scale motions are replaced by a model in order to drastically reduce computational load. A spatial filter is applied to the motions in order to therefore separate them into resolved-scale, $\tilde{u}(t)$, and subfilter-scale, $u'(t)$. The spatial filtering of the field is achieved using a convolution with a kernel/filter function, G_Δ, with filter size Δ. Examples of this kernel are the spectral cut-off filter, Gaussian filter, and box filter[17].

Similarly to RANS, the decomposition introduces a subfilter-scale (SFS) term in the momentum and energy equations of the resolved scales, the SFS-stress and SFS-flux term, respectively. This provides a closure problem again. The crucial difference with RANS is that LES only requires a turbulence model for the mechanics in the inertial subrange and dissipation range, as the scale of the filter is in the order of the inertial subrange, see Figure 4.1. The model replaces the transfer of the resolved turbulent kinetic energy to the dissipation range and the subsequent dissipation of kinetic energy. The anisotropic nature of the energy-containing range is therefore not included in the model, thereby greatly reducing the modeling error compared to RANS and allowing the model to be less complex. Only in regions where the small scales are important, like in wall flow, can the modeling error of LES be severe[18]. Several models for the SFS-stress and -flux exist, one of the most common models is the Smagorinsky-Lilly model, which is based on eddy-viscosity[18].

Apart from the previous simulation types based on the Navier-Stokes equations, a separate category of turbulence generation exists. These simulations are the synthetic turbulence models, like Kaimal or Mann, which simulate turbulence-like behavior based on spectral tensor or coherence models that should resemble turbulence[19]. They are considered by the International Electrotechnical Commission (IEC) to be adequate to simulate turbulence in wind turbine design[20]. They do not produce

	Size	Resolution	Number of points
Spatial (x,y,z)	$350 \times 250 \times 250$ m^3	$10 \times 5 \times 5$ m^3	87,500
Temporal	1000 s	3 Hz	3,000

Table 4.1: Wind data domain

actually physical flows based on mass-, momentum- and energy transfer. Furthermore, they typically create 3D-data resulting in only spatial data without any wind evolution. To simulate a wind field approaching a turbine, Taylor's Frozen Turbulence is assumed to change the longitudinal dimension to a time dimension. Four-dimensional synthetic turbulence exists[21], but, while potentially useful as easy yet simplified data for testing predictive wind models, they are wholly insufficient for validating the underlying assumptions as they do not contain the necessary and complex effects of the foundational fluid dynamics and turbulent intricacies. These methods will therefore not be considered for the validation of the underlying assumptions.

For the high-Reynolds flows of interest in this research, LES seems the best fit and will be used to generate the required wind field data. It captures and resolves the relevant turbulent structures without using an approximation model, while remaining in the realm of being computationally achievable.

4.3 LES-data

Appendix A.4 shows the Smagorinsky-Lilly model applied to the ABL-equations. The wind data generated with LES for this research uses this model with a dynamically determined Smagorinksy coefficient[22]. The data has kindly been provided by dr. R.J.A.M. Stevens of the Physics of Fluids department at the University of Twente. The data is extracted from several simulations spanning several kilometers and multiple hours in order to fully develop the flow and minimize computational boundary influences. The actual wind data used is a much smaller spatial- and temporal region. Table 4.1 shows the size and resolution of the extracted wind data. The original LES domain is $4 \times 2 \times 4$ km^3.

The wind data consists of six scenarios: three different atmospheric stabilities for two different mean wind velocities. This allows the validation to determine whether the assumptions are dependent on these effects. The wind data is simulated in a free domain without a modeled turbine and therefore does not show the turbine blockage effect or induction. While this means that the wind data is applicable in general and not for a specific turbine, this research will not be able to confirm whether the turbine induction has a significant effect on the assumptions made. Researching the assumptions in a free atmosphere must therefore be considered a baseline.

Classification of the wind data scenarios is important to determine whether the data is representative of typical wind turbine operating conditions. The IEC turbine design guidelines are specified in terms of hub wind speed, which requires assuming a certain hub height. This research is based on a wind turbine with a hub height of 100 m and a rotor radius of 70 m. The mean wind speed at hub height of the data sets, 8 m/s and 15 m/s, can be compared to the IEC wind turbine classes[20]. Figure 4.2 shows that the 8 m/s LES data set constitutes a velocity around the highest occurrence, depending on class. The 15 m/s data set is a higher-velocity case. Table 4.2 shows the mean velocity and standard deviation of the wind speed at hub height in all three directions. Appendix B.1 shows the corresponding velocity profiles for both data sets and Appendix B.2 shows the profiles of the time-averaged velocities. In data set 2, the lateral and vertical velocities are small compared to the longitudinal velocity. The flow is generally aligned with the longitudinal axis. For data set 1 the lateral velocity is more pronounced compared to the longitudinal velocity. Figures 4.3 and 4.4 show the spread of the velocity profiles for the longitudinal and lateral velocities, respectively. Where the unstable case has a mean lateral velocity around 8% of the longitudinal velocity and the neutral case only around 5%, the stable case shows a more significant lateral drift. The mean lateral velocity in the stable case increases drastically with height and reaches around 20% of the longitudinal velocity. At hub height, the drift is similar to the unstable case, but at the top of the rotor the flow is clearly not aligned with the longitudinal direction.

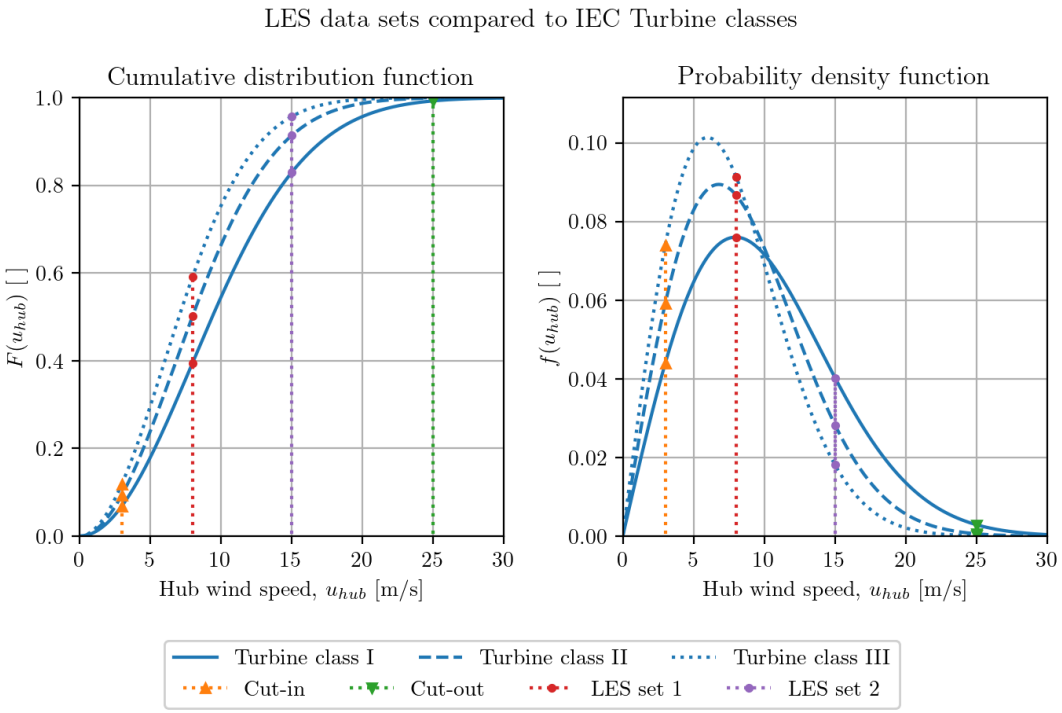

Figure 4.2: LES data sets compared to IEC turbine class

			Data set 1			Data set 2		
			unstable	neutral	stable	unstable	neutral	stable
Mean velocity	$\overline{u}_{\text{hub}}$	[m/s]	8.33	7.98	8.86	15.8	15.3	14.8
	$\overline{v}_{\text{hub}}$	[m/s]	-0.69	-0.32	-0.61	0.22	-0.22	-0.21
	$\overline{w}_{\text{hub}}$	[m/s]	0.00	0.03	0.00	-0.14	0.00	0.00
Standard deviation velocity	$\sigma_{u,\text{hub}}$	[m/s]	0.48	0.46	0.27	0.47	0.95	0.70
	$\sigma_{v,\text{hub}}$	[m/s]	0.48	0.41	0.25	0.46	0.77	0.60
	$\sigma_{w,\text{hub}}$	[m/s]	0.41	0.31	0.16	0.39	0.60	0.47
Turbulence intensity	$I_{u,\text{hub}}$	[%]	5.63	5.72	3.12	2.92	6.21	4.68
Turbulence kinetic energy	k_{hub}	[m^2/s^2]	0.32	0.24	0.08	0.29	0.93	0.53

Table 4.2: LES data: velocity statistics around hub height (100m)

The longitudinal turbulence intensity in Table 4.2 is determined using:

$$I_u = \frac{\sigma_u}{\overline{u}} \tag{4.4}$$

The turbulence intensity for both data sets is around 5%, which is considerably lower than the IEC design guideline (Normal Turbulence Model, class C) for the relevant velocities: 17.4% and 13.5% for 8 m/s and 15 m/s hub wind speed, respectively[20]. While the IEC guidelines can be considered conservative and realistic turbulence intensity can be expected to be lower[23], the LES-data available has relatively low turbulence intensity. Appendix B.3 shows the longitudinal turbulence intensity profile for both data sets.

While the low turbulence kinetic energy (TKE) of the high-velocity unstable case may seem illogical, TKE is not a clear indication of atmospheric stability[24]. Unstable atmospheres can show a lower TKE and stable atmospheres can be more turbulent.

Another indicator of turbulence is the friction velocity near the ground. It is defined based on the

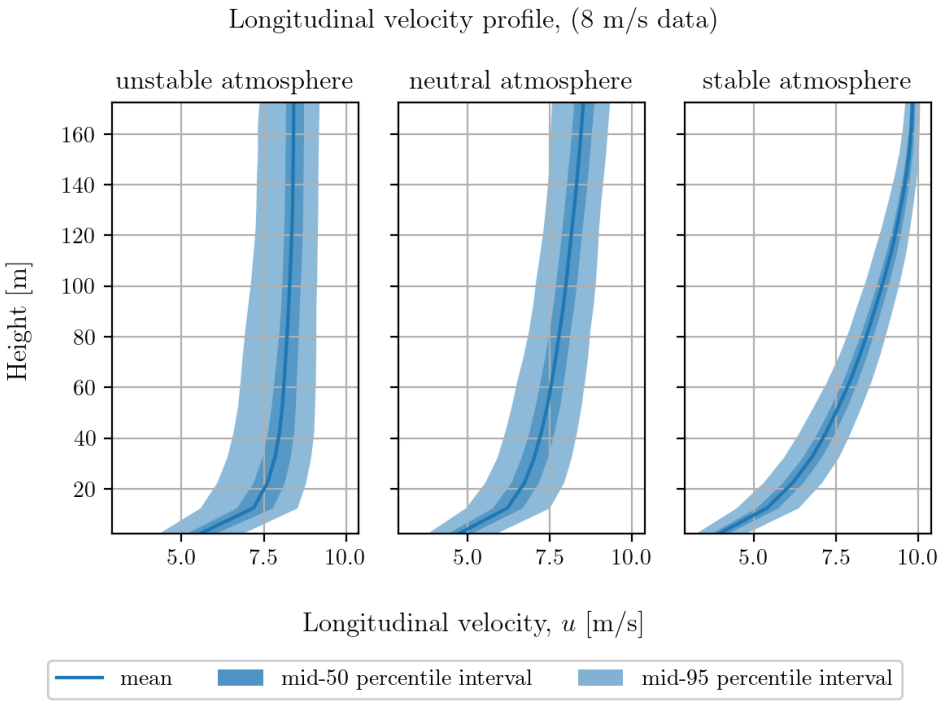

Figure 4.3: Longitudinal velocity profile, data set 1

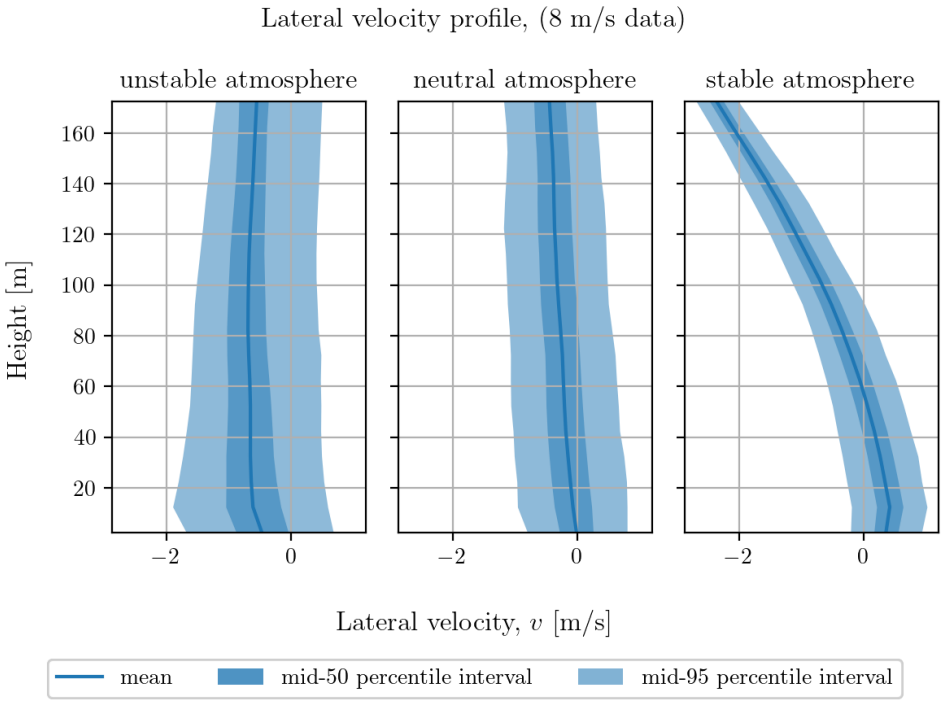

Figure 4.4: Lateral velocity profile, data set 1

		Data set 1			Data set 2		
		unstable	neutral	stable	unstable	neutral	stable
Mean friction velocity	$\bar{u}_*$ [m/s]	0.36	0.28	0.20	0.57	0.56	0.46
Mean Bulk Richardson number	$\overline{\mathrm{Ri}}_B$ [ ]	-0.99	0.00	0.19	-0.18	0.00	0.07
Stability class		A	D	E	A	D	E
Stability		Highly unstable	Neutral	Moderately stable	Highly unstable	Neutral	Moderately stable

Table 4.3: LES data: friction velocity and atmospheric stability

magnitude of the Reynolds stress-components near the surface[13]:

$$u_*^2 = \sqrt{\left(\overline{u'w'}\right)_s^2 + \left(\overline{v'w'}\right)_s^2} \tag{4.5}$$

The friction velocity therefore shows the vertical flux of horizontal turbulent momentum near the surface. Note however that due to the inherent nature of the LES-scheme used, the computational grid is staggered. The virtual temperature, θ, and the longitudinal- and lateral velocities, u and v, are defined at $z = 2.5 + 5k$ m, where k consists of integer values. The vertical velocity, w, is however defined at $z = 0 + 5k$ m. The fluxes therefore consist of quantities that are not defined at the same location. The horizontal velocity perturbations have therefore been interpolated between $z = 2.5$ m and $z = 7.5$ m, which will unavoidably result in only an approximation of the friction velocity. Table 4.3 shows the resulting average friction velocity of the LES-data, calculated using the (interpolated) velocity data at $z = 5$ m. The results indicate that the wind shear is generally strongest for the unstable cases and the neutral case of data set 1. Appendix B.6 shows the spread of the friction velocity.

The atmospheric stability can be inferred from the virtual temperature profile (Appendix B.5); where the virtual temperature indeed decreases with height in an unstable atmosphere, remains constant in a neutral case and increases for a stable atmosphere. A more detailed classification of the atmospheric stability requires determining the Bulk Richardson number[13]:

$$\mathrm{Ri}_B = \frac{g\ \Delta\bar{\theta}\ \Delta z}{\bar{\theta}_0\left((\Delta\bar{u})^2 + (\Delta\bar{v})^2\right)} \tag{4.6}$$

Where the quantities are evaluated at two different heights: z_0 and z_1. Table 4.3 shows the Bulk Richardson number using the minimum and maximum rotor tip heights, therefore showing its value across the rotor. Appendix B.7 shows the spread of the Bulk Richardson number. The atmospheric stability can be determined using the Pasquill stability class and the Bulk Richardson number[25]. Table 4.3 shows the stability class for each scenario, confirming that the LES-data covers three different atmospheric stabilities.

5 Validation

With the LES-data now classified, the assumptions of the wind model can be validated based on this data. The main assumption that will be validated is the application of Taylor's frozen turbulence hypothesis.

5.1 Taylor's frozen turbulence hypothesis (TFTH)

Before the validity of assuming Taylor's frozen turbulence can be investigated, the hypothesis must first be properly understood. Taylor's hypothesis states that the power spectral density of turbulence at a fixed point is directly connected, through a Fourier transform, with the instantaneous cross-correlation of that turbulent signal and a measured signal at a point up- or downstream. This relation hinges on the fact that the mean flow velocity must be much greater than the turbulent velocity perturbations, such that the variation of the measured turbulent signal can be purely attributed to the transportation of an unchanging turbulent eddy over the point[26].

With hypothesizing that the turbulent eddies are advected over a point unchanged and the direct relation between the temporal and spatial correlation of the turbulent signal, a resulting interpretation of Taylor's hypothesis can be formulated:

> *All turbulent eddies are advected with the mean streamwise velocity, without changes to their properties.*

Taylor's hypothesis therefore offers a very powerful simplification to the modeling of a flow. It allows omitting any evolution of the turbulent eddies. The model can then avoid having to solve to the very small scales or an additional turbulence closure model. However, with great power comes great responsibility; applying Taylor's hypothesis to a model without verifying whether the flow is suitable can completely invalidate the result. It can be applied if the evolution of the relevant turbulent eddies has a longer timescale than the duration of the eddy moving past a fixed point. A typically suggested guideline is[13]:

$$I_u < \frac{1}{2} \tag{5.1}$$

This guideline indicates whether the prerequisite for the interchangeability of the auto- and instantaneous cross-correlation (mean flow velocity must be much greater than the turbulent velocity perturbations) is met. It does not tell for how long an eddy can be assumed frozen, only if it is long enough to clear a fixed point[26,27]. The validity of Taylor's hypothesis is also dependent on the turbulent scales of interest[27,28]. The wind model assumes all eddies to be frozen throughout the entire domain. This validation should show whether Taylor's frozen turbulence hypothesis can be applied at all and whether an upper domain length based on the frozen eddies can be formulated. Based on the characteristics mentioned in Section 2, it can be expected that the validity of Taylor's frozen turbulence hypothesis is, at least partly, dependent on the atmospheric stability. The unstable atmosphere, characterized by its turbulence-generating behavior, is expected to have more turbulent evolution and therefore a smaller range where Taylor's frozen turbulence can be applied. The turbulence intensity of the considered flows is however limited, as explained in Section 4.3, so in these cases the effect might be relatively minor. On the other side is the stable atmosphere with its turbulence-stabilizing characteristics. While this should reduce perturbations towards a less turbulent flow, the evolution of the flow is therefore significant. The correlation is then expected to be lowered, resulting in a negative effect on the validity of Taylor's frozen turbulence.

5.1.1 TFTH: Longitudinal correlation

The first step in validation of Taylor's hypothesis is to compute the relevant correlations. The correlation of two signals indicates whether a linear relationship between them exists. Pearson's correlation coefficient of two hypothetical signals $a(t)$ and $b(t)$ is computed by:

$$\rho_{a,b}(\tau) = \frac{\overline{a'(t)\ b'(t+\tau)}}{\sigma_a \sigma_b} \tag{5.2}$$

where τ indicates the delay introduced to signal b. The correlation coefficient ranges from -1 (inversely proportional) to 1 (directly proportional). Two signals are completely uncorrelated if the coefficient is zero.

Both the auto-correlation (signal a compared to itself) and spatial cross-correlation (where signal b is measured spatially distanced from a) are computed using the velocity signals at specific grid points. As the LES-data is mostly aligned with the longitudinal axis, the focus will be on longitudinal correlation of the streamwise velocity, i.e. longitudinal velocity. Furthermore, the LES-data consists of discretely sampled velocity signals and, consequently, the delay consists of discrete steps or lags. These lags have a fixed size based on the sampling frequency, i.e. 1/3 seconds.

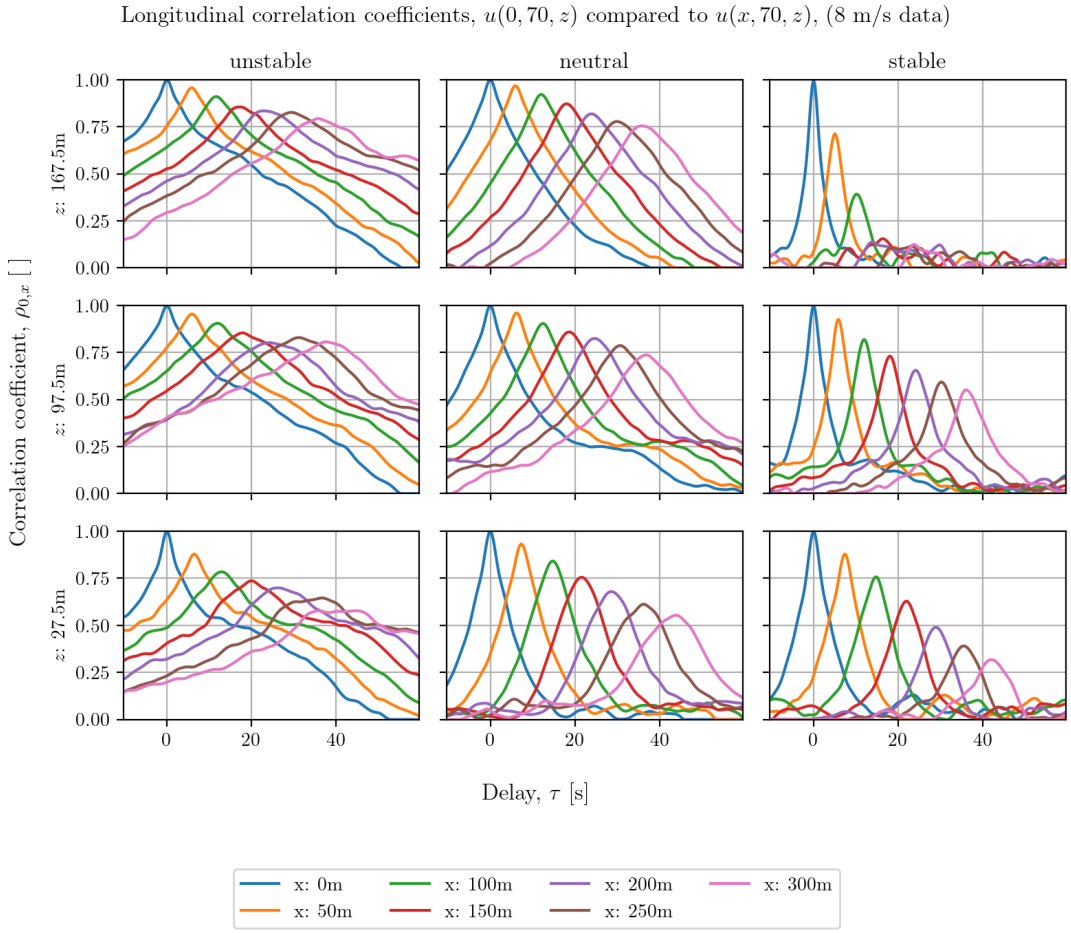

Figure 5.1: Longitudinal correlation for several atmospheric stabilities at three heights

Interpretation of Figure 5.1

As it is still a complicated figure, a guide on interpretation will be offered. First of all, there are three variables to play with: height, atmospheric stability and longitudinal separation distance between the measurement points. The subplots are ordered in a 3×3-grid where each row corresponds to a specific height as indicated on the left. Each column corresponds to a certain atmospheric stability as indicated on the top. The subplots themselves have the correlation coefficient $\rho_{0,x}$ on the y-axis and the delay τ on the x-axis. Each colored line is the correlation between the velocity signal at $x = 0$ m compared to the velocity signal measured at the separation distance corresponding to that color as shown in the legend. For example, the cross-correlation between the signals at $x = 0$ m and $x = 150$ m at hub height ($z = 97.5$ m) in the neutral atmosphere is the red line in the center plot. This cross-correlation seems to have a peak of around 0.85 at a delay of approximately 18 seconds.

Figure 5.1 shows the correlation coefficients of a sample of the available velocity signals. The sample contains the longitudinal velocity signals at three distinct heights (blade tip vertically down, hub height and blade tip vertically up) and at a specific lateral value. The correlation coefficients are then computed using the 35 signals along the longitudinal beam and comparing them to the signal at $x = 0$, i.e. separation distance. The figure therefore shows the auto-correlation and, for clarity, only the correlation coefficients of the signals at intervals of 50 meters are plotted.

The plots generally show clear peaks that decrease with greater separation distance. This reduction in peak correlation with longitudinal distance can be caused by turbulent evolution of the flow or the flow not being aligned with the longitudinal direction. As mentioned in Section 4.3, the lateral drift for the higher-velocity case is minor. Figure 5.1 shows the lower-velocity case where the lateral drift has slightly more effect in the unstable and neutral case. The stable case has a similar lateral drift at hub height and rotor bottom, but the poor correlation at the rotor top can mostly be explained by the significant lateral drift mentioned in Section 4.3. The influence of turbulent evolution on the correlation can therefore not be determined for that case.

These plots do seem to indicate a difference in behavior across the three atmospheric stabilities. The unstable atmosphere shows a relatively small decrease in peak correlation over separation distance and the peak correlation seems to increase with height. The peaks are generally more flattened and not as clearly defined as the neutral case, for example. This could indicate turbulent evolution where the flow structures, apart from the largest sizes, have evolved significantly or a change in advection velocity, especially as this behavior is more pronounced for greater separation distances.

The neutral case shows very defined peaks and, like the unstable case, the peak correlation decreases slowly with separation distance and is better with increasing height. The well-defined peaks also nicely show the transport velocity, as the delay for the largest separation distance is smaller at the rotor top compared to the rotor bottom, as was shown by the velocity profiles.

The stable case has a larger decrease in peak correlation and shows very poor correlation at the rotor top, which was already attributed to the lateral drift. The hub height and rotor bottom are less influenced by the lateral drift providing an insight into the velocity correlation. Similarly to the neutral case the peaks are generally quite narrow and well-defined.

5.1.2 TFTH: Combining and extracting correlation data for analysis

Note that Figure 5.1 only shows the correlation of seven velocity signals per three heights per three atmospheric stabilities for only one data set. The total number of velocity signals available equals $87,500 \cdot 3 \cdot 2 = 525,000$, with each signal consisting of 3000 measurements. Figure 5.1 is therefore only a tiny subset of the available data and is only indicative of how the correlation coefficient typically behaves with delay and separation distance. Using the entirety of the available data to compute correlation coefficients regrettably runs into memory and computation time limits. Furthermore, not all data is equally important to the validation of Taylor's hypothesis, as the focus is primarily on the heights corresponding to the rotor.

A compromise between plotting the data belonging to some points on a longitudinal line, and attempting to plot all data at once, is to plot the data of all points on a select number of horizontal planes. The data to be analyzed is then reduced to $35 \times 50 = 1750$ points per plane. However, plotting all these correlation coefficient signals, like Figure 5.1 shows for only seven signals per plot, is still unfeasible. It is also unnecessary as the entire correlation signal is not of interest, only the correlation coefficients at a few select delays are important. The three distinct correlation coefficients per grid point which should be analyzed are:

- Instantaneous cross-correlation, $\rho_{a,b}(\tau = 0)$
- Peak cross-correlation, $\max(\rho_{a,b}(\tau))$
- Cross-correlation at the expected delay, $\rho_{a,b}(\tau = t_{a \to b})$

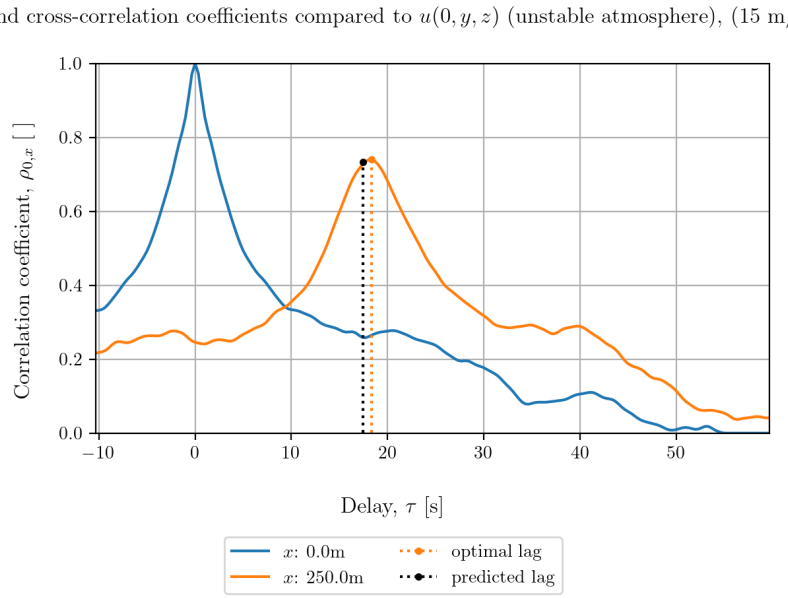

Figure 5.2: Example of difference between expected- and optimal delay, data set 2

The expected delay is the time it would take for a flow particle to travel a certain distance when moving with the mean velocity:

$$t_{a \to b} = \frac{x_{a \to b}}{\bar{u}} \tag{5.3}$$

When assuming Taylor's hypothesis, and consequently that the frozen turbulent eddies advect with the mean velocity, there is a two-parted condition implied. Firstly, the frozen flow implies perfect correlation. Secondly, the advection with the mean velocity implies that the perfect correlation should occur exactly when the delay equals the travel time to the downstream measurement location. Therefore, the cross-correlation at the expected delay is of great importance, because it will show to what degree the flow is unchanging when assumed to be moving with the mean velocity. In reality the peak correlation may not occur at the expected delay due to the eddies moving at speeds different than the mean velocity or a mixing of flows may alter the mean velocity. Other mismatches may occur from computational issues. If the mean velocity is not aligned with the computational grid, this will introduce inaccuracies from drift. Lastly, the computation of the mean velocity also influences the expected delay, as we are dealing with two measurement locations between which the mean velocity may fluctuate. The first and simplest option is to only use the time-averaged velocity as determined by the initial measurement point. The second option is to take the mean of the time-averaged velocities of the measurement points that are being compared. A more complex option is to also include the time-averaged velocities of any intermediate grid points. More complex options reduce the introduced error. This research uses the first option to reduce the computational load and due to the fact that the time-averaged longitudinal velocities do not change or fluctuate significantly, as can be inferred from Figures B.7 and B.8 in Appendix B.2.

Figure 5.2 shows an example of the difference between the expected delay and the delay corresponding to the peak cross-correlation. The difference between them is in the order of one second, which still translates to roughly a 15 meter difference over a distance of 250 meters, equating a 6% mismatch. In this case the effect of the mismatch is probably rather minor, as the peak cross-correlation and the cross-correlation at the expected delay differ very slightly.

Figure 5.3 shows a larger discrepancy in the delays and while the correlation difference is not very large, it does indicate an interesting effect. The figure shows the cross-correlation has a plateau-like shape lasting for almost ten seconds. This indicates that the cross-correlation between the signals is somewhat insensitive to the delay, as long as it remains within the ten second bound. This could be due to the large-scale flow structures matching between the signals, but the smaller ones not as

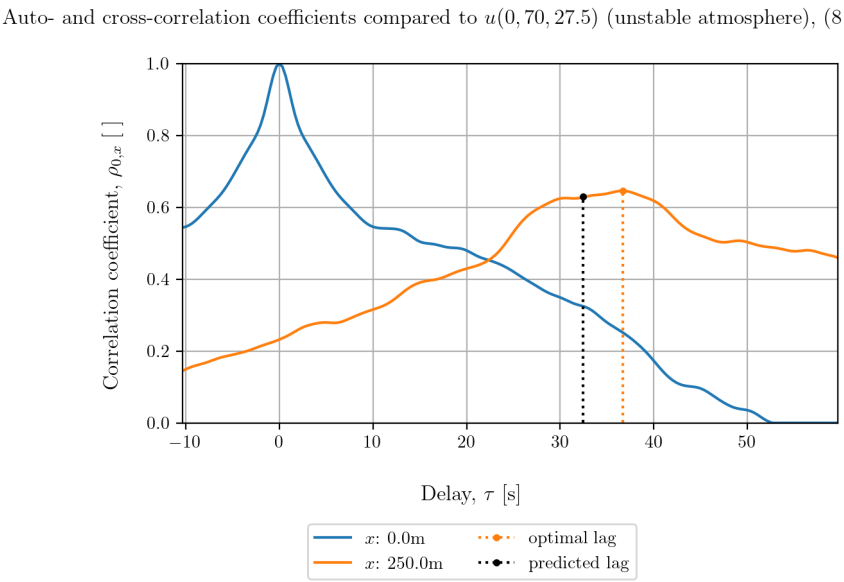

Figure 5.3: Example of difference between expected- and optimal delay, data set 1

a result of turbulent evolution or due to the advection speed of the eddies changing significantly during the measurement period.

It will be important to take note of these discrepancies, because they can indicate specific behavior when analyzing the 1750 cross-correlation signals for the three horizontal planes each, without having to check them separately. Extracting all the cross-correlation coefficients at the expected delay for all longitudinal beams would still result in 50 lines being plotted per panel. While colorful, it would not necessarily give the clearest picture, as overlapping lines would obscure important information. Instead the coefficients will be bundled based on separation distance and then only the mean, mid-50 percentile and mid-95 percentile will be shown. This should provide all relevant information into how the coefficients of all signals behave.

The correlation coefficient data is inherently tied to the sampling frequency of the velocity data. The delay is applied by shifting the signals an integer amount of points compared to each other. The correlation data as a function of delay is therefore discrete with steps of 1/3 seconds. It is then highly probable that the calculated expected delay will not match exactly with the sampled delays. The closest available delay is then used, which introduces a maximum discrepancy of $\pm 1/6$ seconds.

Auto-correlation and instantaneous cross-correlation

As mentioned in Section 5.1, Taylor stated that the power spectral density of turbulence at a fixed point is directly connected, through a Fourier transform, with the instantaneous cross-correlation of that turbulent signal and a measured signal at a point up- or downstream[26]. In other words, the cross-correlation with zero delay should equal the auto-correlation of the upstream point at the expected delay:

$$\rho_{a,a}\left(\tau = \frac{x_{a\to b}}{\bar{u}}\right) = \rho_{a,b}(\tau = 0) \tag{5.4}$$

Figures 5.4 and 5.5 show this relation by computing the difference between the auto-correlation and the instantaneous cross-correlation for all considered points and plotting the spread of the results as a function of separation distance.

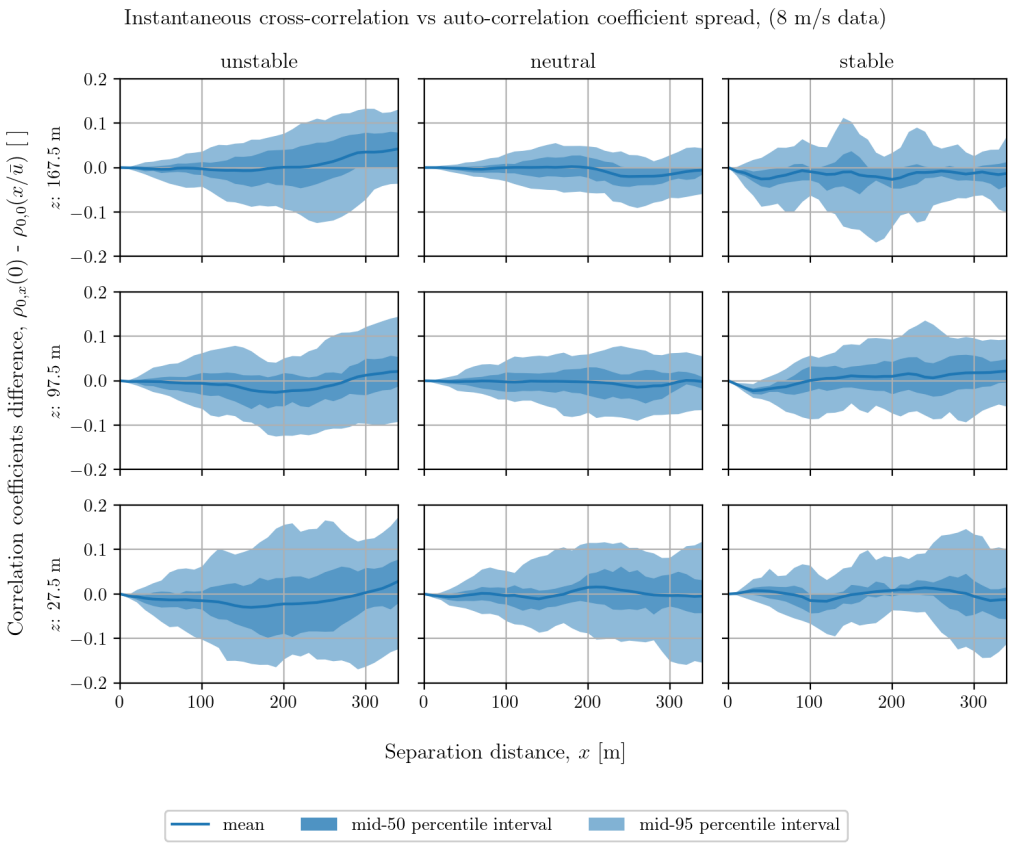

Figure 5.4: Instantaneous cross-correlation and auto-correlation, data set 1

The mean of the spread generally stays at or closely around zero. The mid-50 percentile spread of all cases stays clearly within ±0.1 correlation coefficient point. Especially the higher velocity case, data set 2, shows the relation nicely with very tight spreads. Data set 1, with the lower mean velocity, has a larger spread. This is partly due to the fact that, while the separation distances between both sets are equal, the delay is almost doubled. This provides more time for turbulent structures to evolve and therefore loss of correlation. At that point the correlation coefficients are low enough to be considered largely uncorrelated and any difference between the auto-correlation and instantaneous cross-correlation is mostly up to chance.

A clear dependency on atmospheric stability is harder to conclude. The neutral case seems to show the cleanest relation in both data sets. The stable cases are quite similar to the neutral cases when considering the mean and mid-50 percentile spread. For the stable case of data set 1 it is important to keep the significant lateral drift in mind and therefore not to put too much value on its more erratic behavior. The unstable case has the largest spread generally. This may be caused due to the correlation coefficients not showing a clean descent and an almost plateau-like behavior, as seen in Figure 5.1. The ascent, which includes the instantaneous cross-correlation, is generally cleaner. This difference is especially pronounced at lower heights, which is confirmed by Figures 5.4 and 5.5.

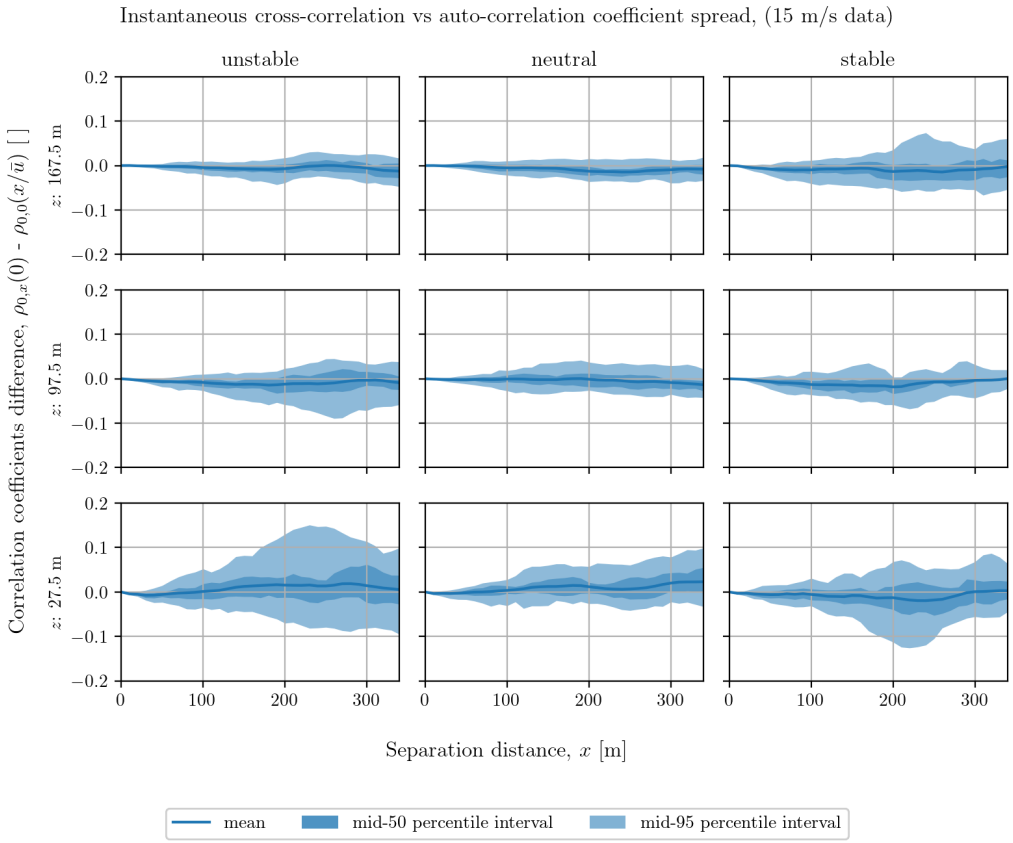

Figure 5.5: Instantaneous cross-correlation and auto-correlation, data set 2

5.1.3 TFTH: Longitudinal correlation spread

Comparing the auto-correlation with the instantaneous cross-correlation shows whether the correlation loss between a signal and its delayed variant is the same as between the same signal and its advected variant. It therefore indicates whether a change in time has a similar effect as a change in space. If the correlation coefficients are indeed equal, it means that the amount the signal has changed over time or space is similarly different from the original signal, but is does not necessarily mean that they have changed equally. It does not guarantee that the delayed original signal and the advected signal are then perfectly correlated. The lower the auto-correlation and instantaneous cross-correlation are, the larger the likelihood that the changed signals are not equal.

To more directly investigate the change of the velocity signal when advected with the flow, the cross-correlation at the expected delay is used. Figures 5.6 and 5.7 show the spread of the cross-correlation coefficients versus the separation distance. In an ideal world the correlation coefficient would remain unity across the separation distance and the spread would be narrow. This is clearly not the case as the correlation coefficient slowly decreases with increasing separation distance, indicating that the flow perturbation changes when moving through the domain.

The results of data set 2 show jagged behavior in some places. This is caused by modeling inaccuracies due to the sampling frequency mentioned in the previous section. The correlation data is determined with steps of 1/3 seconds, causing a slight mismatch with the expected delay. In data set 2 the the mean flow velocity is around 15 m/s and this mismatch of at most $\pm 1/6$ seconds means that the actual flow particle is 2.5 meters (or 25% of the grid spacing) away from the grid point at the delay used. If the spread is narrow and one grid point uses a slightly earlier delay and a neighboring grid point uses a slightly later delay, a step-like effect may occur in the correlation spread.

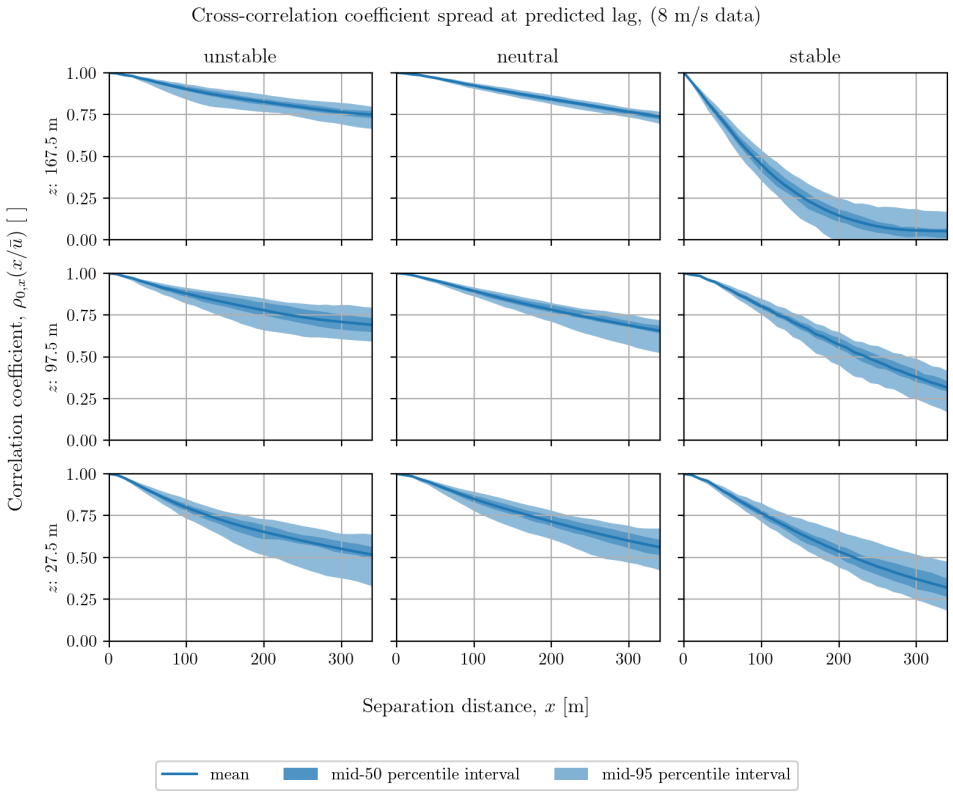

Figure 5.6: Spread of cross-correlation coefficients at expected delay, data set 1

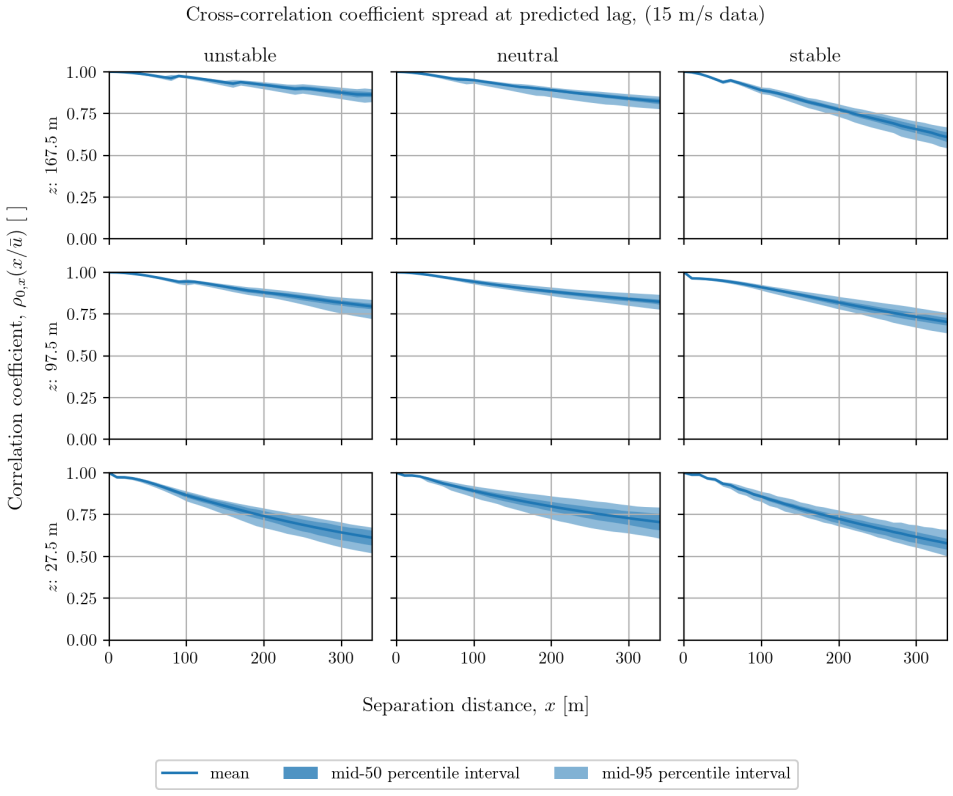

Figure 5.7: Spread of cross-correlation coefficients at expected delay, data set 2

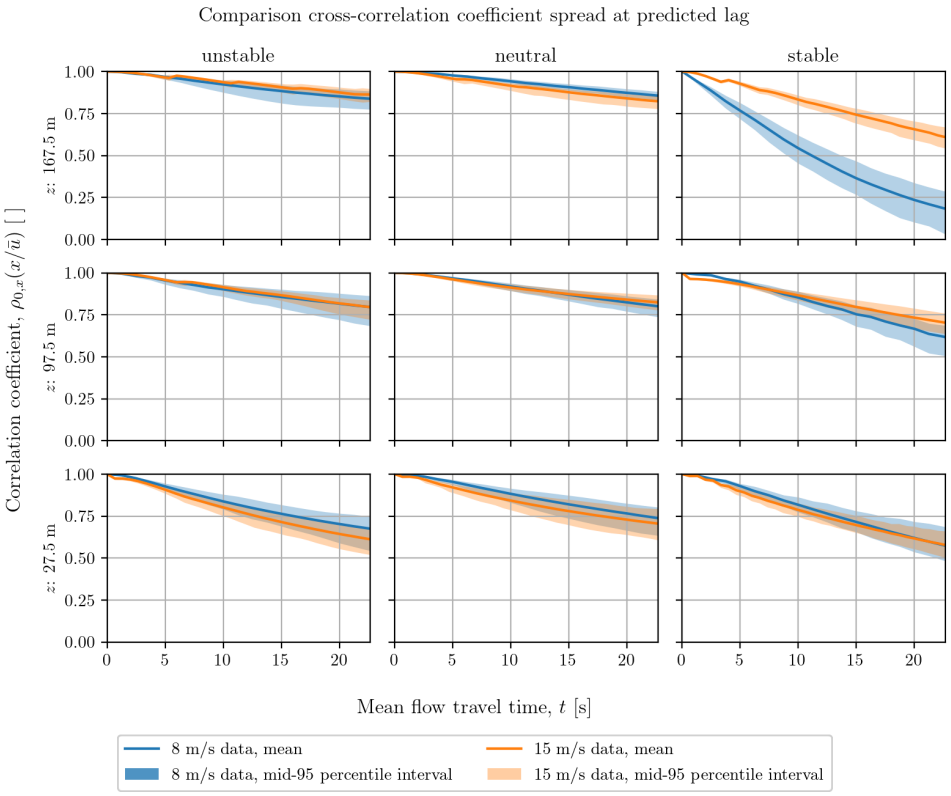

Figure 5.8: Travel time comparison of spread of cross-correlation coefficients at expected delay

Increasing the sampling frequency would reduce this effect, but cannot be done as post-processing. Interpolating would solve the issue, but it would always be an approximation introducing some error depending on the interpolation scheme used. As the jagged effect is relatively minor, it is deemed unnecessary to apply interpolation.

Influence of mean velocity

The influence of the mean velocity seems clear: data set 2 has a lower correlation decrease over distance. The spread is also tighter throughout the domain. This difference should be expected when considering that it takes the higher-velocity flow around 23 seconds to traverse the domain and the lower-velocity flow around 43 seconds. The flow of data set 1 therefore has much more time to evolve and therefore result in a loss of correlation. After around 23 seconds, the lower-velocity flow would have traveled around 180 meters. Figure 5.8 shows a comparison of the correlation spread of both data sets during the first 23 seconds. The separation distance has been converted to the time domain using the mean velocity of the entire data set. It is therefore not representative of the actual mean flow travel time at each plane.

Apart from the highest plane of the stable case of data set 1, the results are very similar. Especially the neutral case which shows only minor differences between the data sets. The unstable case of data set 1 does show a slightly larger spread, which may be caused by the higher turbulence intensity. In general, for flows with similar turbulence intensities, the correlation loss over distance is directly tied to the mean velocity. While this may seem obvious, it is important to keep this in mind when using LiDAR to predict the incoming wind field, as these prediction models are generally focused to specific distances instead of lead time.

Height [m]	Lateral drift [ ]					
	Data set 1			Data set 2		
	unstable	neutral	stable	unstable	neutral	stable
167.5	6.7%	5.2%	22.7%	0.9%	2.4%	5.3%
97.5	8.3%	4.0%	7.0%	1.4%	1.5%	1.4%
27.5	8.4%	2.0%	4.7%	2.4%	0.3%	1.8%

Table 5.1: Lateral drift $\left(\overline{|v|}/\bar{u}\right)$ for each case

Influence of atmospheric stability

Judging the correlation loss across the three atmospheric stabilities, shows that the neutral case has generally the best performance across both data sets. It also has the narrowest spread, indicating that the correlation loss is more predictable. The unstable case is generally quite close to the neutral case, but shows a slightly larger spread. It also seems to vary more with height. The unstable case at the top plane is usually at or a little bit better than the neutral case, whereas it is clearly lower at the bottom plane. Additionally, the unstable case of data set 1 also shows the influence of the higher turbulence intensity, compared to data set 2. Where the spread of the neutral case decreases somewhat, the spread of the unstable case reduces much more. The stable case is more difficult to compare due to the aforementioned lateral drift in data set 1. In data set 2 the stable case shows the worst performance, but it is still relatively close to the other two cases.

Influence of height

With increasing height, the correlation loss decreases. This effect is somewhat stronger in the unstable and stable cases compared to the neutral case. The spread is also narrower with increasing height, which is expected when considering the increased turbulence intensity closer to the ground. It also seems to confirm that the correlation loss and the spread are tied to the turbulence intensity. Due to the increased energy present in more turbulent flows, these flows evolve more significantly when traversing through the domain, resulting in increased correlation loss.

Influence of drift and misalignment

While the stable case of data set 1 does not provide much insight into the turbulent evolution for stable atmospheric stability, it can provide insight into the effect of a flow not aligned with the computational grid. On the top plane, the lateral velocity spread (Figure 4.4) indicates that the lateral velocity is around -2 m/s in the stable case. Meanwhile the longitudinal velocity is around 10 m/s (Figure 4.3), resulting in a 22.7% lateral drift, as shown in Table 5.1. The table shows the average lateral drift for all the cases used in the correlation analysis. This also shows another reason why the higher-velocity data set has better correlation performance; the lateral drift is much lower. The 22.7% lateral drift is a clear outlier, resulting in a grid misalignment of 12.8°. In reality this may occur too when there is a wind veer or a large gust occurs. If the wind turbine has a yaw misalignment to the mean flow a lateral drift is created which is invariant to height.

To put the 12.8°misalignment somewhat into perspective, the IEC extreme direction change case prescribes a 26.8°direction change for the velocity of the respective plane[20]. This direction change has a return period of 50 years, so a 12.8°is more frequent. It may also occur that a localized gust has a significant direction change compared to the mean flow and in order to overcome the LiDAR cyclops issue the lateral velocities are sometimes assumed to be equal across all measurement locations[29]. The actual flow in certain parts of the computational domain may then have a similar misalignment. It is therefore important to consider the drastic effect a misalignment has on the correlation coefficients and consequently the wind prediction accuracy.

Comparing the lateral drift across the two data sets allows investigating the effect of increasing the

lateral drift by a certain factor. The top plane of the stable case has a 22.7% drift in data set 1 and 5.3% in data set 2 which equates to a decrease of roughly 4×. Other cases, like the top plane of the unstable case, show a much larger difference, exceeding 7×. However the correlation loss for those unstable cases is very minor, as shown in Figure 5.8. The top plane stable case has a roughly 2.5× faster correlation loss for data set 1 in the first ten seconds. Other factors like atmospheric stability, turbulence intensity, height are either equal or comparable and by analyzing the time domain, the effect of the mean velocity difference has been eliminated. This shows that the influence of lateral drift on the correlation is not linear, which can be expected when considering the energy spectrum of turbulence. The larger eddies contain more energy and therefore have a larger contribution to the velocity perturbation. This energy is however not linearly related to the eddy size, as shown in Figure 4.1. With increasing lateral drift, increasingly larger eddies will no longer advect past a downstream measurement point and, consequently, the impact on the velocity perturbation is larger. As a result the correlation coefficient will decrease much faster. The effect of large lateral drift on the correlation is clearly major and dwarfs any other effects like turbulent evolution.

5.1.4 TFTH: Validity based on correlation

With the identification of the influences on the longitudinal correlation, the question remains: what is good enough? Up to which point can Taylor's frozen turbulence realistically be assumed? There is no real hard and fast rule. Several criteria have been formulated, but in the end it depends on the use case; what correlation loss still leads to an acceptable prediction and what the limiting behavior is. When the wind model is used mostly to reduce fatigue loading on the turbine blades, the limiting case may be different compared to the case of reducing peak loading. For peak loading the correlation cut-off may be dependent on a peak velocity mismatch of a certain duration, whereas for fatigue loading the average mismatch may be more of interest.

The validity of Taylor's frozen turbulence is therefore difficult to specify to a certain distance or duration. Three different cut-off criteria will be investigated as guidelines:

- Cross-correlation at expected delay, $\rho_{a,b}(t_{a\to b})$, below 75%
- Auto-correlation, $\rho_{a,a}(\tau)$, below 20%
- Integral length scale, L_x

The first criterion, based on the expected delay, is set at 75% indicating strong correlation, but its specific choice is arbitrary. The second criterion, using the auto-correlation, has a cut-off at 20%, which focuses on whether an eddy advects past a sensor mostly unchanged[27]. Lastly, the integral length scale indicates up to which distance a flow particle was influenced by the original position. It is derived from the integral time scale which in turn is based on the auto-correlation and the delay at which it drops to zero ($\tau_{\rho=0}$):

$$L_x = \bar{u}T_x, \quad \text{with} \quad T_x = \int_0^{\tau_{\rho=0}} \rho_{a,a}\ \mathrm{d}\tau \tag{5.5}$$

The cut-off based on the cross-correlation is computed for the three horizontal planes and its mean distance to cut-off is shown in Table 5.2. These values correspond to the mean crossing 75% in Figures 5.6 and 5.7. The other two criteria have been determined for the same horizontal planes and additionally the vertical profiles can be found in Appendix C.1-C.4 for the auto-correlation cut-off and the integral scales. Both are shown in terms of duration and distance.

From Table 5.2 it is clear that the integral length scale is the most conservative of the criteria, often being half the distance compared to the highest criterion. The other two criteria take turns on being the least stringent. Unsurprisingly, as the mean velocity is higher, data set 2 has a longer distance to cut-off, although the difference between the unstable cases is not as large as between the neutral cases.

Note that the stable case is the worst-performing in both data sets. Keeping the significant lateral drift in data set 1 in mind, this is unsurprising for the criterion based on the cross-correlation.

Height [m]	Cut-off criteria	Mean distance to cut-off [m]					
		Data set 1			Data set 2		
		unstable	neutral	stable	unstable	neutral	stable
167.5	$\rho_{a,b}(t_{a\to b}) \leq 75\%$	340	320	40	>340	>340	220
	$\rho_{a,a}(\tau) \leq 20\%$	397	231	52	471	438	169
	L_x	219	138	41	244	351	98
97.5	$\rho_{a,b}(t_{a\to b}) \leq 75\%$	230	230	120	>340	>340	280
	$\rho_{a,a}(\tau) \leq 20\%$	308	230	93	349	485	115
	L_x	164	126	63	177	313	68
27.5	$\rho_{a,b}(t_{a\to b}) \leq 75\%$	130	170	110	190	270	180
	$\rho_{a,a}(\tau) \leq 20\%$	314	184	67	260	461	142
	L_x	163	117	46	157	230	81

Table 5.2: Mean distance to cut-off for criteria cross-correlation at expected delay below 75%, auto-correlation below 20% and integral length scale

The other two criteria are however based on the auto-correlation and, at first glance, it may be surprising that they are still impacted by a grid misalignment, as it only takes data from one grid point. This is due to the flow structures being more aligned with the flow direction from effects like vortex stretching. The coherent flow structures are generally narrower than they are long, in the reference frame of the flow direction. When measuring the correlation of these structures, it therefore decreases more rapidly when misaligned. There is however still a significant impact from the atmospheric stability as data set 2 also has the smallest cut-off distance in the stable case.

In the unstable case of data set 1 the criterion based on the auto-correlation crossing 20% produces significantly larger estimates than the cross-correlation criterion. This was foreshadowed in Figure 5.3, for one specific grid point, showing the plateau-like cross-correlation combined with a slowly decreasing auto-correlation. Figures 5.9-5.10 show the auto-correlation spread of all points on the horizontal planes for data sets 1 and 2, respectively. It indeed seems that the auto-correlation of all points in the unstable case of data set 1 reduces significantly slower compared to the other cases. This, combined with the plateau-like cross-correlation, indicates, to some extent, an insensitivity to the delay. This may be caused by this case having more dominant larger flow structures which evolve more slowly or by the advection speed of the eddies changing more significantly during the measurement period. If, for example, the eddy advection speed changes significantly after 300 seconds, the first 300 seconds of the velocity perturbations would have a peak cross-correlation at a different delay compared to the second part of the measurement period. As the correlation is taken over the entire measurement period, the result is a saddle-like cross-correlation when plotted against delay, where the peak cross-correlation is lower compared to cases with a clean singular peak. The flatter and more spread out the cross-correlation is, the more gradual this advection speed change may have been throughout the measurement period.

This more spread out behavior also explains why the integral length scale in the unstable case of data set 1 is significantly larger than the other atmospheric stabilities, due to basically being a measure of the area under the plotted mean. It also illustrates how the criteria based on the auto-correlation and the integral length scale are more biased towards cases with less sensitivity to delay, whereas the cross-correlation criterion is largely independent of this sensitivity as it focuses purely on the performance at a specific delay. It is difficult to pinpoint one of these criteria as the most suited, because together they paint a certain picture. The cross-correlation criterion shows how alike the signals are when the mean velocity is expected to have arrived and the other two give more insight into how detrimental the effect is of a delay mismatch.

5.1.5 TFTH: Expected delay vs optimal delay

Lastly, the difference between the expected delay and optimal delay is investigated. As mentioned before, the expected delay is based on the travel time of the mean flow to the measurement location

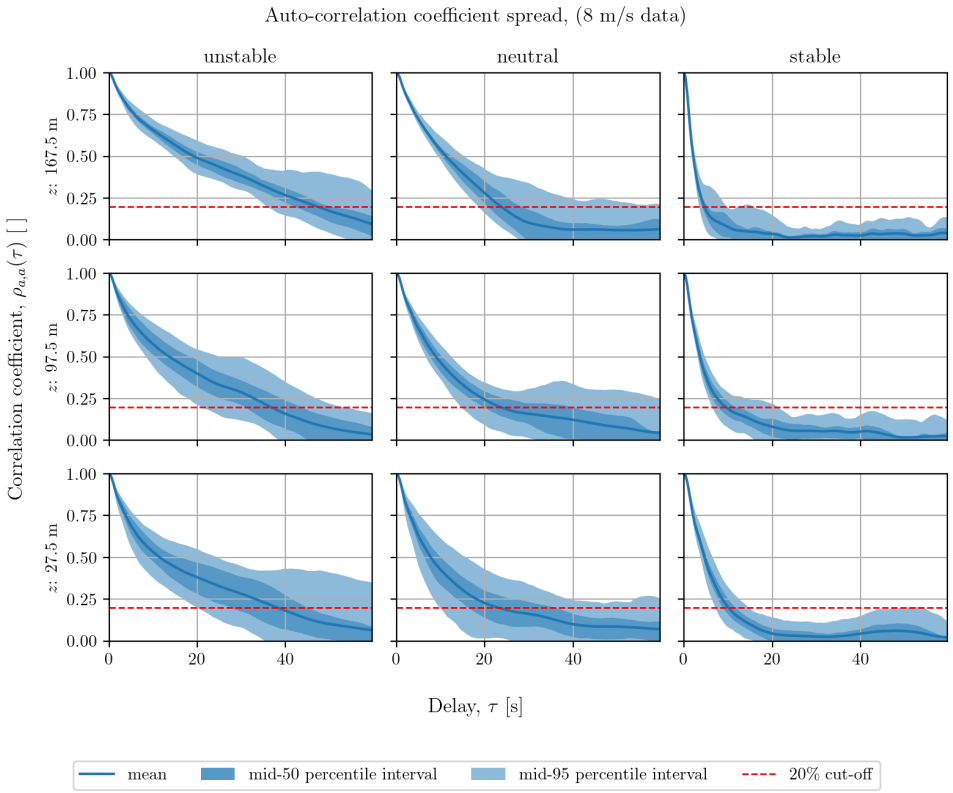

Figure 5.9: Spread of auto-correlation coefficients, data set 1

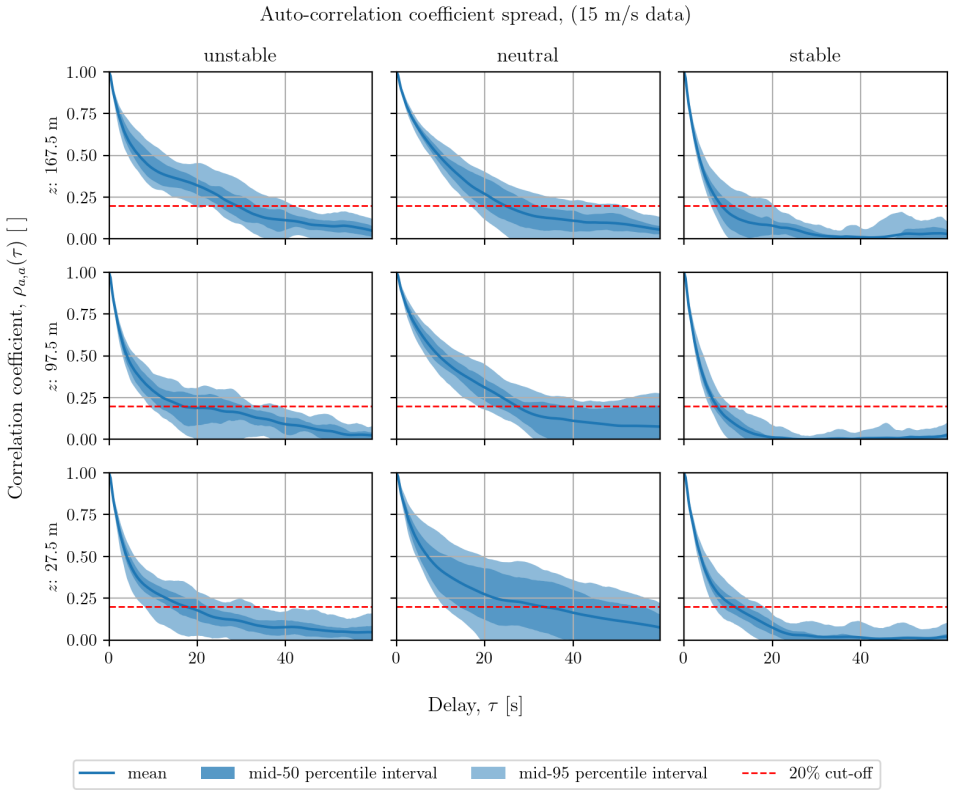

Figure 5.10: Spread of auto-correlation coefficients, data set 2

at a certain separation distance (Equation 5.3). The optimal delay is simply the delay of the peak cross-correlation. Figures 5.11-5.12 show the relative difference between these delays and Appendix C.5 the absolute difference. The relative delay difference is determined using:

$$\frac{\Delta\tau}{\tau} = \frac{\tau_{\text{opt}} - t_{a\to b}}{t_{a\to b}} \tag{5.6}$$

A positive relative difference therefore means that the optimal delay is larger than the expected delay, which generally implies that the actual eddy advection speed is slower than the mean velocity and vice versa for negative differences. Ideally, the difference would be zero, indicating that the actual flow and the expected flow match.

Both figures show oscillatory behavior, especially at the beginning where the relative delay difference is of course large compared the total delay. In data set 2 this behavior is more pronounced, due to the sampling rate being low compared to the velocities, as explained in Section 5.1.3. Data set 1 shows that the unstable case has a somewhat larger spread owing to the more plateau-like cross-correlation functions as previously discussed. Both the unstable- and neutral case have the mean around or at zero. The stable case has the mean deviating from zero, due to the significant lateral drift, which is most pronounced and erratic in the top plane.

Data set 2 has the mean drifting away from zero more often. When looking past the oscillatory behavior of the unstable case, the mean does not hover around zero, but below it for the top plane and above zero for the others, although the difference is rather minor. It does show that velocity perturbations may not advect with the mean flow and therefore reduce the correlation. The neutral- and stable cases also have some deviate from zero, most notably the top plane of the stable case. The peak correlation consistently occurs at a delay longer than the expected delay.

Lastly, the spread is larger for lower heights where the turbulence intensity is higher (as seen in Appendix B.3). A higher turbulence intensity represents the velocity perturbations being larger compared to the mean flow and the impact on the eddy advection speed is therefore larger.

5.1.6 TFTH: Conversion to frequency domain

Analyzing data using the correlation coefficients is a method to judge how alike the signals are in the time domain. All sizes of eddies and therefore all frequencies are included in the analysis and are compared based on the resulting velocity perturbation. The blade loading and, consequently, the pitch controller are however not focused on all frequencies occurring in the flow. Especially the smaller eddies and higher frequencies are not of interest, because they do not contain sufficient energy to significantly impact the blade loading. Furthermore, the pitch rate of the pitch system is another limitation: some flow perturbations change just too fast for a pitch system to respond to. The pitch controllers are therefore mostly interested in the low frequencies, i.e. the large eddies containing the bulk of the turbulent energy. A time-domain analysis, which the correlation is, is then only partly useful. A frequency-domain analysis can offer vital information into the turbulent eddies of interest.

Representing the discretely-sampled velocity in the frequency domain requires a discrete Fourier transform. The transform is applied through Welch's spectral density estimation method. The velocity signals are split into segments of a certain size. These segments generally have a window applied to them to make the signal periodic, which the Fourier transform assumes, and therefore reduce edge effects and spectral leakage. To reduce the effect of altering the signal through windowing, the segments are overlapped by a certain amount. Finally, the discrete Fourier transform of each segment is computed and the squared magnitude of the complete result provides the energy spectrum.

A typical Hann window with 50% overlap is used in the analysis. The window size requires some analysis due to the influence on the frequency resolution, minimum frequency and amount of averaging and noise reduction. All the velocity signals contain 3000 samples with a sample frequency,

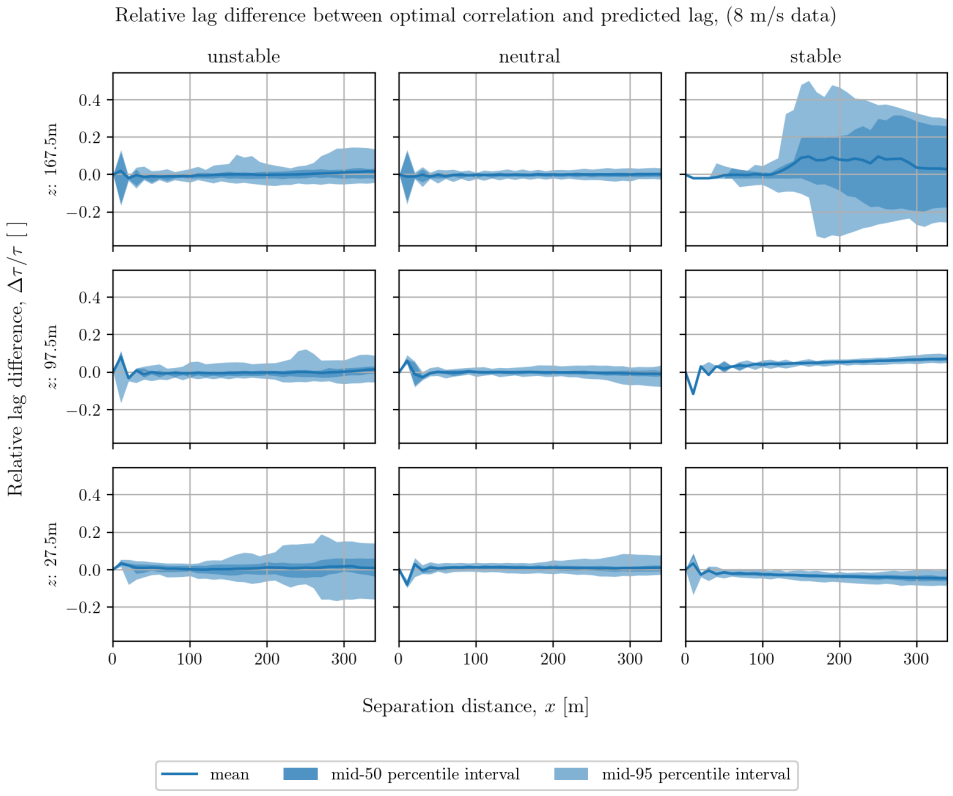

Figure 5.11: Relative delay difference between optimal and expected, data set 1

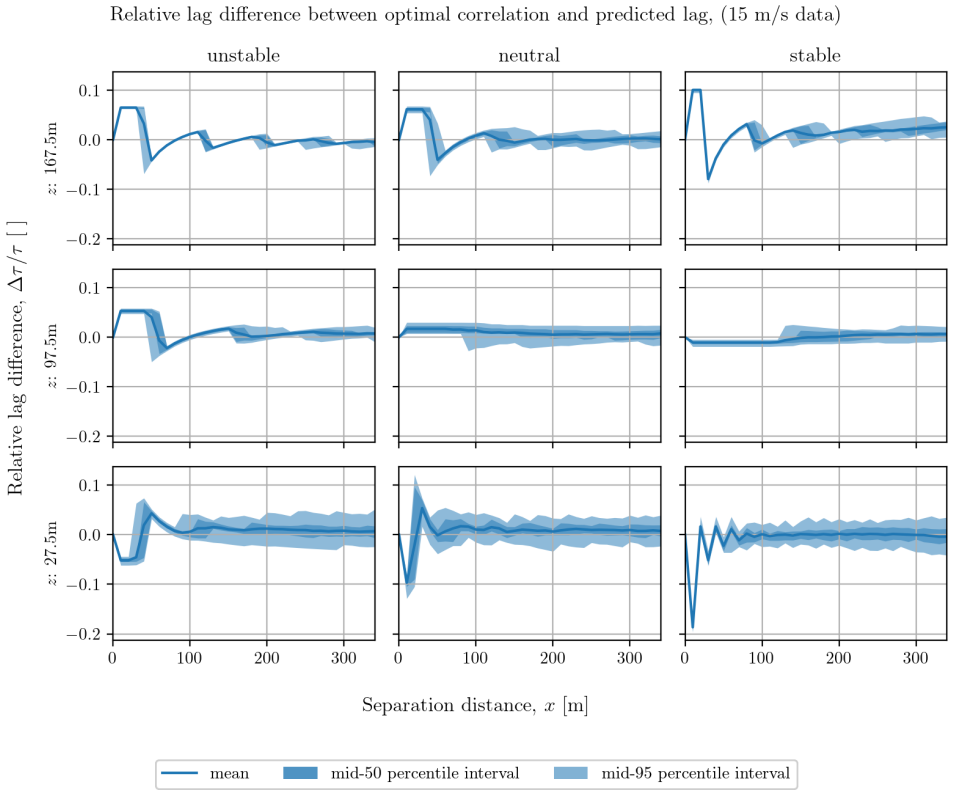

Figure 5.12: Relative delay difference between optimal and expected, data set 2

f_s, of 3 Hz. This provides a hard limit on the highest frequency that can be represented by the temporal grid of the velocity signal in the form of the temporal Nyquist frequency:

$$f_{\max,t} = f_{\text{Nyquist},t} = \frac{f_s}{2} = 1.5 \text{ Hz} \tag{5.7}$$

If the Fourier transform were to be applied to the entire velocity signal without segmentation, the lowest frequency, excluding 0 Hz, that the temporal grid could represent is:

$$f_{\min,t} = \frac{1}{2t_{\text{sig}}} = \frac{f_s}{2N_t} = 5 \cdot 10^{-4} \text{ Hz} \tag{5.8}$$

The result of Welch's method will be the energy determined for a number of frequency bins. The width of these bins, and therefore the frequency resolution of the spectrum, depends on the sampling frequency and the window size, N_w:

$$\Delta f = \frac{f_s}{N_w} \tag{5.9}$$

Where the zero-bin contains all frequencies below the minimum frequency that the segmented signal can represent. The left edge of the first bin equals the minimum frequency as:

$$f_{\min,w} = \frac{\Delta f}{2} = \frac{f_s}{2N_w} \tag{5.10}$$

If the window size were the entire velocity signal, $N_w = N_t$, the frequency resolution would be 10^{-3} Hz. Any smaller window size would increase the width of the frequency bins and reduce the resolution. At the same time, smaller windows allow for more averaging and therefore reduced noise. A proper window size should therefore strike a balance between frequency resolution and noise reduction. Ideally, the window size should also fit an integer amount of times within the signal. This would avoid having to zero-pad the signal or truncate the signal.

With a standard overlap of 50% a window size of 250 samples provides sufficient averaging without over-averaging. The 3000 samples are then divided into 23 (partly) overlapping windows. The window size is often a power of two to reduce the computation time of the Fourier transform, but this was relaxed in favor of a window size which perfectly fits the signal length. This window size results in a frequency bin width of $1.2 \cdot 10^{-2}$ Hz and a minimum frequency that the segmented signal can represent of $6 \cdot 10^{-3}$ Hz, using Equations 5.9-5.10, respectively.

As foreshadowed by determining the temporal Nyquist frequency, there is also a spatial equivalent. The spatial grid used by the LES also has a minimum and maximum frequency it can represent. With a longitudinal spacing of 10 m the smallest wave of the resolved scales (and consequently the highest wavenumber) is the spatial Nyquist wavenumber:

$$\kappa_{\max,x} = \kappa_{\text{Nyquist},x} = \frac{2\pi}{\lambda_{\min}} = \frac{2\pi}{2\Delta x} = \frac{\pi}{10} \text{ m}^{-1} \tag{5.11}$$

Wavenumber and frequency are related through the phase speed of the relevant wave:

$$\kappa = \frac{2\pi f}{u_p} \tag{5.12}$$

When substituting the mean velocity for the phase speed, it is inherently assumed that the wave travels at the mean velocity. This therefore partly assumes Taylor's frozen turbulence when converting between wavenumber and frequency. As it is only assumed for conversion between these domains and no importance is placed on very specific frequencies, the effect is negligible. The approximated spatial Nyquist frequency then becomes:

$$f_{\max,x} = f_{\text{Nyquist},x} = \frac{\overline{u}\kappa_{\max,x}}{2\pi} = \frac{\overline{u}}{2\Delta x} \tag{5.13}$$

The spatial Nyquist frequency will be the limiting case when:

$$f_{\max,x} < f_{\max,t} \tag{5.14}$$

$$\frac{\overline{u}}{2\Delta x} < \frac{f_s}{2} \tag{5.15}$$

$$\overline{u} < f_s \Delta x = 30 \text{ m/s} \tag{5.16}$$

Both data sets will therefore be limited by the spatial Nyquist frequency. All higher frequencies resulting from the Fourier transform will therefore constitute random noise.

Lastly, the spatial minimum frequency must be determined, because it may dictate the window size. The window size has been set such that it provides adequate, but not excessive averaging. If the spatial minimum frequency is however higher than the previously computed minimum frequency of this window of $6{\cdot}10^{-3}$ Hz, the window size can either be adjusted or the resulting spectrum will show random noise for frequencies below the spatial minimum frequency. The spatial minimum frequency does not depend on the spatial domain used in this research, but depends on the larger LES-domain of which a snapshot has been used. The larger domain is 4 km in the longitudinal direction, as mentioned in Section 4.3. The resulting spatial minimum wavenumber that the LES-domain can represent is:

$$\kappa_{\min,x} = \frac{2\pi}{\lambda_{\max}} = \frac{2\pi}{2L_{\text{LES},x}} = \frac{\pi}{4000} \text{ m}^{-1} \tag{5.17}$$

The approximated spatial minimum frequency then becomes:

$$f_{\min,x} = \frac{\overline{u}\kappa_{\min,x}}{2\pi} = \frac{\overline{u}}{2L_{\text{LES},x}} \tag{5.18}$$

This spatial minimum frequency is larger than the minimum frequency of the window if:

$$f_{\min,x} > f_{\min,w} \tag{5.19}$$

$$\frac{\overline{u}}{2L_{\text{LES},x}} > \frac{f_s}{2N_w} \tag{5.20}$$

$$\overline{u} > \frac{f_s L_{\text{LES},x}}{N_w} = 48 \text{ m/s} \tag{5.21}$$

Neither data set contains velocities even close to this threshold. The chosen window size is therefore far from being too large compared to the spatial domain. The lowest frequencies appearing in the spectrum will therefore represent actual flow data and not random noise.

5.1.7 TFTH: Energy spectrum

Welch's method is applied to the temporal longitudinal velocity signal of each grid point to determine the auto-spectral density. The resulting longitudinal energy spectrum, in the form of the squared magnitude, shows the energy density in terms of frequency. In order to compare the spectrum to the typical turbulent kinetic energy spectrum (Figure 4.1), the energy spectrum can be converted to a wavenumber basis by scaling the spectrum:

$$E(\kappa) = \frac{u_p}{2\pi} E(f) \tag{5.22}$$

To greatly reduce the complexity, the frequency-dependent phase speed is replaced by the mean velocity of each grid point. Again, this inherently assumes part of Taylor's frozen turbulence in the conversion. Finally, the spectra of all grid points on the same horizontal plane are compared to obtain a spread. This requires the spectra to be evaluated at the exact same wavenumbers, which is not the case due to small differences in the mean velocity used in the conversion. Due to the

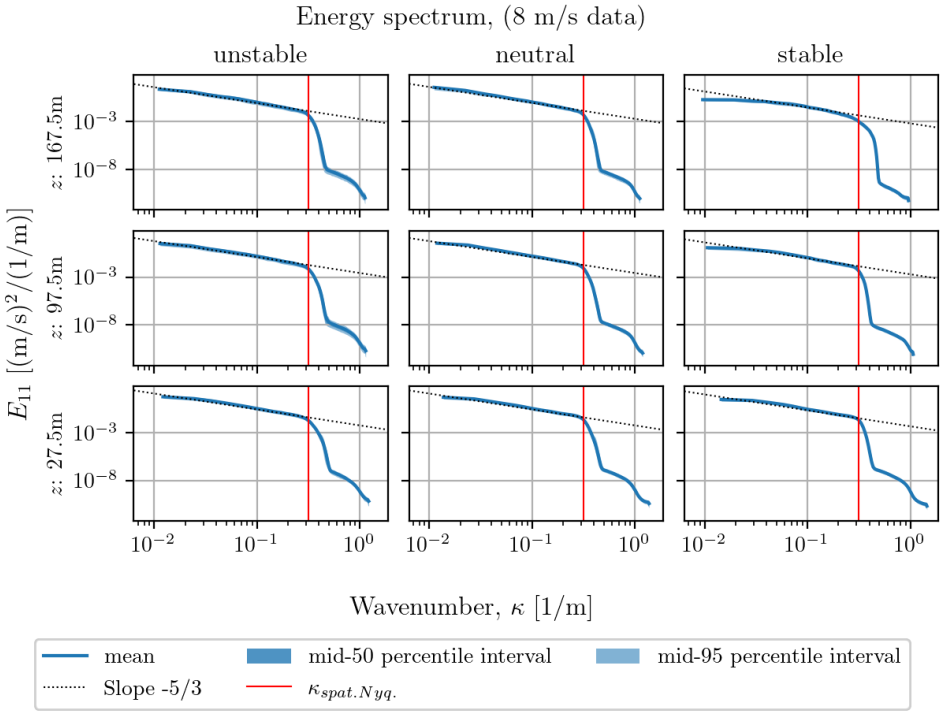

Figure 5.13: Longitudinal energy spectrum in wavenumber, data set 1

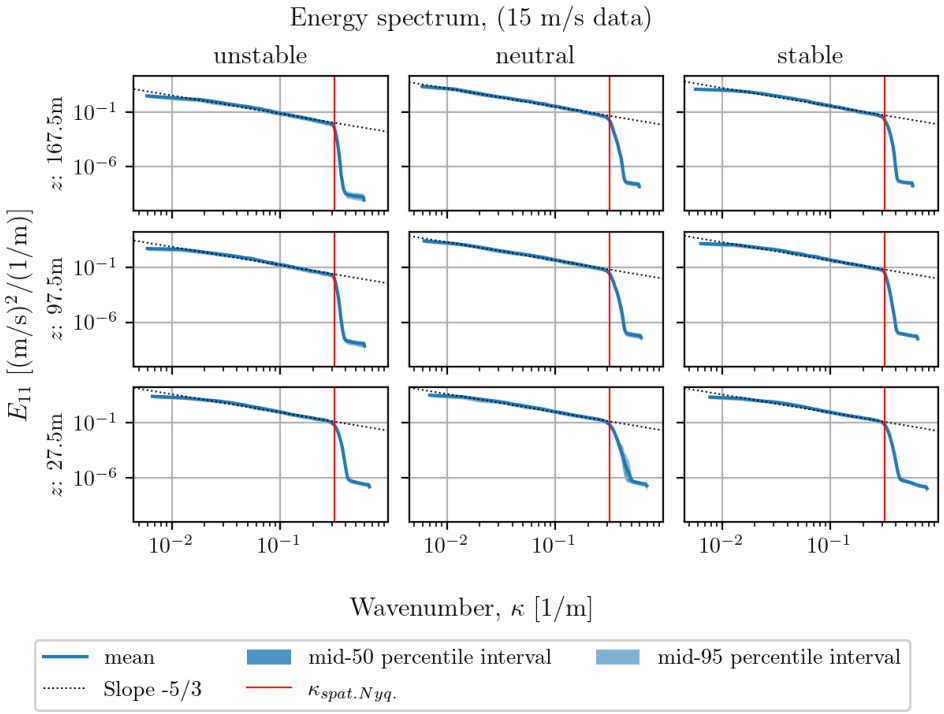

Figure 5.14: Longitudinal energy spectrum in wavenumber, data set 2

relatively minor differences a linear interpolation is applied to adjust the spectrum to a common wavenumber range. Figures 5.13 and 5.14 show the energy spectrum of the longitudinal velocity in terms of wavenumber for both data sets. Appendix C.6 shows the longitudinal energy spectrum as a function of frequency, which does not require any assumption to be made.

The energy spectra of both data sets show a decrease closely matching with the -$\frac{5}{3}$ slope line. This places the analyzed wavenumbers decidedly within the inertial subrange of turbulence. The crossover from the energy-containing range to the inertial subrange occurs around $6\kappa_0$, where κ_0 represents the eddies with a length scale comparable to the flow scales, as mentioned in Section 4.1. The crossover would then roughly be:

$$6\kappa_0 \approx 6 \cdot \frac{2\pi}{L} = \frac{12\pi}{4000} = 9.4 \cdot 10^{-3} \text{ m}^{-1} \tag{5.23}$$

The wavenumbers for which the spectra are determined, start just above this crossover wavenumber. The spectra all seem to deviate slightly from the inertial subrange slope line at the lowest wavenumber. This may therefore be due to the proximity to the energy-containing range where the spectra level off.

Both spectra also show a sharp decline in the higher wavenumbers. However there is no physical cause for the behavior as it occurs at wavenumbers above the spatial Nyquist wavenumber (vertical red line). The spectral drop is therefore purely an artifact of random noise from the spatial grid being unable to represent these eddies. Lastly, both spectra show a very tight spread, almost to the point of being a singular line. This effect is exacerbated by the spectra being shown on a log-scale.

The only spectrum that does not follow the slope line everywhere is the highest plane in the stable case of data set 1. This behavior is caused by the significant lateral drift resulting in the flow direction not being aligned. At the larger scales (lower wavenumber) the anisotropy of the eddies is more pronounced. When determining the energy contained in the velocity perturbation, the result will be drastically lower when measuring the unaligned velocity component.

5.1.8 TFTH: Coherence

The spread of the energy spectra is very narrow when plotted on a log-scale, giving the illusion that the energy distribution of the flow does not change much when advecting through the domain. The coherence between two signals better shows the energy transfer between them. The magnitude-squared coherence is determined using cross-spectral density of the two signals and their auto-spectral densities. Similarly to the correlation, the coherence will be determined in the longitudinal direction. The coherence of the longitudinal velocities, u, between the first grid point, $x = 0$, and a longitudinally separated point, x, is defined as:

$$\gamma^2_{0,x}(f) = \frac{|S_{0,x}(f)|^2}{S_{0,0}(f) \cdot S_{x,x}(f)} \tag{5.24}$$

Where S is the complex spectral density and the energy spectrum, shown in the previous section, is its magnitude-square. The dimensionless coherence ranges between zero and one, indicating no relation or a perfect linear relation, respectively. For perfectly frozen turbulence the coherence should be unity for all frequencies or eddy scales. Any reduction in coherence implies that the relation between the two signals is influenced to some capacity by another source, any non-linear relation or noise. Note that coherence not only reduces due to an amplitude change of a certain frequency between the two signals, but also due to a non-constant phase change. Such a non-linear frequency-dependent phase change could indicate that eddies do not travel with the mean velocity. As turbulence and turbulence evolution is highly non-linear, a reduction in coherence is a clear indicator.

Figure 5.15 shows the coherence spread of the neutral case of data set 1 as a function of frequency. Each column of subplots shows the coherence spread of all points with a certain longitudinal separation distance on the same horizontal plane. Appendix C.7-C.9 shows the coherence spread for all

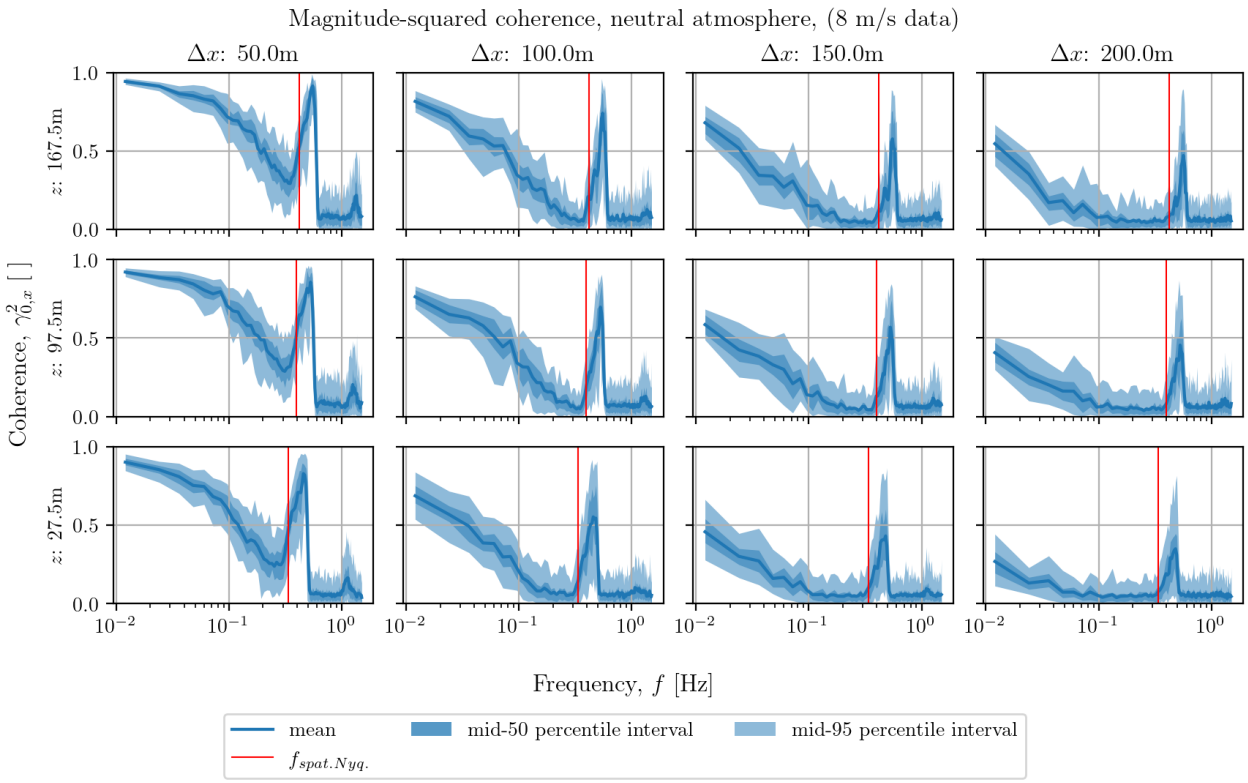

Figure 5.15: Longitudinal coherence, neutral atmosphere, data set 1

other cases. The coherence clearly decreases with higher frequencies, as the wavelength of the higher frequencies becomes progressively smaller compared to the separation distance. And with increasing separation distance, the coherence of even the largest represented eddies decreases drastically. The coherence decay with higher frequencies is because those perturbations, i.e. smaller eddies, evolve at a much faster rate compared to the larger eddies with their longer length- and time scale. The more an eddy can evolve, the lower the coherence. The coherence is therefore directly dependent on the separation time: the separation distance divided by the advection speed. This relation with the coherence is evident as the higher planes, with higher advection speed, show a slower coherence drop compared to the lower planes for the same separation distance.

The maximum spatial frequency that the LES grid can represent has also been indicated by the vertical red line. The coherence has a large peak directly after it, caused by the transition to noise through the spectral drop in the energy spectrum (Figures 5.13-5.14). This drop apparently exhibits a very coherent behavior among all grid points, causing a spike in the coherence. It does not indicate a physical phenomenon and is purely a modeling artifact. It does affect the coherence spread before this spatial Nyquist frequency in some cases, where a slight increase can be seen below this frequency. This is likely a result of spectral leakage due to edge effects.

The mid-50 percentile is generally very tight and the 95 percentile spread shows the same behavior as the mean. To compare all atmospheres in one figure only the mean will be retained as an indicator of the overall coherence. Figures 5.16-5.17 show the mean coherence of a number of separation distances as solid lines for both data sets. The dotted lines will be explained later. It is immediately clear that the previous observations of only the neutral case still hold: the coherence decays with higher frequencies and the coherence also decreases with increasing separation time. The last part is especially obvious when comparing the two data sets: data set 2 has a much slower coherence decay due to the analyzed domain having the same spatial length, but being much shorter when considering flow duration.

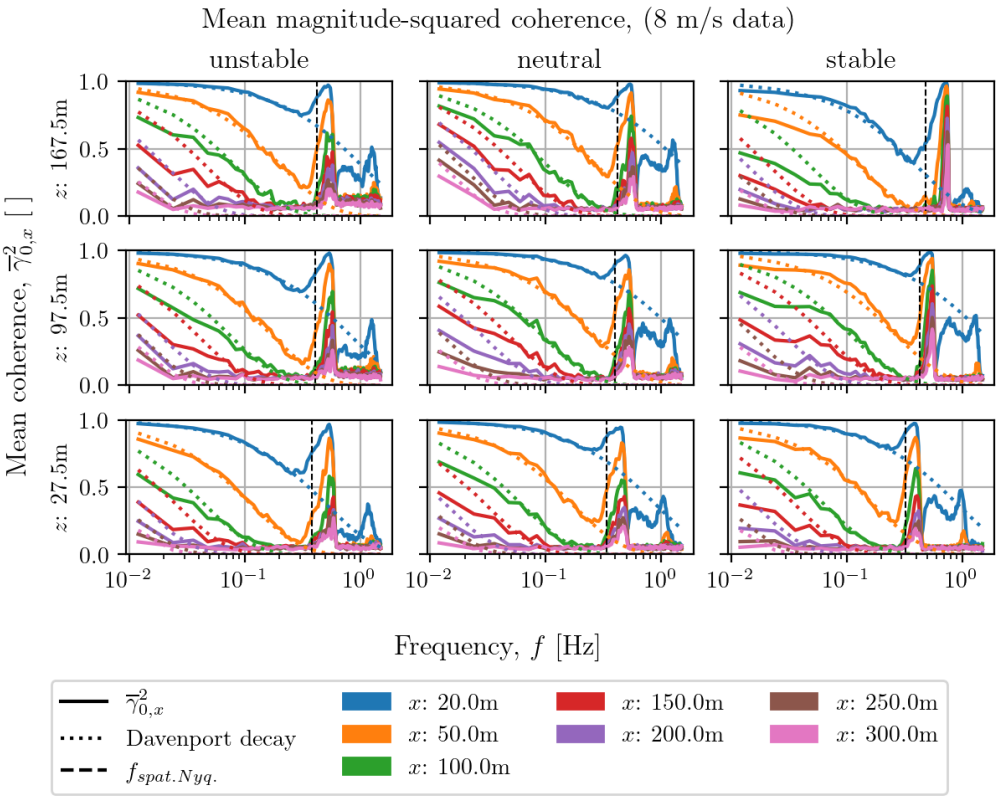

Figure 5.16: Mean magnitude-squared coherence in frequency, data set 1

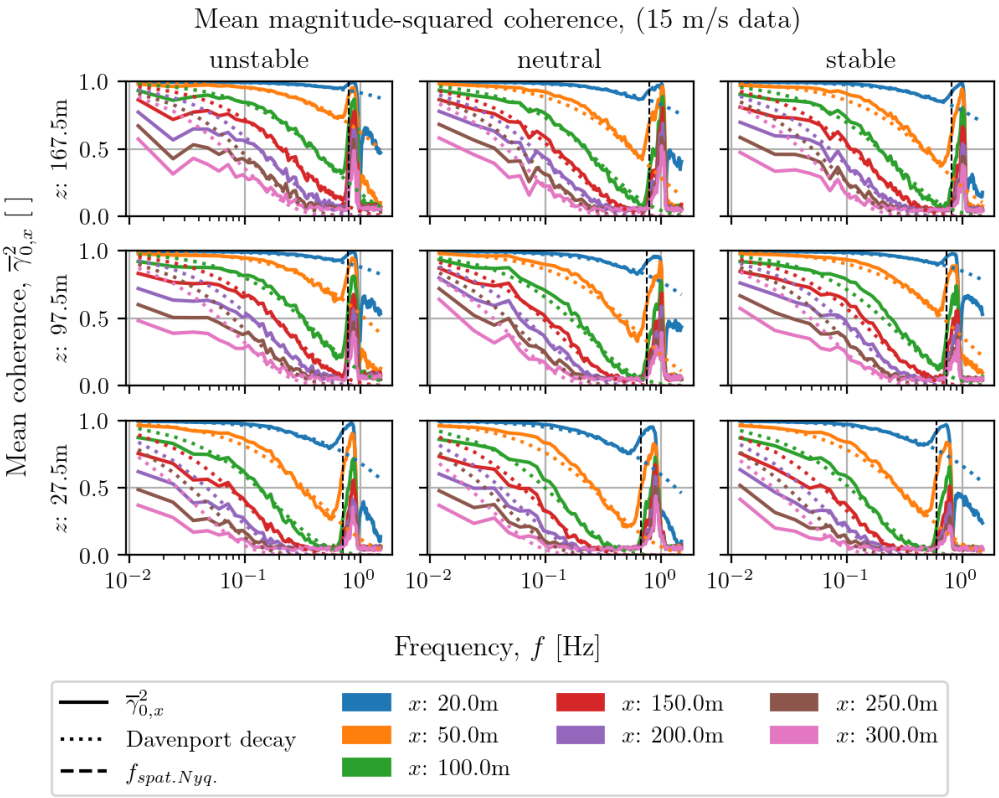

Figure 5.17: Mean magnitude-squared coherence in frequency, data set 2

Keep in mind that the low coherence for high frequencies is not a problem for two reasons: IPC-controllers cannot react quickly enough to the perturbations of small time scales and, considering the energy spectra of Figures 5.13-5.14, the energy contained in these higher frequencies is orders of magnitude lower compared to the energy in the low frequencies.

Across the different atmospheric stabilities, the coherence generally shows very similar behavior. Of course, the stable case of data set 1 is an exception due to the significant lateral drift mentioned in previous sections. In data set 1 the neutral case seems to have the lowest decay, whereas the unstable case seems to perform slightly better in data set 2.

5.1.9 TFTH: Phase

Inspecting the phase difference between the spectra of each of the two analyzed points can provide additional insights in the reason of the decaying coherence. The phase information is contained in the complex cross-spectral density through the angle composed of the real and imaginary part:

$$\phi_{0,x}(f) = \angle S_{0,x}(f) \tag{5.25}$$

The resulting spectrum shows the phase difference per frequency. From Taylor's Frozen Turbulence hypothesis, where all eddies are assumed to advect with the mean flow, the phase difference is expected to follow a linear relation with frequency:

$$\phi_T(f) = 2\pi \left(\frac{\Delta x}{\lambda} - k(f) \right) = 2\pi \left(\frac{\Delta x}{\overline{u}} f - k(f) \right), \qquad \text{with } k(f) = \text{floor} \left(\frac{\Delta x}{\overline{u}} f \right) \tag{5.26}$$

Where k is added to bound the phase delay between 0 and 2π. In the ideal case the Taylor phase delay and the computed phase delay would be equal, but Figure 5.18 shows, for the stable case of data set 1, that this is not the case. The other phase delay spectra can be found in Appendix C.10-C.12. The phase delay of the stable case is shown here to illustrate how the spread of the phase delay becomes wider and wider with increasing separation distance. This widening of the spread and the mean being unable to follow the Taylor phase delay is detrimental for the coherence. At low separation distances, this occurs only at the highest frequencies before the spatial Nyquist frequency, but the effect worsens with increasing separation distance where even the lowest frequencies become impacted.

Whenever the mean deviates from the Taylor phase and the spread is still relatively narrow, it indicates that eddies of these frequencies advect at a different velocity compared to the mean velocity. If the actual phase delay is higher than the Taylor phase delay, the elapsed time of the perturbations of that frequency is longer than expected, indicating that they advect at a slower pace than the mean velocity.

At high frequencies the phase delay spread becomes so wide that the actual phase delay is practically random at these frequencies. This is caused by the larger amounts of cycles these frequencies complete within that separation distance. Any small change in advection velocity of that perturbation or a larger perturbation evolving towards higher frequencies may result in a small phase delay in the first cycle. Due to the compounding effect of consecutive cycles, the final phase delay can be greatly affected.

Lastly, the phase delay of the top plane of the stable case is clearly affected by the lateral drift with the spread increasing at much lower frequencies compared to the other two heights.

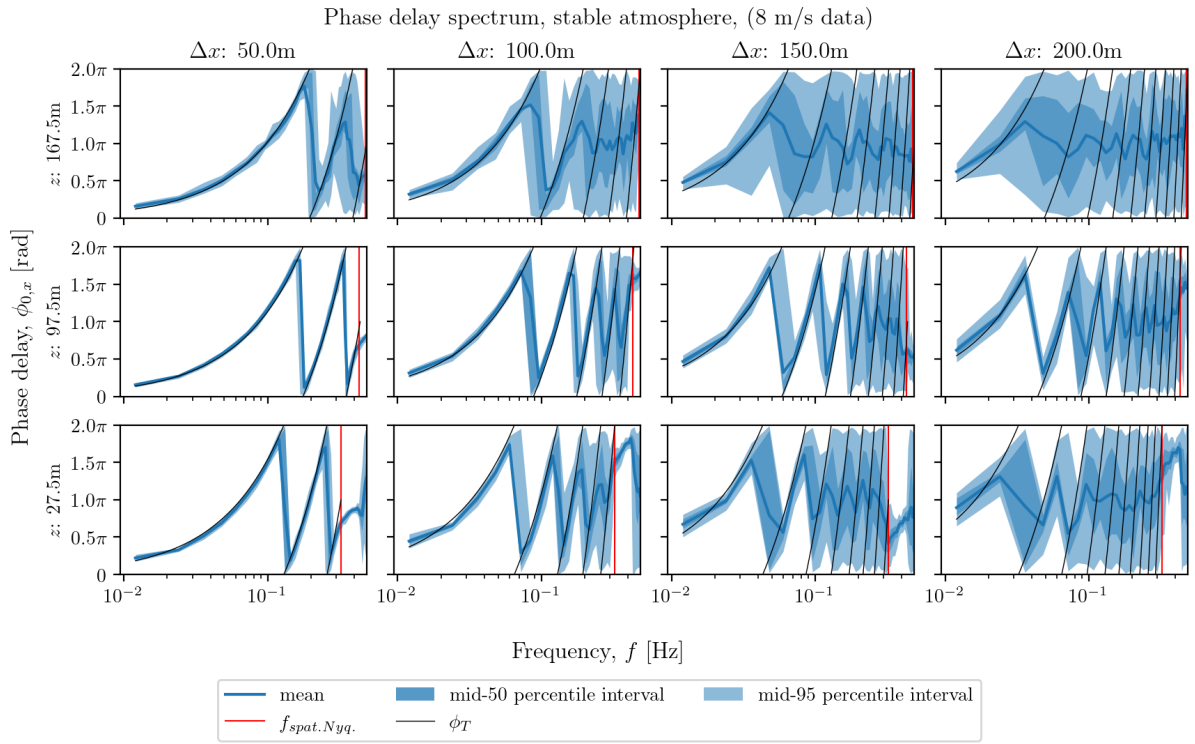

Figure 5.18: Phase delay spectrum of the stable case compared to the Taylor phase delay, data set 1

5.1.10 TFTH: Coherence and exponential decay

An estimate for the validity of Taylor's Frozen Turbulence hypothesis has already been determined using correlation data. With the frequency-domain data now available, it may be possible to refine or adjust this estimate. This will be attempted using a model based on Davenport Geometric Similarity which was extended to horizontal coherence by Pielke & Panofsky[30] based on measurements in the surface layer below 30 m. It notes that the coherence decay with frequency exhibits an exponential decay and can therefore be approximated with:

$$\gamma^2_{\Delta x}(f) = e^{-af\Delta x/\overline{u}} \tag{5.27}$$

Where a is a non-dimensional decay parameter, which is adjusted to obtain a good fit with the actual coherence. To link the coherence to the cross-correlation and Taylor's hypothesis, an equation for the 'pseudo-Lagrangian' correlation coefficient was derived by Panofsky & Mizuno[31]:

$$\rho_p(t) = \int_0^\infty F(f)\sqrt{\gamma^2(f,t)}\,\mathrm{d}f, \qquad \text{with } F(f) = \frac{\sqrt{S_1(f)S_2(f)}}{\sigma_1\sigma_2} \tag{5.28}$$

The pseudo-Lagrangian correlation coefficient is the peak cross-correlation and is therefore an approximation of the correlation when traveling with the flow. The coherence is shown as a function of frequency and time, this time represents the flow travel time between the measured spectra for the specific frequency.

This equation was derived using the inverse Fourier sine and cosine transform on the cross-spectrum. The cross-spectrum is the Fourier transform of the cross-covariance and also related to the coherence, as shown in Equation 5.24 where it is represented as $S_{0,x}(f)$. The cross-correlation coefficient is the cross-covariance normalized by the product of the standard deviations of the two signals, $\sigma_1\sigma_2$.

Height [m]	$f = 2\pi/T_x$ [Hz]					
	Data set 1			Data set 2		
	unstable	neutral	stable	unstable	neutral	stable
167.5	0.26	0.39	0.88	0.48	0.33	1.42
97.5	0.31	0.38	0.91	0.48	0.37	1.22
27.5	0.42	0.52	0.86	1.01	0.45	1.04

Table 5.3: Frequency where $fF(f)$ is estimated to peak for each case

To simplify Equation 5.28 further, the auto-spectra are assumed to be equal[30]. Combined with the exponential decay function in terms of separation time, the equation becomes:

$$\rho_p(t) = \int_0^\infty F(f) e^{-(a/2)ft} \, \mathrm{d}f, \qquad \text{with } F(f) = \frac{S(f)}{\sigma^2} \tag{5.29}$$

The validity distance of Taylor's hypothesis can now be determined by considering that the cross-correlation must remain approximately unity. Mizuno & Panofsky[32] state that this is sufficiently satisfied as long as:

$$aft < 1 \quad \rightarrow \quad e^{-(a/2)ft} < e^{-1/2} \approx 0.6 \tag{5.30}$$

When aft does exceed unity, the correlation may still remain large if the energy contained in the frequencies beyond is small. The normalized spectral density F is then small, such that the contribution to the integral is limited. For small frequencies, $\mathcal{O}\left(1/(4T_x)\right)$, the spectral density is roughly constant, therefore the term $fF(f)$ in the integral peaks at a certain frequency dependent on the integral time scale, typically around $2\pi/T_x$. After which the term quickly drops and the contribution to the correlation is limited. Table 5.3 shows this frequency estimate, which is above the spatial Nyquist frequency of some of the cases. The condition for high correlation is then determined to be[32]:

$$\Delta x_{\mathrm{TFTH}} = L_x \frac{2\pi}{a} \tag{5.31}$$

This model would provide a very simple condition for determining the upper limit of the validity distance of Taylor's Frozen Turbulence hypothesis, without having to resolve the entire frequency spectrum. Only the frequencies where the coherence decays are required. However, the dotted lines in Figures 5.16-5.17 represent the Davenport exponential decay function. It is immediately clear that no good fit can be found for all separation distances. In data set 1, all coherence lines belonging to a separation distance of 100 m or higher show a very poor fit for low frequencies. In data set 2, this crossover occurs somewhere between 100 m and 150 m. In these cases the exponential decay greatly overestimates the coherence of the low frequencies.

Figure C.26 shows the decay parameter a of data set 2 which provided the best fit. Appendix C.13 shows the figures for both data sets. The marker colors correspond to the same colors in the mean coherence figures (Figures 5.16-5.17). The shape of the marker indicates the horizontal plane it belongs to and the line type indicates the atmospheric stability. All cases seem to show a slow increase with larger separation distances. Mizuno & Panosfky[32] noted that the dependency with distance was only seen in stable atmospheres and noted that a "appeared" constant with separation distance. The analyzed cases in this report seem to show a dependency on separation time, and consequently also on separation distance, for all atmospheric cases.

Wetz et al.[33] encountered a similar result where no good fit could be found for larger separation distances, noting that this occurred around the integral length scale. Table 5.4 presents the previously computed integral length scale again and the distance up to where a reasonably good fit could be found with the exponential decay function. In the unstable and neutral cases the integral length scale is around 2-4 times larger than the largest good fit distance. Only the stable case has the two distances being somewhat close together.

Table 5.4 also contains the distance for which Taylor's Frozen Turbulence should be valid using the mean of only the parameters from the good fits and using Equation 5.31. It is immediately clear

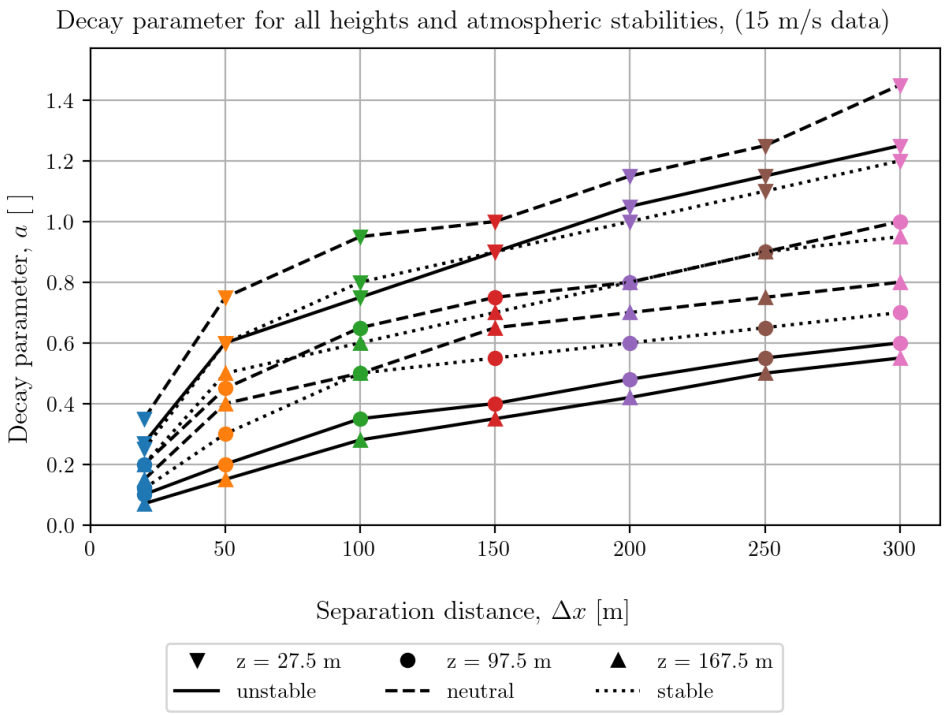

Figure 5.19: Decay parameter over distance, data set 2

Height [m]		Data set 1			Data set 2		
		unstable	neutral	stable	unstable	neutral	stable
167.5	L_x [m]	219	138	41	244	351	98
	Good fit [m]	50	50	20	100	100-150	100
	Δx_{TFTH} [m]	2293	1993	723	9199	5189	1421
97.5	L_x [m]	164	126	63	177	313	68
	Good fit [m]	50	50	50	100	100-150	100
	Δx_{TFTH} [m]	1421	1799	851	5133	3837	1393
27.5	L_x [m]	163	117	46	157	230	81
	Good fit [m]	50	50	50	50-100	100	100
	Δx_{TFTH} [m]	975	1246	526	1827	2115	925

Table 5.4: Validity distance based on Davenport decay with only good fits

that this result in incredibly large distances compared to integral length scale and the correlation cut-off distances from Table 5.2. Additionally, the coherence of the largest separation distances computed, show that already at these distances these frequencies are almost entirely unrelated. The result is especially distorted due to having to neglect the parameters of the larger separation distances, because of the poor fit at low frequencies.

So there is a twofold problem with applying this model to estimate the validity distance:

1. No good exponential decay fit can be found for separation distances larger than 50 m and 100 m, for the two cases respectively
2. The decay parameters are very low, leading to a massive upper limit of the validity distance

The first problem could be caused, at least partly, due to the limited number of cycles these frequencies have in the segmented signal resulting in a small amount of data. This lower sample size combined with the effects of windowing and averaging may lead to inaccuracies in the representation of the power and phase at these frequencies. While these effects may not be noticeable in the energy spectra, the coherence is more sensitive to these errors, due to the dependence on three separate

spectra.

All decay parameters, and especially those that were usable, are considerably lower than typical values of 3 to 8[33]. These much lower parameters are possibly due to the low turbulence intensity of the cases considered here. As mentioned before, coherence decreases whenever a non-linearity, other source or noise affects the signal. Higher turbulence intensity increases the energy available in the turbulence and in the energy cascade. As a result the chaotic nature of turbulence is exacerbated and the coherence between two signals decreases. Another possible reason why the model does not provide a good fit, maybe due to it, originally, only being considered for heights below 30 meters[32]. If this were the issue, then only the lowest plane considered in this research should provide an accurate estimate, but this is clearly not the case.

5.1.11 TFTH: Cross-correlation of a frequency band

The exponential decay model of the previous section was sadly unable to provide a meaningful estimate of the validity distance. Therefore another approach based on the relation between the cross-covariance and the cross-spectrum will be used:

$$R_{0,x}(\tau) = \mathcal{F}^{-1}\left(S_{0,x}(f)\right) \tag{5.32}$$

Normalizing this equation results in the cross-correlation coefficient. The cross-correlation of the entire time-domain signal has already been demonstrated in Section 5.1.4. This constituted the cross-correlation of all frequencies contained in the flow. When computing the cross-correlation based on the cross-spectrum in the frequency domain, certain frequency bands can first be isolated. The highest frequency of interest for an IPC-controller is typically around 0.1 Hz[34]. The cross-spectrum will therefore be modified to only contain data for the frequencies below it. All values for frequencies above 0.1 Hz are set to zero. This acts like a simple low-pass filter on the available frequencies:

$$S_{0,x(LP)}(f) = \begin{cases} S_{0,x}(f) & \text{for } f \leq 0.1\text{Hz} \\ 0 & \text{for } f > 0.1\text{Hz} \end{cases} \tag{5.33}$$

Note that the minimum frequency of the cross-spectrum is determined by the minimum frequency of the windowing (Equation 5.10), which is $1.2 \cdot 10^{-2}$ Hz. The frequency band that will be analyzed therefore roughly spans from 0.01 Hz to 0.1 Hz. The LES flow data contains frequencies much lower than 0.01 Hz, but these cannot be represented by Welch's method due to the smaller window size required for adequate averaging and noise reduction.

After taking the inverse Fourier transform of the filtered cross-spectrum, the resulting cross-covariance must be normalized to obtain the cross-correlation coefficient. By definition the correlation coefficient of the cross-covariance measured at the same point at zero delay, $R_{0,0}(0)$, must be unity. It can therefore be used to normalize all other cross-covariances to obtain the cross-correlation coefficient:

$$\rho_{0,x}(\tau) = \frac{R_{x,0}(\tau)}{R_{0,0}(0)} = \frac{\mathcal{F}^{-1}\left(S_{0,x(LP)}\right)}{\mathcal{F}^{-1}\left(S_{0,0(LP)}\right)|_{\tau=0}} \tag{5.34}$$

Of the resulting cross-correlation coefficients as a function of delay only the peak is retained per grid point, $\max(\rho_{0,x})$. This roughly results in the correlation coefficient at the delay where the advected perturbations reach the other measurement location. Figures 5.20-5.21 show the spread of the cross-correlation coefficients of this specific frequency band as a function of separation distance. For comparison the mean of the cross-correlation coefficients of the overall flow, as determined in Section 5.1.4, is added. Expectedly, the correlation of the specific frequency band is lower than the mean of the overall flow, as it covers a band of frequencies in the inertial subrange. The overall mean also contains the contributions of the much lower frequencies with longer time scales which contain the bulk of the energy and therefore influence the correlation more significantly.

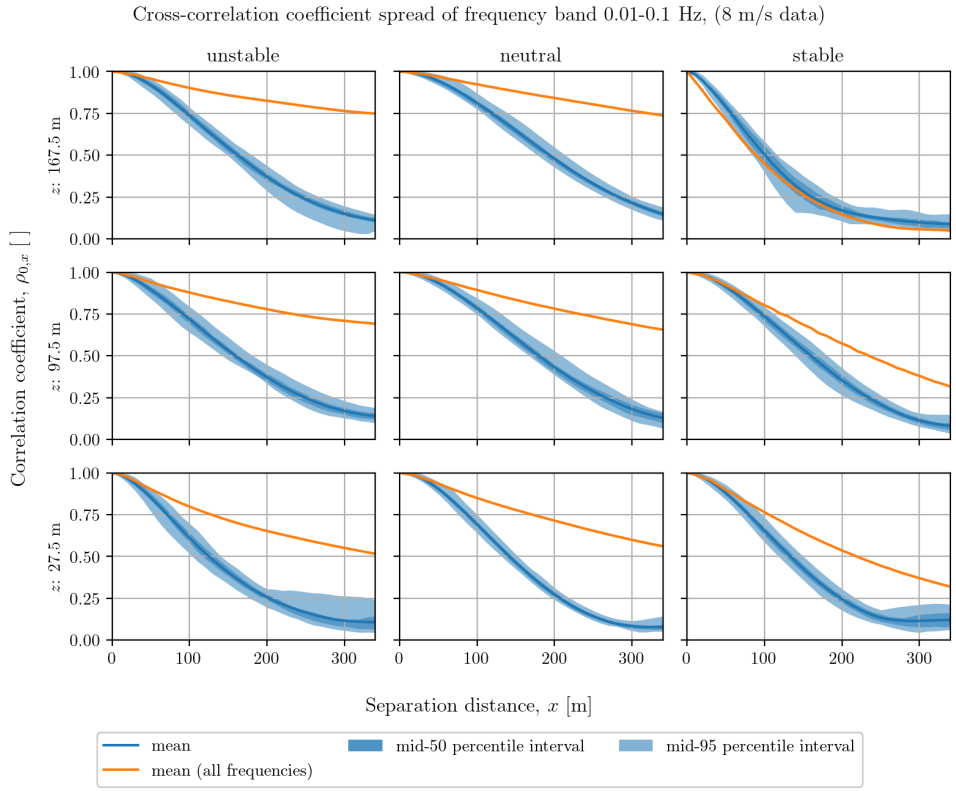

Figure 5.20: Cross-correlation spread of frequency band compared to overall mean, data set 1

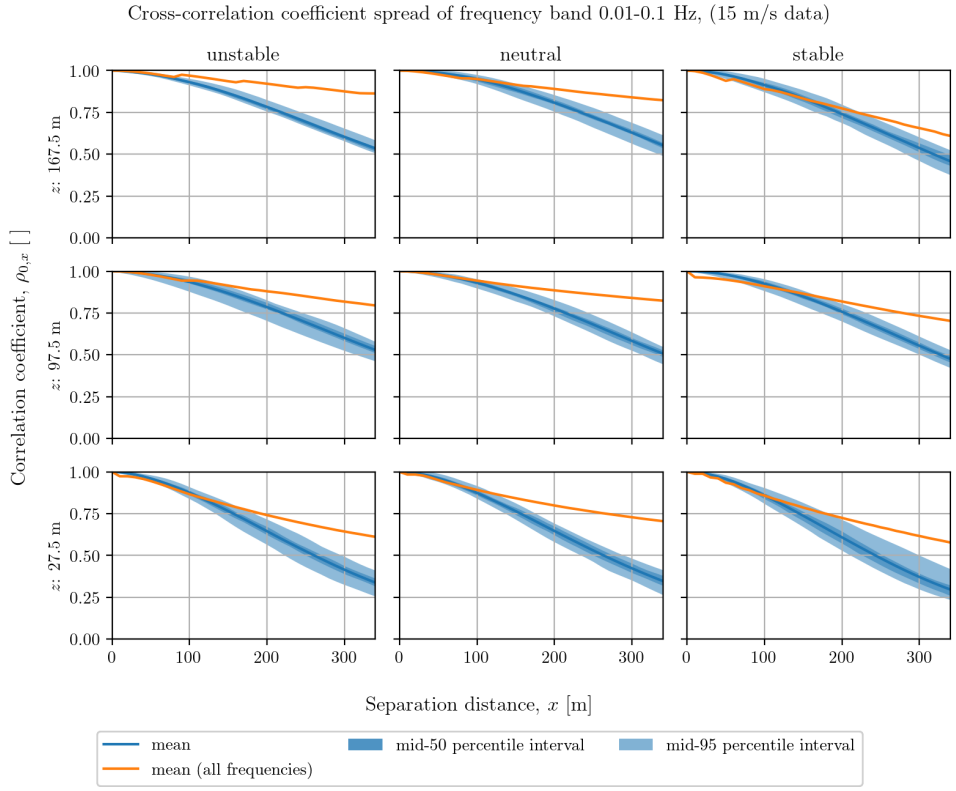

Figure 5.21: Cross-correlation spread of frequency band compared to overall mean, data set 2

Height [m]	Cut-off criterion: $\rho_{a,b}(t_{a\to b}) \leq 75\%$	Mean distance to cut-off [m]					
		Data set 1			Data set 2		
		unstable	neutral	stable	unstable	neutral	stable
167.5	overall	340	320	40	>340	>340	220
	0.01 - 0.1 Hz	100	120	60	220	240	200
97.5	overall	230	230	120	>340	>340	280
	0.01 - 0.1 Hz	100	120	100	230	220	210
27.5	overall	130	170	110	190	270	180
	0.01 - 0.1 Hz	80	90	80	160	160	150

Table 5.5: Mean distance to cut-off for overall cross-correlation at expected delay and cross-correlation of frequency band

Apart from the stable case of data set 1, there is no significant difference between the several atmospheric conditions. The stable case of data set 1 shows clearly that the lateral drift is destructive to the correlation of all frequencies. The effect also seems to be independent of the frequency band as both means are very similar.

Similar to Section 5.1.4 an estimate of the validity of Taylor's Frozen Turbulence hypothesis is determined using the same criterion for the cross-correlation. Table 5.5 shows the 75% cut-off criterion for both the cross-correlation of the frequency band and a repeat of the overall cross-correlation. Note that for the validity of the hypothesis, the cross-correlation must be large, preferably unity. The choice for 75% remains somewhat arbitrary, as mentioned before. The table shows that the validity distance of this frequency band is more dependent on mean velocity than height or atmospheric stability.

6 Conclusion

One of the most impactful and complex-to-validate assumptions made by the simplified wind model is Taylor's Frozen Turbulence hypothesis. The validity of which has been researched by analyzing six atmospheric cases (three atmospheric stabilities each for two mean velocities). The data for these cases were produced using Large Eddy Simulations, which provided an optimum between accuracy, data quantity, control over the conditions and ease-of-access. All cases had relatively low turbulence intensity.

Taylor's Frozen Turbulence hypothesis consists of two aspects: the turbulent eddies being frozen and unchanging and them advecting with the mean velocity. The cross-correlation of longitudinal velocity signals between to longitudinally-separated points analyzed at the expected delay combined the two aspects together. The expected delay was defined as the time required for a flow particle traveling with the flow to reach the downstream measurement location. This cross-correlation showed the large impact of mean velocity and lateral drift or misalignment. The impact of the mean velocity was attributed to measuring the cross-correlation with regards to the separation distance and not separation time. Comparing different heights showed that the cross-correlation improves, both in terms of its mean and the spread, with height due to the reduced turbulence intensity and the higher velocities leading to a shorter separation time. The unstable and neutral case were generally comparable in performance, with the unstable case generally having a larger spread due to increased turbulence production. The stable case with its turbulence-damping effect due to buoyancy, produced the worst correlation performance.

Three cut-off criteria were presented as possible guidelines for judging the validity distance of Taylor's Frozen Turbulence. These criteria were 75% cross-correlation at expected delay, 20% auto-correlation and the integral length scale. The integral length scale proved to be the most conservative, though the other cut-offs are based on an arbitrary choice. The 75% cross-correlation is for example nothing more than a large number, it is not based on an allowable error.

Transforming the data to the frequency domain, allowed for a coherence analysis of a number of frequencies in the inertial subrange. At low separation distances the coherence of the lowest available frequencies was approximately unity and the higher frequencies showed some coherence decay due to their relatively smaller time- and length scales. The coherence decayed more and more with increasing separation distance as the flow perturbations had more and more time to develop and evolve. This also resulted in the phase drifting from the expected phase based on the mean velocity.

After unsuccessfully applying a coherence decay model to the data, the cross-correlation of a specific frequency band (0.01 - 0.1 Hz) was analyzed. This band covered all available frequencies below a typical IPC-controller cut-off. The cross-correlation of this band decayed faster than the overall cross-correlation, due to these frequencies having smaller time- and length scales compared to the lower, energy-containing frequencies which dictate the overall cross-correlation. A similar estimate was provided based on the 75% cut-off, which was therefore also lower.

The usefulness of this research is limited if it is not followed-up by more analysis. On its own, this research is mostly a number of qualitative statements on what affects the validity distance of Taylor's Frozen Turbulence. This research is not an end-all be-all analysis providing a fixed validity distance that can be used as-is in a predictive wind model. It shows the behavior of the cross-correlation for a number of cases. The estimates based on the cut-off criteria are purely ballpark values; for the current atmospheric conditions the validity distance is in the order of tens to hundreds of meters.

The reason that this report is merely a baseline for more research is not only due to the limited number of cases and included effects, but most importantly because there is no allowable error defined. Defining an allowable error dictates the cut-off value for the cross-correlation and consequently the validity distance. The 75% cut-off used here may be too conservative or already too relaxed. This allowable error is specific to the turbine, environment and limiting case used. Limiting behavior may vary greatly whether they are defined by peak loading or fatigue loading, for example. Keep in mind that any real-time predictive wind model also contains other errors, stemming from discretization errors, measurement errors or other approximation errors. These sources of errors combined with

the assumption of Taylor's Frozen Turbulence fill up the error budget. For a fixed error margin, the larger the other errors, the lower the validity distance will be and vice versa. Because any wind model which assumes Taylor's Frozen Turbulence, but is otherwise perfect, will result in a certain minimum error based on the cross-correlations determined for these and similar cases.

Furthermore, this research used general, turbine-agnostic atmospheric data. For example, no turbine blockage or specific terrain effect was included. The turbulence intensity of all cases was also relatively low. It is expected that the cross-correlation will decrease faster with increased turbulence intensity. Turbine blockage may have a similar effect as the turbulence damping of the stable case, resulting in a faster decrease of the cross-correlation.

Lastly, it is specifically repeated for LiDAR measurement strategies that the validity distance is more dependent on separation time than on separation distance. This means that LiDAR measurement strategies should either adjust their measurement distance depending on the mean wind velocity or be set to a fixed distance determined by the limiting case. Additionally, a significant misalignment between the actual flow direction and the measured or computed flow direction may have detrimental effects on the prediction. This is due to the cross-correlation decaying rapidly as shown by the stable case of data set 1.

7 Recommendations

This section will list a number of recommendations for future research. Some of these have already been mentioned in previous sections, but will be repeated here for clarity. The recommendations are grouped based on topic.

Data set

Applying a similar analysis as this research on different data sets will provide additional insights. It is recommended to:

- fine-tune the spatial and temporal domain of the LES snapshot; determine the domains based on the frequencies of interest and the required time resolution
- analyze LES-data with higher turbulence intensity; the correlation and validity distance are expected to decrease due to increased energy and evolution
- include turbine induction; the blocking and distorting effect of a turbine are expected to lead to decreased correlation and could, for example, be modeled by an actuator disk or -line model
- investigate neglecting the vertical velocity; assumed by the simplified wind model, based on a characteristic scale analysis, and should be validated especially in a data set with higher turbulence intensity and preferably also turbine blockage
- investigate transverse correlation; the lateral correlation (ρ_y) of the longitudinal velocity component may provide insights into turbulent structure size and influence LiDAR measurement density

Case importance and limiting behavior

The current analysis was purposefully kept very general, putting no extra significance on specific cases. The next step before actual use of predictive wind modeling is to identify important cases and limiting behavior. It is recommended to:

- identify important atmospheric stability, mean velocity and turbulence intensity cases; depending on the intended use-case some cases may be more frequent or drive the limiting behavior

- determine an acceptable margin of error for cross-correlation cut-off; the cut-off will be driven by intended use-case and its limiting behaviors

Simplified wind model

Even though it has not been included in this report, some improvements and extensions have been made to the simplified wind model, most notably the extension to three dimensions. Many improvements are however still to be made, it is recommended to:

- convert/revert the model to polar coordinates; the Cartesian coordinate system does not use this model's strengths in combating the LiDAR cyclops issue
- improve the grid generation/definition; obtaining more flexible and robust grids allows disregarding uninteresting grid points and consequently improving computation time and memory usage
- parameter test the model; determining the optimal settings of the computational settings may result in increased performance and improved accuracy
- rewrite the code in a more computationally-optimized language; the current model is limited in its allowed grid size and density by computational inefficiencies defeating the purpose of real-time computation

Acknowledgments

I would like to thank my supervisors, Arne, Gerardo and Martijn, for their patience, understanding and support during my graduation assignment. I would like to thank Richard for providing the LES-data and having the time to discuss some of the results. Lastly, I would like to thank Dilan for always being there for me.

References

[1] European Commission and Directorate-General for Climate Action, *Going climate-neutral by 2050 – A strategic long-term vision for a prosperous, modern, competitive and climate-neutral EU economy*. Publications Office, 2019.

[2] "Renewables 2023," tech. rep., International Energy Agency, 2024.

[3] Z. Jiang, Z. Chen, W. Liu, Y. Liu, and X. Wang, "A review of individual pitch control for wind turbines," *Proceedings of the 2016 IEEE 11th Conference on Industrial Electronics and Applications, ICIEA 2016*, pp. 399–404, 2016.

[4] M. Lara, S. P. Mulders, J. W. van Wingerden, F. Vázquez, and J. Garrido, "Analysis of Adaptive Individual Pitch Control Schemes for Blade Fatigue Load Reduction on a 15 MW Wind Turbine," *Applied Sciences (Switzerland)*, vol. 14, no. 1, 2024.

[5] F. Dunne, E. Simley, and L. Y. Pao, "Lidar wind speed measurement analysis and feed-forward blade pitch control for load mitigation in wind turbines," 2010.

[6] E. Bossanyi, "Un-freezing the turbulence: application to lidar-assisted wind turbine control," *IET Renewable Power Generation*, vol. 7, pp. 321–329, 7 2013.

[7] F. Guillemin, H. N. Nguyen, G. Sabiron, D. D. Domenico, and M. Boquet, "Real-time three dimensional wind field reconstruction from nacelle lidar measurements," vol. 1037, Institute of Physics Publishing, 6 2018.

[8] C. Stock-Williams, P. Mazoyer, and S. Combrexelle, "Wind field reconstruction from lidar measurements at high-frequency using machine learning," vol. 1102, Institute of Physics Publishing, 10 2018.

[9] E. S. Sagredo, Ásta Hannesdóttir, J. M. Rinker, and M. Courtney, "Reconstructing turbulent wind-fields using inverse-distance-weighting interpolation and measurements from a pulsed mounted-hub lidar," *Journal of Physics: Conference Series*, vol. 2745, 2024.

[10] A. Borraccino, D. Schlipf, F. Haizmann, and R. Wagner, "Wind field reconstruction from nacelle-mounted lidar short-range measurements," *Wind Energy Science*, vol. 2, pp. 269–283, 2017.

[11] P. Towers and B. L. Jones, "Real-time wind field reconstruction from lidar measurements using a dynamic wind model and state estimation," *Wind Energy*, vol. 19, pp. 133–150, 1 2014.

[12] M. C. Peters, *Internship 2-B Energy: Simplified Wind Modeling*. University of Twente & 2-B Energy, 2022.

[13] R. B. Stull, *An Introduction to Boundary Layer Meteorology*. Kluwer Academic Publishers, 1988.

[14] E.T.A. van der Weide, *Lecture notes in Computational Fluid Dynamics, Lecture 9: Turbulence Modeling and CFD Software*. University of Twente, June 2021.

[15] S. B. Pope, *Turbulent Flows*. Cambridge University Press, 2000.

[16] C. Hirsch, *Numerical Computation of Internal and External Flows*, vol. 1. John Wiley & Sons, Ltd, 1996.

[17] C. Meneveau and J. Katz, "Scale-invariance and turbulence models for large-eddy simulation," *Annual Review of Fluid Mechanics*, vol. 32, pp. 1–32, 2000.

[18] C. H. Moeng and P. P. Sullivan, "Numerical Models: Large-Eddy Simulation," in *Encyclopedia of Atmospheric Sciences: Second Edition*, pp. 232–240, Elsevier Inc., 2015.

[19] A. Nybø, F. Nielsen, J. Reuder, M. Churchfield, and M. Godvik, "Evaluation of different wind fields for the investigation of the dynamic response of offshore wind turbines," *Wind Energy*, vol. 23, 05 2020.

[20] "IEC 61400-1 Wind Energy Generation Systems Design Requirements," tech. rep., International Electrotechnical Commission, 2019.

[21] Y. Chen, F. Guo, D. Schlipf, and P. W. Cheng, "Four-dimensional wind field generation for the aeroelastic simulation of wind turbines with lidars," *Wind Energy Science*, vol. 7, no. 2, pp. 539–558, 2022.

[22] S. N. Gadde and R. J. A. M. Stevens, "Interaction between low-level jets and wind farms in a stable atmospheric boundary layer," *Physical Review Fluids*, vol. 6, p. 014603, Jan 2021.

[23] G. Ren, J. Liu, J. Wan, F. Li, Y. Guo, and D. Yu, "The analysis of turbulence intensity based on wind speed data in onshore wind farms," *Renewable Energy*, vol. 123, pp. 756–766, 2018.

[24] C. L. Archer, B. A. Colle, D. L. Veron, F. Veron, and M. J. Sienkiewicz, "On the predominance of unstable atmospheric conditions in the marine boundary layer offshore of the u.s. northeastern coast," *Journal of geophysical research*, vol. 121, pp. 8869–8885, 2016.

[25] M. Mohan and T. A. Siddiqui, "Analysis of various schemes for the estimation of atmospheric stability classification," *Atmospheric Environment*, vol. 32, no. 21, pp. 3775–3781, 1998.

[26] G.I.Taylor, "The spectrum of turbulence," in *Proceedings of the Royal Society of London*, vol. 164 of *Series A*, pp. 476–490, Mathematical and Physical sciences, 1938.

[27] C. W. Higgins, M. Froidevaux, V. Simeonov, N. Vercauteren, C. Barry, and M. B. Parlange, "The Effect of Scale on the Applicability of Taylor's Frozen Turbulence Hypothesis in the Atmospheric Boundary Layer," *Boundary-Layer Meteorology*, vol. 143, no. 2, pp. 379–391, 2012.

[28] Y. Cheng, C. Sayde, Q. Li, J. Basara, J. Selker, E. Tanner, and P. Gentine, "Failure of Taylor's hypothesis in the atmospheric surface layer and its correction for eddy-covariance measurements," *Geophysical Research Letters*, vol. 44, no. 9, pp. 4287–4295, 2017.

[29] S. Shi, Z. Liu, X. Deng, S. Chen, and D. Song, "From Lidar Measurement to Rotor Effective Wind Speed Prediction: Empirical Mode Decomposition and Gated Recurrent Unit Solution," *Sensors*, vol. 23, no. 23, 2023.

[30] R. A. Pielke and H. A. Panofsky, "Turbulence characteristics along several towers," *Boundary-Layer Meteorology*, vol. 1, no. 2, pp. 115–130, 1970.

[31] H. A. Panofsky and T. Mizuno, "Horizontal coherence and Pasquill's beta," *Boundary-Layer Meteorology*, vol. 9, no. 3, pp. 247–256, 1975.

[32] T. Mizuno and H. Panofsky, "The validity of Taylor's hypothesis in the atmospheric surface layer," *Boundary-Layer Meteorology*, vol. 9, pp. 375–380, 1975.

[33] T. Wetz, J. Zink, J. Bange, and N. Wildmann, "Analyses of Spatial Correlation and Coherence in ABL Flow with a Fleet of UAS," *Boundary-Layer Meteorology*, vol. 187, pp. 673–701, jun 2023.

[34] K. Selvam, S. Kanev, J. van Wingerden, T. van Engelsen, and M. Verhaegen, "Feedback–feedforward individual pitch control for wind turbine load reduction," *International Journal of Robust and Nonlinear Control*, vol. 19, no. 2009, pp. 72–91, 2009.

[35] C.-H. Moeng, "A large-eddy-simulation model for the study of planetary boundary-layer turbulence," *Journal of Atmospheric Sciences*, vol. 41, no. 13, pp. 2052 – 2062, 1984.

[36] P. McMurtry, *Lecture notes in ME 7960 - Turbulence: 6. Vorticity Dynamics*. University of Utah, 2000.

[37] S. Lovejoy and D. Schertzer, *The weather and climate: Emergent laws and multifractal cascades*. 2011.

[38] R. B. Bird, R. C. Armstrong, and O. Hassager, *Dynamics of Polymeric Liquids*, vol. 1. John Wiley & Sons, Inc., 1987.

[39] P.J. Mason, "Large-eddy simulation: A critical review of the technique," *Royal Meteorological Society, Quarterly Journal*, vol. 120, no. 515, pp. 1–26, 1994.

[40] A. Leonard, "Energy cascade in large eddy simulations of turbulent fluid flow," *Adv. Geophys.*, vol. 18A, pp. 237–248, 01 1974.

Appendices

A Derivation of equations

This section will derive the governing equations for both LES and the wind model used, starting with the set of conservation equations of mass, momentum and energy (in differential form).

A.1 Navier-Stokes equations for a general fluid

The general Navier-Stokes equations in three dimensions describe the behavior of a fluid based on a number of conservation laws. These equations can be rewritten to certain forms in order to provide additional insights. This section will show a number of useful variants of the Navier-Stokes equations.

Conservation equations

Mass:
$$\frac{\partial \rho}{\partial t} + \frac{\partial}{\partial x_j}(\rho u_j) = 0 \tag{A.1}$$

Momentum:
$$\frac{\partial}{\partial t}(\rho u_i) + \frac{\partial}{\partial x_j}(\rho u_i u_j) = \frac{\partial \sigma_{ji}}{\partial x_j} + F_i \qquad \text{for } i = 1, 2, 3 \tag{A.2}$$

(Total) Energy:
$$\frac{\partial E}{\partial t} + \frac{\partial}{\partial x_j}(E u_j) = -\frac{\partial q_j}{\partial x_j} + \frac{\partial}{\partial x_j}(\sigma_{ji} u_i) + u_i F_i + Q \tag{A.3}$$

A.1.1 Momentum equation

Focusing on the momentum equation, the partial derivatives on the left-hand side are expanded using the chain rule (which alters the form of the equation from conservative to non-conservative):

$$\frac{\partial}{\partial t}(\rho u_i) = \rho \frac{\partial u_i}{\partial t} + u_i \frac{\partial \rho}{\partial t} \tag{A.4}$$

$$\frac{\partial}{\partial x_j}(\rho u_i u_j) = u_i \frac{\partial}{\partial x_j}(\rho u_j) + \rho u_j \frac{\partial u_i}{\partial x_j} \tag{A.5}$$

Resulting in:

$$\rho \frac{\partial u_i}{\partial t} + \rho u_j \frac{\partial u_i}{\partial x_j} + u_i \left(\frac{\partial \rho}{\partial t} + \frac{\partial}{\partial x_j}(\rho u_j) \right) = \frac{\partial \sigma_{ji}}{\partial x_j} + F_i \qquad \text{for } i = 1, 2, 3 \tag{A.6}$$

The conservation of mass (Equation A.1) can be recognized and, as it is zero, eliminated from the momentum equation:

$$\rho \frac{\partial u_i}{\partial t} + \rho u_j \frac{\partial u_i}{\partial x_j} = \frac{\partial \sigma_{ji}}{\partial x_j} + F_i \qquad \text{for } i = 1, 2, 3 \tag{A.7}$$

The surface stresses can be split into normal stresses due to the pressure (p) and shear stresses (τ):

$$\sigma_{ij} = -p\delta_{ij} + \tau_{ij} \tag{A.8}$$

where δ_{ij} is the Kronecker delta. This leads to the rewritten momentum equation in Eulerian form:

$$\rho \frac{\partial u_i}{\partial t} + \rho u_j \frac{\partial u_i}{\partial x_j} = -\frac{\partial p}{\partial x_i} + \frac{\partial \tau_{ij}}{\partial x_j} + F_i \qquad \text{for } i = 1, 2, 3 \tag{A.9}$$

Where the left-hand side shows the conserved advection of momentum and the right-hand side shows the momentum forcing terms: pressure, shear stress and body forces, respectively.

The left-hand side can be rewritten to the Lagrangian form using the material derivative:

$$\frac{\mathrm{D}u_i}{\mathrm{D}t} = \frac{\partial u_i}{\partial t} + u_j \frac{\partial u_i}{\partial x_j} \tag{A.10}$$

Which describes the change of velocity of a fluid parcel traveling along its pathline. The momentum equation then becomes:

$$\rho \frac{\mathrm{D}u_i}{\mathrm{D}t} = -\frac{\partial p}{\partial x_i} + \frac{\partial \tau_{ij}}{\partial x_j} + F_i \qquad \text{for } i = 1, 2, 3 \tag{A.11}$$

A.1.2 Momentum equation (rotation form)

The nonlinear advection terms in the momentum equation are sometimes written in rotation form in order to conserve the volume-averaged kinetic energy when solving numerically.[35] The nonlinear advection term can be written as the sum of the cross product of vorticity and velocity with the gradient of specific kinetic energy.

The vorticity, being the curl of the velocity, is defined as:

$$\underset{\sim}{\omega} = \nabla \times \underset{\sim}{u} = \begin{Bmatrix} \dfrac{\partial w}{\partial y} - \dfrac{\partial v}{\partial z} \\ \dfrac{\partial u}{\partial z} - \dfrac{\partial w}{\partial x} \\ \dfrac{\partial v}{\partial x} - \dfrac{\partial u}{\partial y} \end{Bmatrix} \tag{A.12}$$

Taking the cross product of the vorticity with velocity:

$$\underset{\sim}{\omega} \times \underset{\sim}{u} = (\nabla \times \underset{\sim}{u}) \times \underset{\sim}{u} = \begin{Bmatrix} v\dfrac{\partial u}{\partial y} + w\dfrac{\partial u}{\partial z} - v\dfrac{\partial v}{\partial x} - w\dfrac{\partial w}{\partial x} \\ u\dfrac{\partial v}{\partial x} + w\dfrac{\partial v}{\partial z} - u\dfrac{\partial u}{\partial y} - w\dfrac{\partial w}{\partial y} \\ u\dfrac{\partial w}{\partial x} + v\dfrac{\partial w}{\partial y} - u\dfrac{\partial u}{\partial z} - v\dfrac{\partial v}{\partial z} \end{Bmatrix} \tag{A.13}$$

This is also known as the (negative of the) Lamb vector.

The gradient of specific kinetic energy is:

$$\nabla e_k = \nabla \left(\frac{1}{2} |\underset{\sim}{u}|^2 \right) = \frac{\partial}{\partial x_i} \left(\frac{1}{2} u_k u_k \right) = u_j \frac{\partial u_j}{\partial x_i} = \begin{Bmatrix} u\dfrac{\partial u}{\partial x} + v\dfrac{\partial v}{\partial x} + w\dfrac{\partial w}{\partial x} \\ u\dfrac{\partial u}{\partial y} + v\dfrac{\partial v}{\partial y} + w\dfrac{\partial w}{\partial y} \\ u\dfrac{\partial u}{\partial z} + v\dfrac{\partial v}{\partial z} + w\dfrac{\partial w}{\partial z} \end{Bmatrix} \tag{A.14}$$

Summing Equations A.13 and A.14 indeed leads to the nonlinear advection term:

$$\underset{\sim}{\omega} \times \underset{\sim}{u} + \nabla \left(\frac{1}{2} |\underset{\sim}{u}|^2 \right) = (\nabla \cdot \underset{\sim}{u}) \underset{\sim}{u} \tag{A.15}$$

Which becomes very clear when writing Equation A.13 in index notation:

$$\underset{\sim}{\omega} \times \underset{\sim}{u} = u_j \frac{\partial u_i}{\partial x_j} - u_j \frac{\partial u_j}{\partial x_i} \tag{A.16}$$

Therefore:

$$u_j \frac{\partial u_i}{\partial x_j} - u_j \frac{\partial u_j}{\partial x_i} + \frac{\partial}{\partial x_i}\left(\frac{1}{2} u_k u_k\right) = u_j \frac{\partial u_i}{\partial x_j} - u_j \frac{\partial u_j}{\partial x_i} + u_j \frac{\partial u_j}{\partial x_i} = u_j \frac{\partial u_i}{\partial x_j} \tag{A.17}$$

Substituting this result into the momentum equation (Equation A.9) and moving the gradient of the specific kinetic energy to the right-hand side results in the Lamb-Gromeka equation:

$$\frac{\partial u_i}{\partial t} + u_j \frac{\partial u_i}{\partial x_j} - u_j \frac{\partial u_j}{\partial x_i} = -\frac{1}{\rho}\frac{\partial p}{\partial x_i} - \frac{\partial}{\partial x_i}\left(\frac{1}{2} u_k u_k\right) + \frac{1}{\rho}\frac{\partial \tau_{ij}}{\partial x_j} + \frac{1}{\rho} F_i \qquad \text{for } i = 1, 2, 3 \tag{A.18}$$

The pressure term can be expanded using the chain rule:

$$\frac{1}{\rho}\frac{\partial p}{\partial x_i} = \frac{\partial}{\partial x_i}\left(\frac{p}{\rho}\right) - \frac{p}{\rho^2}\frac{\partial \rho}{\partial x_i} \tag{A.19}$$

The pressure and kinetic energy terms can then be combined, which leads to the momentum equation in rotation form:

$$\frac{\partial u_i}{\partial t} + u_j \left(\frac{\partial u_i}{\partial x_j} - \frac{\partial u_j}{\partial x_i}\right) = -\frac{\partial P}{\partial x_i} + \frac{p}{\rho^2}\frac{\partial \rho}{\partial x_i} + \frac{1}{\rho}\frac{\partial \tau_{ij}}{\partial x_j} + \frac{1}{\rho} F_i \qquad \text{for } i = 1, 2, 3 \tag{A.20}$$

Where P is the total kinematic pressure, defined as:

$$P = \frac{p}{\rho} + \frac{1}{2} u_k u_k \tag{A.21}$$

The usefulness of this form is mostly reserved to incompressible cases where the $\partial\rho/\partial x_i$-term vanishes as it indicates a forcing due to a density gradient/compressibility effect.

A.1.3 Vorticity equation

The momentum equation can be rewritten to the vorticity equation, governing the conservation of angular momentum, by considering that vorticity is the curl of velocity, as shown in Equation A.12. Taking the curl of the momentum equation (Equation A.9 in vector notation):

$$\nabla \times \frac{\partial \underset{\sim}{u}}{\partial t} + \nabla \times (\underset{\sim}{u} \cdot \nabla)\underset{\sim}{u} = \nabla \times \left(-\frac{1}{\rho}\nabla p\right) + \nabla \times \left(\frac{\nabla \cdot \underline{\tau}}{\rho}\right) + \nabla \times \left(\frac{\underline{\underline{F}}}{\rho}\right) \tag{A.22}$$

Substituting Equation A.15, as the dot product is commutative, results in:

$$\frac{\partial \underset{\sim}{\omega}}{\partial t} + \nabla \times (\underset{\sim}{\omega} \times \underset{\sim}{u}) + \nabla \times \nabla\left(\frac{1}{2}|\underset{\sim}{u}|^2\right) = \nabla \times \left(-\frac{1}{\rho}\nabla p\right) + \nabla \times \left(\frac{\nabla \cdot \underline{\tau}}{\rho}\right) + \nabla \times \left(\frac{\underline{\underline{F}}}{\rho}\right) \tag{A.23}$$

The specific kinetic energy term vanishes as the curl of the gradient of a scalar is zero. Expanding the second term in the equation:

$$\nabla \times (\underset{\sim}{\omega} \times \underset{\sim}{u}) = \underset{\sim}{\omega}(\nabla \cdot \underset{\sim}{u}) - \underset{\sim}{u}(\nabla \cdot \underset{\sim}{\omega}) + (\underset{\sim}{u} \cdot \nabla)\underset{\sim}{\omega} - (\underset{\sim}{\omega} \cdot \nabla)\underset{\sim}{u} \tag{A.24}$$

Where the second term on the right-hand side vanishes as the divergence of curl is zero. The third term can be recognized to be part of the vorticity transportation.

Focusing on the density-pressure term and using the product rule:

$$\nabla \times \left(-\frac{1}{\rho}\nabla p\right) = \nabla\left(-\rho^{-1}\right) \times \nabla p - \rho^{-1}\nabla \times \nabla p \tag{A.25}$$

Recognizing that the second term is zero as it is the curl of a gradient. The term $\nabla\left(-\rho^{-1}\right)$ can also be expanded using the chain rule (shown in tensor notation for clarity):

$$\frac{\partial}{\partial x}\left(-\rho^{-1}\right) = \frac{\partial}{\partial \rho}\left(-\rho^{-1}\right)\frac{\partial \rho}{\partial x} = \rho^{-2}\frac{\partial \rho}{\partial x} \tag{A.26}$$

Substituting leads to the vorticity equation:

$$\boxed{\frac{\partial \underset{\sim}{\omega}}{\partial t} + (\underset{\sim}{u}\cdot\nabla)\underset{\sim}{\omega} = (\underset{\sim}{\omega}\cdot\nabla)\underset{\sim}{u} - \underset{\sim}{\omega}(\nabla\cdot\underset{\sim}{u}) + \frac{1}{\rho^2}\nabla\rho\times\nabla p + \nabla\times\left(\frac{\nabla\cdot\underset{\sim}{\tau}}{\rho}\right) + \nabla\times\left(\frac{\underset{\sim}{F}}{\rho}\right)} \tag{A.27}$$

The first term on the right-hand side represents vortex stretching. It is a vital aspect of turbulent energy cascading from the larger eddies towards the smaller eddies. The second term is a compressibility term; the magnitude of vorticity is reduced in an expanding flow due to the conservation of angular momentum. The density-pressure term is baroclinic torque and the shear stress term represents diffusion of vorticity due to viscous effects.[36]

The vortex stretching term, $(\underset{\sim}{\omega}\cdot\nabla)\underset{\sim}{u}$, can be expanded by decomposing the velocity gradient tensor into its symmetric and skew-symmetric parts:

$$\omega_j\frac{\partial u_i}{\partial x_j} = \omega_j S_{ij} + \omega_j R_{ij} \tag{A.28}$$

The symmetric part is the strain-rate tensor S_{ij} and the skew-symmetric part represents rigid-body rotation, R_{ij}. Note however that the rotation tensor and vorticity are related through the Levi-Civita symbol:

$$R_{ij} = \varepsilon_{ijk}\omega_k \quad \rightarrow \quad \omega_j R_{ij} = \omega_j\varepsilon_{ijk}\omega_k = 0 \tag{A.29}$$

The rotation tensor vanishes and only the strain-rate tensor remains, therefore showing that positive strain increases the magnitude of the vorticity.

Considering a vortex tube where the surface is aligned with the vorticity vector, the ends of this tube will, due to the chaotic nature of turbulence, tend to grow further apart with time. This stretching motion will increase the vorticity. Simultaneously the stretching of the tube will, due to conservation of mass, cause a combination of cross-sectional shrinking of the tube and a reduction in density (in case of a compressible flow). The shrinking constitutes a length scale reduction, eventually pinching the vortex tube and breaking it up to smaller scales. This largely conserves the kinetic energy (except at very small scales where the viscous terms are large) and shows the process of kinetic energy transfer from the larger scales to the smaller scales.[37]

A.1.4 Kinetic energy equation

Taking the dot product of the velocity and the conservation of momentum equation (Equation A.2) will result in the kinetic energy equation:

$$u_i\frac{\partial}{\partial t}(\rho u_i) + u_i\frac{\partial}{\partial x_j}(\rho u_i u_j) = u_i\frac{\partial \sigma_{ji}}{\partial x_j} + u_i F_i \tag{A.30}$$

All partial derivatives are expanded using the chain rule:

$$u_i\frac{\partial}{\partial t}(\rho u_i) = \frac{\partial}{\partial t}\left(\frac{1}{2}\rho u_i u_i\right) - \frac{1}{2}u_i u_i\frac{\partial \rho}{\partial t} \tag{A.31}$$

$$u_i \frac{\partial}{\partial x_j}(\rho u_i u_j) = \frac{\partial}{\partial x_j}\left(\frac{1}{2}\rho u_i u_i u_j\right) - \frac{1}{2}u_i u_i \frac{\partial}{\partial x_j}(\rho u_j) \tag{A.32}$$

$$u_i \frac{\partial \sigma_{ji}}{\partial x_j} = \frac{\partial}{\partial x_j}(\sigma_{ji} u_i) - \sigma_{ji}\frac{\partial u_i}{\partial x_j} \tag{A.33}$$

Substituting and grouping the terms:

$$\frac{\partial}{\partial t}\left(\frac{1}{2}\rho u_i u_i\right) + \frac{\partial}{\partial x_j}\left(\frac{1}{2}\rho u_i u_i u_j\right) - \frac{1}{2}u_i u_i \left(\frac{\partial \rho}{\partial t} + \frac{\partial}{\partial x_j}(\rho u_j)\right) = \frac{\partial}{\partial x_j}(\sigma_{ji} u_i) - \sigma_{ji}\frac{\partial u_i}{\partial x_j} + u_i F_i \tag{A.34}$$

Recognizing the conservation of mass and substituting it again, results in the kinetic energy equation:

$$\frac{\partial}{\partial t}\left(\frac{1}{2}\rho u_i u_i\right) + \frac{\partial}{\partial x_j}\left(\frac{1}{2}\rho u_i u_i u_j\right) = \frac{\partial}{\partial x_j}(\sigma_{ji} u_i) - \sigma_{ji}\frac{\partial u_i}{\partial x_j} + u_i F_i \tag{A.35}$$

The left-hand side contains the rate of change and flux of kinetic energy. The right-hand side contains the rate of work done on the fluid by the stresses, the rate of kinetic energy loss due to molecular interactions through viscous dissipation and pressure effects, and, finally, the rate of work done by the body forces.

A.1.5 Internal energy equation

Total energy can be split into the internal energy and the kinetic energy, using:

$$E = \rho e + \frac{1}{2}\rho u_i u_i \tag{A.36}$$

Expanding the conservation of total energy equation (Equation A.3) and splitting the left-hand side:

$$\frac{\partial}{\partial t}(\rho e) + \frac{\partial}{\partial x_j}(\rho e u_j) + \frac{\partial}{\partial t}\left(\frac{1}{2}\rho u_i u_i\right) + \frac{\partial}{\partial x_j}\left(\frac{1}{2}\rho u_i u_i u_j\right) = -\frac{\partial q_j}{\partial x_j} + \frac{\partial}{\partial x_j}(\sigma_{ji} u_i) + u_i F_i + Q \tag{A.37}$$

Subtracting the kinetic energy equation (Equation A.35) results in the internal energy equation:

$$\frac{\partial}{\partial t}(\rho e) + \frac{\partial}{\partial x_j}(\rho e u_j) = -\frac{\partial q_j}{\partial x_j} + \sigma_{ji}\frac{\partial u_i}{\partial x_j} + Q \tag{A.38}$$

Splitting the partial derivatives of the left-hand side using the chain rule and separating the normal and shear stresses (using Equation A.8):

$$\rho\frac{\partial e}{\partial t} + \rho u_j \frac{\partial e}{\partial x_j} + e\left(\frac{\partial \rho}{\partial t} + \frac{\partial}{\partial x_j}(\rho u_j)\right) = -\frac{\partial q_j}{\partial x_j} - p\frac{\partial u_i}{\partial x_i} + \tau_{ij}\frac{\partial u_i}{\partial x_j} + Q \tag{A.39}$$

Substituting the conservation of mass again, results in the internal energy equation:

$$\rho\frac{\partial e}{\partial t} + \rho u_j \frac{\partial e}{\partial x_j} = -\frac{\partial q_j}{\partial x_j} - p\frac{\partial u_i}{\partial x_i} + \tau_{ij}\frac{\partial u_i}{\partial x_j} + Q \tag{A.40}$$

The left-hand side contains the rate of change and flux of internal energy. The right-hand side contains the heat flux, the rate of internal energy change due to molecular interactions through pressure effects and viscous dissipation, and, finally, volumetric heating.

In Lagrangian form the internal energy equation becomes:

$$\rho\frac{\mathrm{D}e}{\mathrm{D}t} = -\frac{\partial q_j}{\partial x_j} - p\frac{\partial u_i}{\partial x_i} + \tau_{ij}\frac{\partial u_i}{\partial x_j} + Q \tag{A.41}$$

A.1.6 Enthalpy equation

Specific enthalpy is defined as the sum of internal energy and work done to displace the surroundings to accommodate the occupied volume against an external pressure:

$$h = e + \frac{p}{\rho} \tag{A.42}$$

Substituting into the internal energy equation (Equation A.40) and splitting the left-hand side:

$$\rho\frac{\partial h}{\partial t} + \rho u_j\frac{\partial h}{\partial x_j} - \rho\frac{\partial}{\partial t}\left(\frac{p}{\rho}\right) - \rho u_j\frac{\partial}{\partial x_j}\left(\frac{p}{\rho}\right) = -\frac{\partial q_j}{\partial x_j} - p\frac{\partial u_i}{\partial x_i} + \tau_{ij}\frac{\partial u_i}{\partial x_j} + Q \tag{A.43}$$

Applying the chain rule to the partial derivatives containing p/ρ:

$$-\rho\frac{\partial}{\partial t}\left(\frac{p}{\rho}\right) = -\frac{\partial p}{\partial t} + \frac{p}{\rho}\frac{\partial \rho}{\partial t} \tag{A.44}$$

$$-\rho u_j\frac{\partial}{\partial x_j}\left(\frac{p}{\rho}\right) = -u_j\frac{\partial p}{\partial x_j} + \frac{p}{\rho}u_j\frac{\partial \rho}{\partial x_j} = -u_j\frac{\partial p}{\partial x_j} + \frac{p}{\rho}\frac{\partial}{\partial x_j}\left(\rho u_j\right) - p\frac{\partial u_j}{\partial x_j} \tag{A.45}$$

Resulting in:

$$\rho\frac{\partial h}{\partial t} + \rho u_j\frac{\partial h}{\partial x_j} - \frac{\partial p}{\partial t} - u_j\frac{\partial p}{\partial x_j} + \frac{p}{\rho}\left(\frac{\partial \rho}{\partial t} + \frac{\partial}{\partial x_j}\left(\rho u_j\right)\right) - p\frac{\partial u_j}{\partial x_j} = -\frac{\partial q_j}{\partial x_j} - p\frac{\partial u_i}{\partial x_i} + \tau_{ij}\frac{\partial u_i}{\partial x_j} + Q \tag{A.46}$$

Substituting the conservation of mass again and reordering results in the enthalpy equation:

$$\rho\frac{\partial h}{\partial t} + \rho u_j\frac{\partial h}{\partial x_j} = -\frac{\partial q_j}{\partial x_j} + \frac{\partial p}{\partial t} + u_j\frac{\partial p}{\partial x_j} + \tau_{ij}\frac{\partial u_i}{\partial x_j} + Q \tag{A.47}$$

In Lagrangian form the enthalpy equation becomes:

$$\rho\frac{\mathrm{D}h}{\mathrm{D}t} = -\frac{\partial q_j}{\partial x_j} + \frac{\mathrm{D}p}{\mathrm{D}t} + \tau_{ij}\frac{\partial u_i}{\partial x_j} + Q \tag{A.48}$$

A.1.7 Temperature equation

Up until this point no assumptions have been made. However, in order to derive the temperature equation enthalpy is assumed to only be a function of the state variables p and T (disregarding the strain state of a system or any other state contribution)[38]:

$$h = e + \frac{p}{\rho} = f(p, T) \tag{A.49}$$

Such that the following thermodynamic relation can be used:

$$\mathrm{d}h = \left(\frac{\partial h}{\partial T}\right)_p \mathrm{d}T + \left(\frac{\partial h}{\partial p}\right)_T \mathrm{d}p = c_p \mathrm{d}T + \frac{1}{\rho}\left(1 - \beta T\right)\mathrm{d}p, \qquad \text{with } \beta = \rho\left(\frac{\partial}{\partial T}\left(\frac{1}{\rho}\right)\right)_p \tag{A.50}$$

Where β is the thermal expansion coefficient. This equation, like the first law of thermodynamics on which it is based, applies to a thermodynamic system in equilibrium. Any volume or fluid particle in a flow is considered a small thermodynamic system in equilibrium as any change in equilibrium is resolved much faster than a change in flow. Therefore the equation can be rewritten to apply to a fluid particle:

$$\frac{\mathrm{D}h}{\mathrm{D}t} = c_p\frac{\mathrm{D}T}{\mathrm{D}t} + \frac{1}{\rho}\left(1 - \beta T\right)\frac{\mathrm{D}p}{\mathrm{D}t} \tag{A.51}$$

Which can be substituted into the Lagrangian form of the enthalpy equation (Equation A.48) to obtain the temperature equation in Lagrangian form:

$$\rho c_p \frac{\mathrm{D}T}{\mathrm{D}t} = -\frac{\partial q_j}{\partial x_j} + \tau_{ij}\frac{\partial u_i}{\partial x_j} + Q + \beta T \frac{\mathrm{D}p}{\mathrm{D}t} \tag{A.52}$$

And the temperature equation in Eulerian form:

$$\rho c_p \left(\frac{\partial T}{\partial t} + u_j \frac{\partial T}{\partial x_j}\right) = -\frac{\partial q_j}{\partial x_j} + \tau_{ij}\frac{\partial u_i}{\partial x_j} + Q + \beta T \left(\frac{\partial p}{\partial t} + u_j \frac{\partial p}{\partial x_j}\right), \qquad \text{assuming } h = f(p,T) \tag{A.53}$$

Where the last term indicates work done by the pressure where the temperature changes due to a change in density.

A.1.8 Potential temperature equation

The concept of potential temperature is often used in atmospheric problems as it is a better characterization than temperature. Temperature is namely influenced by changes in pressure altitude and potential temperature eliminates this variation. Potential temperature is derived from the first law of thermodynamics and assumes an ideal gas, which is a valid assumption for air in the temperature range of interest[13]:

$$\mathrm{d}q = \mathrm{d}e + p\mathrm{d}\mathcal{V} \tag{A.54}$$

where $\mathcal{V} = \rho^{-1}$ is the specific volume. The internal energy for an ideal gas is:

$$\mathrm{d}e = c_v \mathrm{d}T \tag{A.55}$$

The equation of state for an ideal gas can be written for small increments as:

$$p\mathrm{d}\mathcal{V} + \mathcal{V}\mathrm{d}p = R\mathrm{d}T \tag{A.56}$$

The first law of thermodynamics is then rewritten for an ideal gas to:

$$\mathrm{d}q = c_v \mathrm{d}T + R\mathrm{d}T - \mathcal{V}\mathrm{d}p \tag{A.57}$$

For an ideal gas the heat capacity and gas constant are related through:

$$c_p = c_v + R \tag{A.58}$$

Resulting in:

$$\mathrm{d}q = c_p \mathrm{d}T - \mathcal{V}\mathrm{d}p \tag{A.59}$$

Potential temperature is defined as the temperature of a parcel when it is adiabatically ($\mathrm{d}q = 0$) brought to a reference pressure. Therefore:

$$c_p \mathrm{d}T - \mathcal{V}\mathrm{d}p = 0 \tag{A.60}$$

Substituting the equation of state for the specific volume and reordering leads to:

$$\frac{1}{T}\mathrm{d}T - \frac{R}{c_p}\frac{1}{p}\mathrm{d}p = 0 \tag{A.61}$$

Integrating from state T, p to the potential temperature and reference pressure (θ, p_0):

$$\int_T^\theta \frac{1}{T}\mathrm{d}T - \int_p^{p_0} \frac{R}{c_p}\frac{1}{p}\mathrm{d}p = 0 \tag{A.62}$$

$$\ln(T) - \ln(\theta) - \frac{R}{c_p}\ln(p) + \frac{R}{c_p}\ln(p_0) = 0 \tag{A.63}$$

$$\ln(\theta) = \ln\left(T\left(\frac{p_0}{p}\right)^{R/c_p}\right) \tag{A.64}$$

Leading to the definition of potential temperature:

$$\theta = T\left(\frac{p_0}{p}\right)^{R/c_p} \tag{A.65}$$

Substituting the potential temperature into the temperature equation (Equation A.52):

$$\rho c_p \frac{\mathrm{D}}{\mathrm{D}t}\left[\theta\left(\frac{p}{p_0}\right)^{R/c_p}\right] = -\frac{\partial q_j}{\partial x_j} + \tau_{ij}\frac{\partial u_i}{\partial x_j} + q + \beta\theta\left(\frac{p}{p_0}\right)^{R/c_p}\frac{\mathrm{D}p}{\mathrm{D}t} \tag{A.66}$$

Expanding the material derivatives:

$$\rho c_p\left(\frac{p}{p_0}\right)^{R/c_p}\frac{\mathrm{D}\theta}{\mathrm{D}t} + \frac{\rho R\theta}{p}\left(\frac{p}{p_0}\right)^{R/c_p}\frac{\mathrm{D}p}{\mathrm{D}t} = -\frac{\partial q_j}{\partial x_j} + \tau_{ij}\frac{\partial u_i}{\partial x_j} + q + \beta\theta\left(\frac{p}{p_0}\right)^{R/c_p}\frac{\mathrm{D}p}{\mathrm{D}t} \tag{A.67}$$

$$\rho c_p\left(\frac{p}{p_0}\right)^{R/c_p}\frac{\mathrm{D}\theta}{\mathrm{D}t} = -\frac{\partial q_j}{\partial x_j} + \tau_{ij}\frac{\partial u_i}{\partial x_j} + q + \left(\beta - \frac{\rho R}{p}\right)\theta\left(\frac{p}{p_0}\right)^{R/c_p}\frac{\mathrm{D}p}{\mathrm{D}t} \tag{A.68}$$

The thermal expansion coefficient for an ideal gas is:

$$\beta = \rho\left(\frac{\partial}{\partial T}\left(\frac{1}{\rho}\right)\right)_p = \rho\left(\frac{\partial}{\partial T}\left(\frac{RT}{p}\right)\right)_p = \frac{\rho R}{p} \tag{A.69}$$

The pressure derivative is then indeed eliminated as expected from the concept of potential temperature:

$$\rho c_p\left(\frac{p}{p_0}\right)^{R/c_p}\frac{\mathrm{D}\theta}{\mathrm{D}t} = -\frac{\partial q_j}{\partial x_j} + \tau_{ij}\frac{\partial u_i}{\partial x_j} + Q \tag{A.70}$$

$$\frac{\mathrm{D}\theta}{\mathrm{D}t} = \frac{1}{\rho c_p}\left(\frac{p_0}{p}\right)^{R/c_p}\left(-\frac{\partial q_j}{\partial x_j} + \tau_{ij}\frac{\partial u_i}{\partial x_j} + Q\right)\Big|_{T,p} \tag{A.71}$$

Note that any heat addition terms that are defined at pressure p are adiabatically converted to p_0. Heating effects can also be defined in terms of θ and p_0 directly.

A.2 Atmospheric boundary layer equations

With the general system of equations defined in the previous section, assumptions can be applied to obtain the equations specific to the atmospheric boundary layer (ABL).

As the typical wind velocities are much lower than 0.3M, the flow will be assumed incompressible, i.e. constant ρ. The density can therefore be moved outside the partial derivatives as it does not change over time or space. This simplifies the conservation of mass (Equation A.1) to:

$$\frac{\partial u_j}{\partial x_j} = 0 \tag{A.72}$$

This indicates that the flow is now divergence-free.

Assuming the medium is Newtonian and iso-tropic, Stokes' hypothesis can be applied as a constitutive equation. The shear stress is then rewritten in terms of the dynamic viscosity μ. These assumptions are valid for air[13] and result in:

$$\tau_{ij} = \mu \left(\frac{\partial u_i}{\partial x_j} + \frac{\partial u_j}{\partial x_i} \right) - \frac{2}{3} \mu \delta_{ij} \frac{\partial u_k}{\partial x_k} \qquad \text{for } i = 1, 2, 3 \tag{A.73}$$

where the last term is a compressibility term, which vanishes when substituting the incompressible continuity equation:

$$\tau_{ij} = \mu \left(\frac{\partial u_i}{\partial x_j} + \frac{\partial u_j}{\partial x_i} \right) \qquad \text{for } i = 1, 2, 3 \tag{A.74}$$

Applied to the momentum equation (Equation A.9) it becomes:

$$\frac{\partial u_i}{\partial t} + u_j \frac{\partial u_i}{\partial x_j} = -\frac{1}{\rho_0} \frac{\partial p}{\partial x_i} + \frac{\partial}{\partial x_j} \left(\nu \left(\frac{\partial u_i}{\partial x_j} + \frac{\partial u_j}{\partial x_i} \right) \right) + \frac{1}{\rho_0} F_i \qquad \text{for } i = 1, 2, 3 \tag{A.75}$$

Where the dynamic viscosity is replaced by the kinematic viscosity:

$$\nu = \frac{\mu}{\rho} \tag{A.76}$$

The body forces, F_i, of importance are gravity, buoyancy due to atmospheric stability and the Coriolis force due to planetary rotation. The buoyancy force is caused by a difference in density along the vertical axis/altitude. This clashes with the already assumed incompressibility. Therefore, the Boussinesq approximation is used, where density fluctuations are only retained if they are multiplied by a gravity term.[13] This is sometimes called pseudo-incompressibility. The combined gravity and buoyancy forces are:

$$\underset{\sim}{F}_{grav,buoy} = \rho g_i = \rho_0 g_i - \rho_0 g_i \left(\frac{\theta - \theta_0}{\theta_0} \right) \tag{A.77}$$

where the potential temperature is used and the bracketed term indicates the relative fluctuation compared to a reference potential temperature. Note that the definition of potential temperature assumes an ideal gas for the equation of state.

The Coriolis force depends on the location and heading of the wind turbine, as the force depends on the latitude ϕ and azimuth a:

$$\underset{\sim}{F}_{Cor} = \rho_0 a_{Cor} = -2\rho_0 \, \underset{\sim}{\Omega} \times \underset{\sim}{V} \tag{A.78}$$

where $\underset{\sim}{\Omega}$ relates to the planetary rotation and $\underset{\sim}{V}$ relates to the velocities in the planetary reference frame:

$$\underset{\sim}{\Omega} = \omega \begin{Bmatrix} 0 \\ \cos(\phi) \\ \sin(\phi) \end{Bmatrix}, \qquad \underset{\sim}{V} = \begin{Bmatrix} V_{\text{east}} \\ V_{\text{north}} \\ V_{\text{vertical}} \end{Bmatrix} \tag{A.79}$$

The Coriolis force must now be converted to the reference frame used (u, v, w) using the azimuth angle:

$$\underset{\sim}{V} = \begin{Bmatrix} V_{\text{east}} \\ V_{\text{north}} \\ V_{\text{vertical}} \end{Bmatrix} = \begin{Bmatrix} u \sin(a) + v \cos(a) \\ u \cos(a) + v \sin(a) \\ w \end{Bmatrix} \tag{A.80}$$

The Coriolis force becomes:

$$\underset{\sim}{F}_{Cor} = 2\rho_0 \omega \begin{Bmatrix} [u \cos(a) + v \sin(a)] \sin(\phi) - w \cos(\phi) \\ -[u \sin(a) + v \cos(a)] \sin(\phi) \\ [u \sin(a) + v \cos(a)] \cos(\phi) \end{Bmatrix} \tag{A.81}$$

These are the general forces acting on the fluid in the atmospheric boundary layer. Additional forces like turbine induction or a driving mean pressure gradient in the form of geostrophic winds can be introduced on a case-by-case basis.

The conservation of energy in the form of the potential temperature equation is left unaltered. For an incompressible flow it is decoupled from the continuity and momentum equations if viscous effects can be neglected or the viscosity is not a function of temperature.

All assumptions until now are shared by both ABL LES and the wind model. The atmospheric boundary layer equations from which they both start are:

Atmospheric boundary layer equations

Continuity:
$$\frac{\partial u_j}{\partial x_j} = 0 \tag{A.82}$$

Momentum:
$$\frac{\partial u_i}{\partial t} + u_j \frac{\partial u_i}{\partial x_j} = -\frac{1}{\rho_0}\frac{\partial p^*}{\partial x_i} + \frac{\partial}{\partial x_j}\left(\nu\left(\frac{\partial u_i}{\partial x_j} + \frac{\partial u_j}{\partial x_i}\right)\right) + \delta_{i3} g \left(\frac{\theta - \theta_0}{\theta_0}\right) + f_{Cor,i} + f_i \qquad \text{for } i = 1,2,3 \tag{A.83}$$

Potential temperature:
$$\frac{\mathrm{D}\theta}{\mathrm{D}t} = \frac{1}{\rho_0 c_p}\left(\frac{p_0}{p}\right)^{R/c_p}\left(-\frac{\partial q_j}{\partial x_j} + \tau_{ij}\frac{\partial u_i}{\partial x_j} + Q\right) \tag{A.84}$$

Any additional specific forces or heat sources can be added when necessary. The gravity force term is now included in the modified pressure term.

A.3 Wind model equations

The system of equations used in the wind model, as derived in previous research[12], is repeated here for completeness. The final set of equations is achieved through non-dimensionalizing the continuity and momentum equations (Equations A.82-A.83), applying a scale analysis and introducing a stream function. As the wind model only resolves the velocity field, the decoupled potential temperature equation (Equation A.84) is disregarded and no other force terms are added.

A.3.1 Non-dimensionalized equations

In order to non-dimensionalize, all variables are split into a dimensional reference constant ($\hat{\chi}$) and non-dimensional variable ($\breve{\chi}$):

$$x = \hat{x}\breve{x}, \qquad y = \hat{y}\breve{y}, \qquad z = \hat{z}\breve{z}, \qquad u = \hat{u}\breve{u}, \qquad v = \hat{v}\breve{v}, \qquad w = \hat{w}\breve{w}, \qquad p^* = \hat{p^*}\breve{p^*}, \qquad t = \hat{t}\breve{t} \tag{A.85}$$

First, the continuity equation is non-dimensionalized:

$$\frac{\hat{u}_j}{\hat{x}_j}\frac{\partial \breve{u}_j}{\partial \breve{x}_j} = 0 \tag{A.86}$$

It is then expanded and multiplied by $\hat{x}/\hat{u}$ in order to show the importance of the ratio of the scale constants in the non-dimensionalized continuity equation:

$$\frac{\partial \breve{u}}{\partial \breve{x}} + \frac{\hat{v}}{\hat{u}}\frac{\hat{x}}{\hat{y}}\frac{\partial \breve{v}}{\partial \breve{y}} + \frac{\hat{w}}{\hat{u}}\frac{\hat{x}}{\hat{z}}\frac{\partial \breve{w}}{\partial \breve{z}} = 0 \tag{A.87}$$

The non-dimensionalized conservation of momentum equation becomes:

$$\frac{\hat{u}_i}{\hat{t}}\frac{\partial \breve{u}_i}{\partial \breve{t}} + \frac{\hat{u}_i}{\hat{u}_j \hat{x}_j}\breve{u}_j\frac{\partial \breve{u}_i}{\partial \breve{x}_j} = -\frac{1}{\rho_0}\frac{\hat{p^*}}{\hat{x}_i}\frac{\partial \breve{p^*}}{\partial \breve{x}_i} + \frac{1}{\hat{x}_j}\frac{\partial}{\partial \breve{x}_j}\left(\nu\left(\frac{\hat{u}_i}{\hat{x}_j}\frac{\partial \breve{u}_i}{\partial \breve{x}_j} + \frac{\hat{u}_j}{\hat{x}_i}\frac{\partial \breve{u}_j}{\partial \breve{x}_i}\right)\right) + \delta_{i3} g \left(\frac{\delta\hat{\Theta}}{\Theta}\right)\left(\frac{\theta - \theta_0}{\theta_0}\right) + \hat{f}_{Cor,i}\breve{f}_{Cor,i} \qquad \text{for } i = 1,2,3 \tag{A.88}$$

Where the non-dimensionalized Coriolis force is:

$$\underset{\sim}{\hat{f}}_{Cor,i}\underset{\sim}{\breve{f}}_{Cor,i} = 2\omega \begin{Bmatrix} [\hat{u}\breve{u}\cos(a) + \hat{v}\breve{v}\sin(a)]\sin(\phi) - \hat{w}\breve{w}\cos(\phi) \\ -[\hat{u}\breve{u}\sin(a) + \hat{v}\breve{v}\cos(a)]\sin(\phi) \\ [\hat{u}\breve{u}\sin(a) + \hat{v}\breve{v}\cos(a)]\cos(\phi) \end{Bmatrix} \tag{A.89}$$

Note that the potential temperature term was already a dimensionless term as it was a relative fluctuation. It was however not yet appropriately scaled. As such, the scale term $\left(\frac{\delta\hat{\Theta}}{\Theta}\right)$ is added.

The momentum equation is then expanded to show all three directions individually. Multiplying each by $\hat{t}/\hat{u}$ results in:

$$\begin{aligned} i=1: \quad \frac{\partial\breve{u}}{\partial\breve{t}} + \frac{\hat{t}\hat{u}}{\hat{x}}\breve{u}\frac{\partial\breve{u}}{\partial\breve{x}} + \frac{\hat{t}\hat{v}}{\hat{y}}\breve{v}\frac{\partial\breve{u}}{\partial\breve{y}} + \frac{\hat{t}\hat{w}}{\hat{z}}\breve{w}\frac{\partial\breve{u}}{\partial\breve{z}} =& -\frac{\hat{t}\hat{p^*}}{\rho_0\hat{u}\hat{x}}\frac{\partial\breve{p^*}}{\partial\breve{x}} + \frac{\nu\hat{t}}{\hat{u}}\frac{\hat{u}}{\hat{x}^2}\left(\frac{\partial^2\breve{u}}{\partial\breve{x}^2} + \frac{\hat{x}^2}{\hat{y}^2}\frac{\partial^2\breve{u}}{\partial\breve{y}^2} + \frac{\hat{x}^2}{\hat{z}^2}\frac{\partial^2\breve{u}}{\partial\breve{z}^2}\right) \\ &+ 2\omega\hat{u}\frac{\hat{t}}{\hat{u}}\left(\left[\breve{u}\cos(a) + \frac{\hat{v}}{\hat{u}}\breve{v}\sin(a)\right]\sin(\phi)\right. \\ &\left. - \frac{\hat{w}}{\hat{u}}\breve{w}\cos(\phi)\right) \end{aligned} \tag{A.90}$$

$$\begin{aligned} i=2: \quad \frac{\partial\breve{v}}{\partial\breve{t}} + \frac{\hat{t}\hat{u}}{\hat{x}}\breve{u}\frac{\partial\breve{v}}{\partial\breve{x}} + \frac{\hat{t}\hat{v}}{\hat{y}}\breve{v}\frac{\partial\breve{v}}{\partial\breve{y}} + \frac{\hat{t}\hat{w}}{\hat{z}}\breve{w}\frac{\partial\breve{v}}{\partial\breve{z}} =& -\frac{\hat{t}\hat{p^*}}{\rho_0\hat{v}\hat{y}}\frac{\partial\breve{p^*}}{\partial\breve{y}} + \frac{\nu\hat{t}}{\hat{v}}\frac{\hat{v}}{\hat{x}^2}\left(\frac{\partial^2\breve{v}}{\partial\breve{x}^2} + \frac{\hat{x}^2}{\hat{y}^2}\frac{\partial^2\breve{v}}{\partial\breve{y}^2} + \frac{\hat{x}^2}{\hat{z}^2}\frac{\partial^2\breve{v}}{\partial\breve{z}^2}\right) \\ &+ 2\omega\hat{u}\frac{\hat{t}}{\hat{v}}\left[\breve{u}\sin(a) + \frac{\hat{v}}{\hat{u}}\breve{v}\cos(a)\right]\sin(\phi) \end{aligned} \tag{A.91}$$

$$\begin{aligned} i=3: \quad \frac{\partial\breve{w}}{\partial\breve{t}} + \frac{\hat{t}\hat{u}}{\hat{x}}\breve{u}\frac{\partial\breve{w}}{\partial\breve{x}} + \frac{\hat{t}\hat{v}}{\hat{y}}\breve{v}\frac{\partial\breve{w}}{\partial\breve{y}} + \frac{\hat{t}\hat{w}}{\hat{z}}\breve{w}\frac{\partial\breve{w}}{\partial\breve{z}} =& -\frac{\hat{t}\hat{p^*}}{\rho_0\hat{w}\hat{z}}\frac{\partial\breve{p^*}}{\partial\breve{z}} + \frac{\nu\hat{t}}{\hat{w}}\frac{\hat{w}}{\hat{x}^2}\left(\frac{\partial^2\breve{w}}{\partial\breve{x}^2} + \frac{\hat{x}^2}{\hat{y}^2}\frac{\partial^2\breve{w}}{\partial\breve{y}^2} + \frac{\hat{x}^2}{\hat{z}^2}\frac{\partial^2\breve{w}}{\partial\breve{z}^2}\right) \\ &+ \frac{\hat{t}}{\hat{w}}g\left(\frac{\delta\hat{\Theta}}{\Theta}\right)\left(\frac{\theta-\theta_0}{\theta_0}\right) \\ &+ 2\omega\hat{u}\frac{\hat{t}}{\hat{w}}\left[\breve{u}\sin(a) + \frac{\hat{v}}{\hat{u}}\breve{v}\cos(a)\right]\cos(\phi) \end{aligned} \tag{A.92}$$

The reference constant for time $\hat{t}$ can be chosen in order to simplify the equations, specifically:

$$\hat{t} = \frac{\hat{x}}{\hat{u}} \tag{A.93}$$

This is valid as the result is still in units of time. When applied to the momentum equations, they can be reordered in order to show the ratios between the scaling parameters:

$$i=1: \quad \frac{\partial \breve{u}}{\partial \breve{t}} + \breve{u}\frac{\partial \breve{u}}{\partial \breve{x}} + \frac{\hat{v}}{\hat{u}}\frac{\hat{x}}{\hat{y}}\breve{v}\frac{\partial \breve{u}}{\partial \breve{y}} + \frac{\hat{w}}{\hat{u}}\frac{\hat{x}}{\hat{z}}\breve{w}\frac{\partial \breve{u}}{\partial \breve{z}} = -\frac{\hat{p^*}}{\rho_0 \hat{u}^2}\frac{\partial \breve{p^*}}{\partial \breve{x}} + \frac{\nu}{\hat{u}\hat{x}}\left(\frac{\partial^2 \breve{u}}{\partial \breve{x}^2} + \left(\frac{\hat{x}}{\hat{y}}\right)^2\frac{\partial^2 \breve{u}}{\partial \breve{y}^2} + \left(\frac{\hat{x}}{\hat{z}}\right)^2\frac{\partial^2 \breve{u}}{\partial \breve{z}^2}\right) + \frac{2\omega\hat{x}}{\hat{u}}\left(\left[\breve{u}\cos(a) + \frac{\hat{v}}{\hat{u}}\breve{v}\sin(a)\right]\sin(\phi) - \frac{\hat{w}}{\hat{u}}\breve{w}\cos(\phi)\right) \tag{A.94}$$

$$i=2: \quad \frac{\partial \breve{v}}{\partial \breve{t}} + \breve{u}\frac{\partial \breve{v}}{\partial \breve{x}} + \frac{\hat{v}}{\hat{u}}\frac{\hat{x}}{\hat{y}}\breve{v}\frac{\partial \breve{v}}{\partial \breve{y}} + \frac{\hat{w}}{\hat{u}}\frac{\hat{x}}{\hat{z}}\breve{w}\frac{\partial \breve{v}}{\partial \breve{z}} = -\frac{\hat{p^*}}{\rho_0 \hat{u}^2}\frac{\hat{u}}{\hat{v}}\frac{\hat{x}}{\hat{y}}\frac{\partial \breve{p^*}}{\partial \breve{y}} + \frac{\nu}{\hat{u}\hat{x}}\left(\frac{\partial^2 \breve{v}}{\partial \breve{x}^2} + \left(\frac{\hat{x}}{\hat{y}}\right)^2\frac{\partial^2 \breve{v}}{\partial \breve{y}^2} + \left(\frac{\hat{x}}{\hat{z}}\right)^2\frac{\partial^2 \breve{v}}{\partial \breve{z}^2}\right) + \frac{2\omega\hat{x}}{\hat{v}}\left[\breve{u}\sin(a) + \frac{\hat{v}}{\hat{u}}\breve{v}\cos(a)\right]\sin(\phi) \tag{A.95}$$

$$i=3: \quad \frac{\partial \breve{w}}{\partial \breve{t}} + \breve{u}\frac{\partial \breve{w}}{\partial \breve{x}} + \frac{\hat{v}}{\hat{u}}\frac{\hat{x}}{\hat{y}}\breve{v}\frac{\partial \breve{w}}{\partial \breve{y}} + \frac{\hat{w}}{\hat{u}}\frac{\hat{x}}{\hat{z}}\breve{w}\frac{\partial \breve{w}}{\partial \breve{z}} = -\frac{\hat{p^*}}{\rho_0 \hat{u}^2}\frac{\hat{u}}{\hat{w}}\frac{\hat{x}}{\hat{z}}\frac{\partial \breve{p^*}}{\partial \breve{z}} + \frac{\nu}{\hat{u}\hat{x}}\left(\frac{\partial^2 \breve{w}}{\partial \breve{x}^2} + \left(\frac{\hat{x}}{\hat{y}}\right)^2\frac{\partial^2 \breve{w}}{\partial \breve{y}^2} + \left(\frac{\hat{x}}{\hat{z}}\right)^2\frac{\partial^2 \breve{w}}{\partial \breve{z}^2}\right) + \frac{g\hat{x}}{\hat{u}\hat{w}}\left(\frac{\delta\hat{\Theta}}{\Theta}\right)\left(\frac{\theta-\theta_0}{\theta_0}\right) + \frac{2\omega\hat{x}}{\hat{w}}\left[\breve{u}\sin(a) + \frac{\hat{v}}{\hat{u}}\breve{v}\cos(a)\right]\cos(\phi) \tag{A.96}$$

The previous paper[12] contains an overview of the dimensionless numbers which can be identified in these equations to provide additional insights in their workings.

A.3.2 Scale analysis

In order to scale the current problem appropriately the orders of magnitude of the constants (Table A.1) and the scale parameters (Table A.2) are determined. The characteristic scale parameters are based on large eddy simulation data for atmospheric boundary layer wind fields[11].

Table A.1: Constants (orders of magnitude)

ρ_0	$\sim 10^0$	kg/m^3	density (air)
ν	$\sim 10^{-5}$	m^2/s	kinematic viscosity (air)
g	$\sim 10^1$	m/s^2	gravitational acceleration
2ω	$\sim 10^{-4}$	rad/s	planetary rotation speed

The scale parameters are then applied to the non-dimensional equations (Equations A.87, A.94-A.96). The scaling of each term in the equations is shown in Tables A.3-A.6.

Table A.2: Characteristic scale parameters

$\hat{x}$	$\sim 10^2$	m	longitudinal length scale
$\hat{y}$	$\sim 10^2$	m	transversal length scale
$\hat{z}$	$\sim 10^1$	m	vertical length scale
$\hat{u}$	$\sim 10^1$	m/s	longitudinal velocity scale
$\hat{v}$	$\sim 10^1$	m/s	transverse velocity scale
$\hat{w}$	$\sim 10^{-2}$	m/s	vertical velocity scale
$\hat{p^*}$	$\sim 10^1$	Pa	modified pressure fluctuation scale
$\left(\frac{\hat{\delta\Theta}}{\Theta}\right)$	$\sim 10^{-1}$	–	relative temperature fluctuation scale
$\hat{t}$	$\sim \hat{x}/\hat{u}$	s	time scale

Table A.3: Scale analysis of the continuity equation (Eq. A.87)

$\frac{\partial\breve{u}}{\partial\breve{x}}$	$\frac{\partial\breve{v}}{\partial\breve{y}}$	$\frac{\partial\breve{w}}{\partial\breve{z}}$
–	$\frac{\hat{v}}{\hat{u}}\frac{\hat{x}}{\hat{y}}$	$\frac{\hat{w}}{\hat{u}}\frac{\hat{x}}{\hat{z}}$
10^0	10^0	10^{-2}

Table A.4: Scale analysis of the conservation of momentum equation, $i = 1$ (Eq. A.94)

$\frac{\partial\breve{u}}{\partial\breve{t}}$	$\breve{u}\frac{\partial\breve{u}}{\partial\breve{x}}$	$\breve{v}\frac{\partial\breve{u}}{\partial\breve{y}}$	$\breve{w}\frac{\partial\breve{u}}{\partial\breve{z}}$	$\frac{\partial\breve{p^*}}{\partial\breve{x}}$	$\frac{\partial^2\breve{u}}{\partial\breve{x}^2}$	$\frac{\partial^2\breve{u}}{\partial\breve{y}^2}$	$\frac{\partial^2\breve{u}}{\partial\breve{z}^2}$	$\breve{u}$	$\breve{v}$	$\breve{w}$
–	–	$\frac{\hat{v}}{\hat{u}}\frac{\hat{x}}{\hat{y}}$	$\frac{\hat{w}}{\hat{u}}\frac{\hat{x}}{\hat{z}}$	$\frac{\hat{p^*}}{\rho_0\hat{u}^2}$	$\frac{\nu}{\hat{u}\hat{x}}$	$\frac{\nu\hat{x}}{\hat{u}\hat{y}^2}$	$\frac{\nu\hat{x}}{\hat{u}\hat{z}^2}$	$\frac{2\omega\hat{x}\mathrm{s}(\phi)^*}{\hat{u}}$	$\frac{2\omega\hat{x}\hat{v}\mathrm{s}(\phi)\mathrm{c}(a)^\ddagger}{\hat{u}^2}$	$\frac{2\omega\hat{x}\hat{w}\mathrm{c}(\phi)\mathrm{s}(a)^\ddagger}{\hat{u}^2}$
10^0	10^0	10^0	10^{-2}	10^{-1}	10^{-8}	10^{-8}	10^{-6}	$10^{-3\dagger}$	$10^{-3\dagger}$	$10^{-6\dagger}$

Table A.5: Scale analysis of the conservation of momentum equation, $i = 2$ (Eq. A.95)

$\frac{\partial\breve{v}}{\partial\breve{t}}$	$\breve{u}\frac{\partial\breve{v}}{\partial\breve{x}}$	$\breve{v}\frac{\partial\breve{v}}{\partial\breve{y}}$	$\breve{w}\frac{\partial\breve{v}}{\partial\breve{z}}$	$\frac{\partial\breve{p^*}}{\partial\breve{y}}$	$\frac{\partial^2\breve{v}}{\partial\breve{x}^2}$	$\frac{\partial^2\breve{v}}{\partial\breve{y}^2}$	$\frac{\partial^2\breve{v}}{\partial\breve{z}^2}$	$\breve{u}$	$\breve{v}$
–	–	$\frac{\hat{v}}{\hat{u}}\frac{\hat{x}}{\hat{y}}$	$\frac{\hat{w}}{\hat{u}}\frac{\hat{x}}{\hat{z}}$	$\frac{\hat{p^*}\hat{x}}{\rho_0\hat{u}\hat{v}\hat{y}}$	$\frac{\nu}{\hat{u}\hat{x}}$	$\frac{\nu\hat{x}}{\hat{u}\hat{y}^2}$	$\frac{\nu\hat{x}}{\hat{u}\hat{z}^2}$	$\frac{2\omega\hat{x}\mathrm{s}(\phi)\mathrm{s}(a)^\ddagger}{\hat{v}}$	$\frac{2\omega\hat{x}\mathrm{s}(\phi)\mathrm{c}(a)^\ddagger}{\hat{u}}$
10^0	10^0	10^0	10^{-2}	10^{-1}	10^{-8}	10^{-8}	10^{-6}	$10^{-3\dagger}$	$10^{-3\dagger}$

Table A.6: Scale analysis of the conservation of momentum equation, $i = 3$ (Eq. A.96)

$\frac{\partial\breve{w}}{\partial\breve{t}}$	$\breve{u}\frac{\partial\breve{w}}{\partial\breve{x}}$	$\breve{v}\frac{\partial\breve{w}}{\partial\breve{y}}$	$\breve{w}\frac{\partial\breve{w}}{\partial\breve{z}}$	$\frac{\partial\breve{p^*}}{\partial\breve{z}}$	$\frac{\partial^2\breve{w}}{\partial\breve{x}^2}$	$\frac{\partial^2\breve{w}}{\partial\breve{y}^2}$	$\frac{\partial^2\breve{w}}{\partial\breve{z}^2}$	$\left(\frac{\theta-\theta_0}{\theta_0}\right)$	$\breve{u}$	$\breve{v}$
–	–	$\frac{\hat{v}}{\hat{u}}\frac{\hat{x}}{\hat{y}}$	$\frac{\hat{w}}{\hat{u}}\frac{\hat{x}}{\hat{z}}$	$\frac{\hat{p^*}\hat{x}}{\rho_0\hat{u}\hat{w}\hat{z}}$	$\frac{\nu}{\hat{u}\hat{x}}$	$\frac{\nu\hat{x}}{\hat{u}\hat{y}^2}$	$\frac{\nu\hat{x}}{\hat{u}\hat{z}^2}$	$\frac{g\hat{x}}{\hat{u}\hat{w}}\left(\frac{\hat{\delta\Theta}}{\Theta}\right)$	$\frac{2\omega\hat{x}\mathrm{c}(\phi)\mathrm{c}(a)^\ddagger}{\hat{w}}$	$\frac{2\omega\hat{x}\hat{v}\mathrm{c}(\phi)\mathrm{s}(a)^\ddagger}{\hat{u}\hat{w}}$
10^0	10^0	10^0	10^{-2}	10^3	10^{-8}	10^{-8}	10^{-6}	10^3	$10^{-4\dagger}$	$10^{-4\dagger}$

Based on the scale analysis of Tables A.3-A.6, only the dominant terms are retained. The non-dimensional equations become:

$$\frac{\partial \breve{u}}{\partial \breve{x}} + \frac{\partial \breve{v}}{\partial \breve{y}} = 0 \tag{A.97}$$

$i = 1:$
$$\frac{\partial \breve{u}}{\partial \breve{t}} + \breve{u}\frac{\partial \breve{u}}{\partial \breve{x}} + \breve{v}\frac{\partial \breve{u}}{\partial \breve{y}} = 0 \tag{A.98}$$

$i = 2:$
$$\frac{\partial \breve{v}}{\partial \breve{t}} + \breve{u}\frac{\partial \breve{v}}{\partial \breve{x}} + \breve{v}\frac{\partial \breve{v}}{\partial \breve{y}} = 0 \tag{A.99}$$

$i = 3:$
$$0 = -\frac{\partial \breve{p^*}}{\partial \breve{z}} + \left(\frac{\theta - \theta_0}{\theta_0}\right) \tag{A.100}$$

Reverting to dimensional terms in the equations:

$$\frac{\partial u}{\partial x} + \frac{\partial v}{\partial y} = 0 \tag{A.101}$$

$i = 1:$
$$\frac{\partial u}{\partial t} + u\frac{\partial u}{\partial x} + v\frac{\partial u}{\partial y} = 0 \tag{A.102}$$

$i = 2:$
$$\frac{\partial v}{\partial t} + u\frac{\partial v}{\partial x} + v\frac{\partial v}{\partial y} = 0 \tag{A.103}$$

$i = 3:$
$$0 = -\frac{1}{\rho_0}\frac{\partial p^*}{\partial z} + g\left(\frac{\theta - \theta_0}{\theta_0}\right) \tag{A.104}$$

Upon analysis of the remaining system of equations, it is clear that the momentum equation for $i = 3$ (Equation A.104) is decoupled from the rest. This indicates that the velocity field in the horizontal plane (Equations A.101-A.103) is independent of the vertical direction and can be analysed separately. Furthermore, no pressure or viscous effects are retained which prohibits modeling any turbulent evolution. Through only keeping the dominant advection terms, Taylor's frozen turbulence hypothesis is therefore implicitly assumed.

A.3.3 Stream function

After scaling only two unknowns remain: u, v. These can be coupled to a single variable:

$$u = f(\phi), \qquad v = g(\phi) \qquad \text{with } \phi = \phi(x, y, t) \tag{A.105}$$

Choosing ϕ intelligently such that the continuity equation is automatically satisfied would mean an additional simplification. Therefore the unknown functions are substituted into the continuity equation:

$$\frac{\partial u}{\partial x} + \frac{\partial v}{\partial y} = \frac{\partial f(\phi)}{\partial x} + \frac{\partial g(\phi)}{\partial y} = 0 \tag{A.106}$$

[‡] s( ) and c( ) are used as short-hand notations of sin( ) and cos( )

[†] These parameters depend on the specific latitude and azimuth. The maximum possible value has been used here.

In order to attempt to compare the terms, $f(\phi)$ is chosen as a y-derivative:

$$f(\phi) = \frac{\partial \phi}{\partial y} \tag{A.107}$$

Substituted into the equation:

$$\frac{\partial}{\partial x}\left(\frac{\partial \phi}{\partial y}\right) + \frac{\partial g(\phi)}{\partial y} = 0 \tag{A.108}$$

Due to the symmetry of second derivatives, the order of derivation in the first term can be switched:

$$\frac{\partial}{\partial y}\left(\frac{\partial \phi}{\partial x}\right) + \frac{\partial g(\phi)}{\partial y} = 0 \tag{A.109}$$

In order to satisfy the equation, $g(\phi)$ must be:

$$\frac{\partial \phi}{\partial x} = -g(\phi) \tag{A.110}$$

The descriptions for u and v in terms of a stream function that inherently satisfies the mass conservation, have been found:

$$u = \frac{\partial \phi}{\partial y}, \qquad v = -\frac{\partial \phi}{\partial x} \tag{A.111}$$

The momentum conservation equations are then rewritten in terms of the stream function ϕ and reordered to obtain the final set of equations which the wind model aims to solve:

$$i = 1: \qquad \frac{\partial}{\partial t}\left(\frac{\partial \phi}{\partial y}\right) = -\frac{\partial \phi}{\partial y}\frac{\partial^2 \phi}{\partial x \partial y} + \frac{\partial \phi}{\partial x}\frac{\partial^2 \phi}{\partial y^2} \tag{A.112}$$

$$i = 2: \qquad \frac{\partial}{\partial t}\left(\frac{\partial \phi}{\partial x}\right) = -\frac{\partial \phi}{\partial y}\frac{\partial^2 \phi}{\partial x^2} + \frac{\partial \phi}{\partial x}\frac{\partial^2 \phi}{\partial x \partial y} \tag{A.113}$$

The model now consists of a set of only two equations, specifically the nonlinear, two-dimensional advection equations. A three-dimensional problem will be solved as a set of horizontal planes with a two-dimensional flow on each plane.

A.4 LES ABL equations

The velocity is decomposed into the resolved-scale velocity, $\tilde{u}_i$, and the subfilter-scale, u_i':

$$u_i = \tilde{u}_i + u_i' \tag{A.114}$$

A similar decomposition is applied to the other flow variables. The atmospheric boundary layer equations are only resolved for the filtered motions.

A.4.1 Filtered momentum equation

The ABL flows of interest are all high-Reynolds number flows. Combined with the fundamental idea of the LES filter, the influence of molecular viscosity on the resolved-scale motions can be neglected.[39] The filtered momentum equation becomes:

$$\frac{\partial \tilde{u}_i}{\partial t} + \tilde{u}_j \frac{\partial \tilde{u}_i}{\partial x_j} = -\frac{\partial \tilde{P}^*}{\partial x_i} - \frac{\partial \tau_{ij}^{\Delta}}{\partial x_j} + \delta_{i3} g \left(\frac{\tilde{\theta} - \tilde{\theta}_0}{\tilde{\theta}_0}\right) + \tilde{f}_{Cor,i} + \tilde{f}_i \qquad \text{for } i = 1, 2, 3 \tag{A.115}$$

where the trace of the subfilter-scale stress tensor is included within the modified kinematic pressure term:

$$P^* = \frac{p - \rho_0 g z}{\rho_0} + \frac{\sigma_{kk}}{3} \tag{A.116}$$

The deviatoric part of the subfilter-scale stress tensor, often also known as the residual stress tensor, is:

$$\tau_{ij}^{\Delta} = \widetilde{u_i u_j} - \tilde{u}_i \tilde{u}_j \tag{A.117}$$

Note that this is the often-presented equation in literature, but for τ_{ij}^{Δ} and σ_{kk} to have the dimensions of stress, the density must be included, as:

$$-\rho_0 \tau_{ij}^{\Delta} = \widetilde{u_i u_j} - \tilde{u}_i \tilde{u}_j \tag{A.118}$$

However, to stay in line with existing literature, the density will be omitted and the stresses mentioned will have the dimension of $\mathrm{m}^2/\mathrm{s}^2$. This is similar to the modified pressure and the Reynolds stress.

The term $\widetilde{u_i u_j}$ can be expanded using the Leonard identity:[40]

$$\widetilde{u_i u_j} = \widetilde{\tilde{u}_i \tilde{u}_j} + \widetilde{u_i' \tilde{u}_j} + \widetilde{\tilde{u}_i u_j'} + \widetilde{u_i' u_j'} \tag{A.119}$$

This shows that the resolved-scale shear stress now also contains subfilter-scale terms, defeating the purpose of filtering the equations. A closure model in terms of only resolved-scale quantities is therefore required. Several SFS stress models exist. The model used to generate the LES data for this research is based on the Smagorinsky-Lilly eddy-viscosity model:[22]

$$\tau_{ij}^{\Delta} = -2\nu_T \tilde{S}_{ij} \tag{A.120}$$

where ν_T is the eddy viscosity and $\tilde{S}_{ij}$ is the filtered strain-rate tensor:

$$\tilde{S}_{ij} = \frac{1}{2}\left(\frac{\partial u_i}{\partial x_j} + \frac{\partial u_j}{\partial x_i}\right) \tag{A.121}$$

The eddy viscosity is modeled as:

$$\nu_T = (C_s \Delta)^2 \sqrt{2 \tilde{S}_{ij} \tilde{S}_{ij}} \tag{A.122}$$

where C_s is the Smagorinsky coefficient for the SFS stress, which is calculated dynamically.[22]

A.4.2 Filtered temperature equation

Similarly to the momentum equation, the viscous heating term in the potential temperature equation is also eliminated. Fourier's law is used for the surface heating term. It is applied at state θ, p_0:

$$q_j = -k_t \frac{\partial \theta}{\partial x_j} = \rho c_p \alpha \frac{\partial \theta}{\partial x_j} \tag{A.123}$$

where k is the thermal conductivity and α thermal diffusivity.

The filtered potential temperature equation becomes:

$$\frac{\partial \tilde{\theta}}{\partial t} + \tilde{u}_j \frac{\partial \tilde{\theta}}{\partial x_j} = -\frac{\partial q_j^{\Delta}}{\partial x_j} + \frac{1}{\rho_0 c_p} \tilde{Q}|_{\theta, p_0} \tag{A.124}$$

where the sub-filter scale heat flux is:

$$q_j^{\Delta} = -\nu_\theta \frac{\partial \tilde{\theta}}{\partial x_j} \tag{A.125}$$

where the eddy thermal diffusivity is modeled as:

$$\nu_\theta = (D_s \Delta)^2 \sqrt{2 \tilde{S}_{ij} \tilde{S}_{ij}} \tag{A.126}$$

where D_s is the Smagorinsky coefficient for the SFS heat flux, which is calculated dynamically.[22]

B LES-data flow quantities

This section contains the height profiles of various flow quantities of the LES-data sets and the friction velocity over time.

B.1 Velocity profile

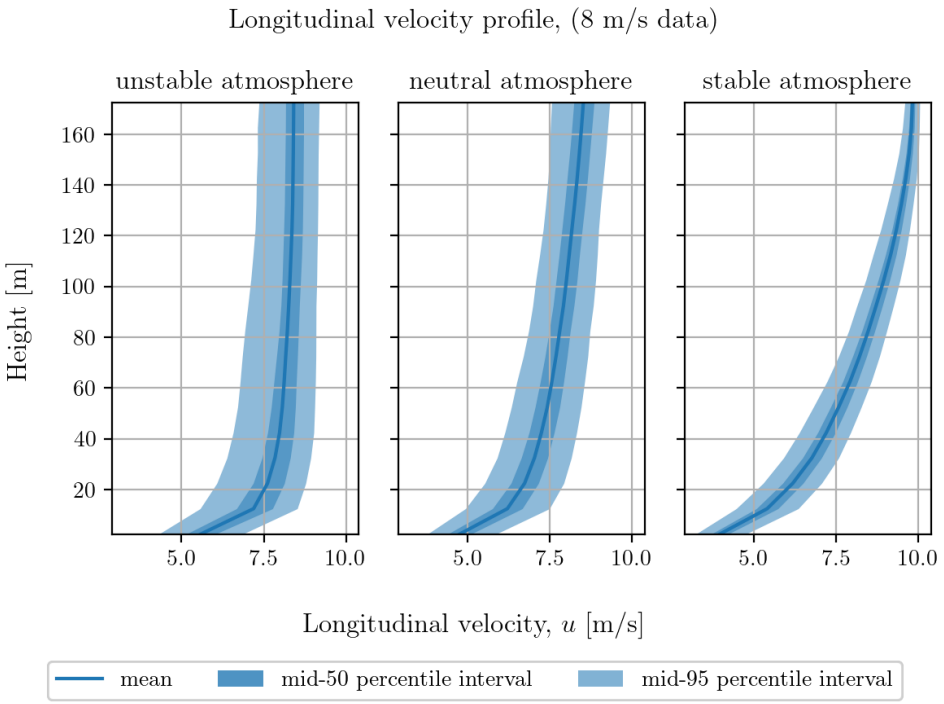

Figure B.1: Longitudinal velocity profile (Data set 1)

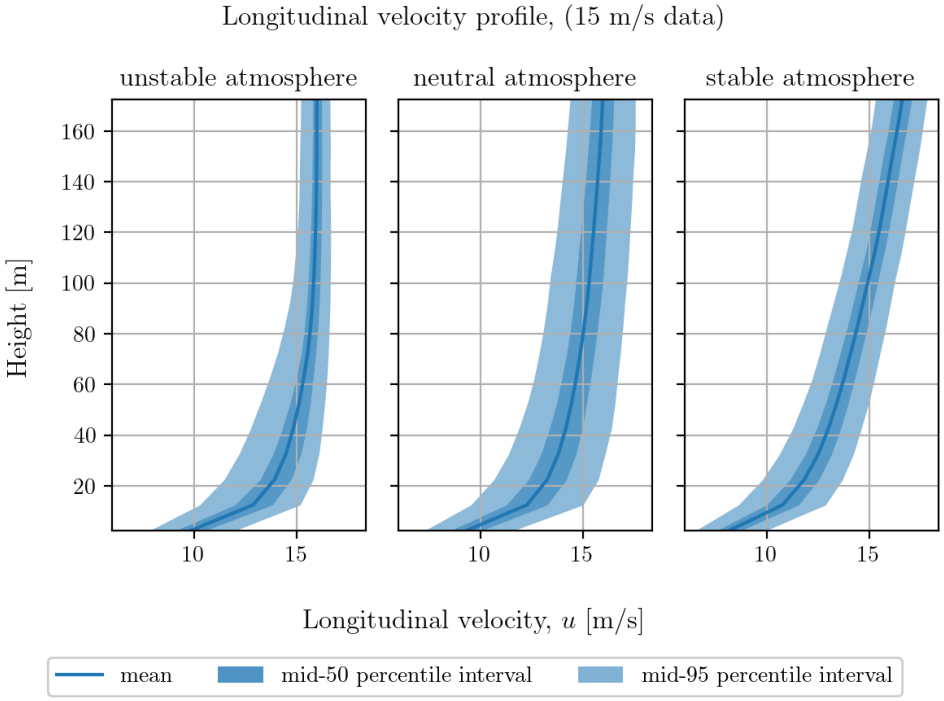

Figure B.2: Longitudinal velocity profile (Data set 2)

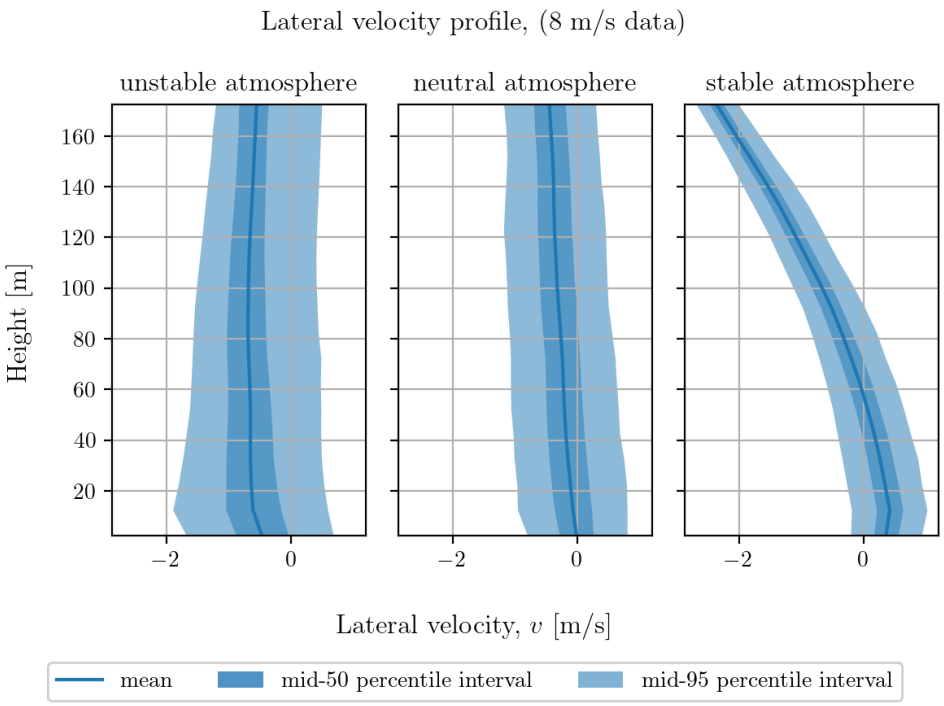

Figure B.3: Lateral velocity profile (Data set 1)

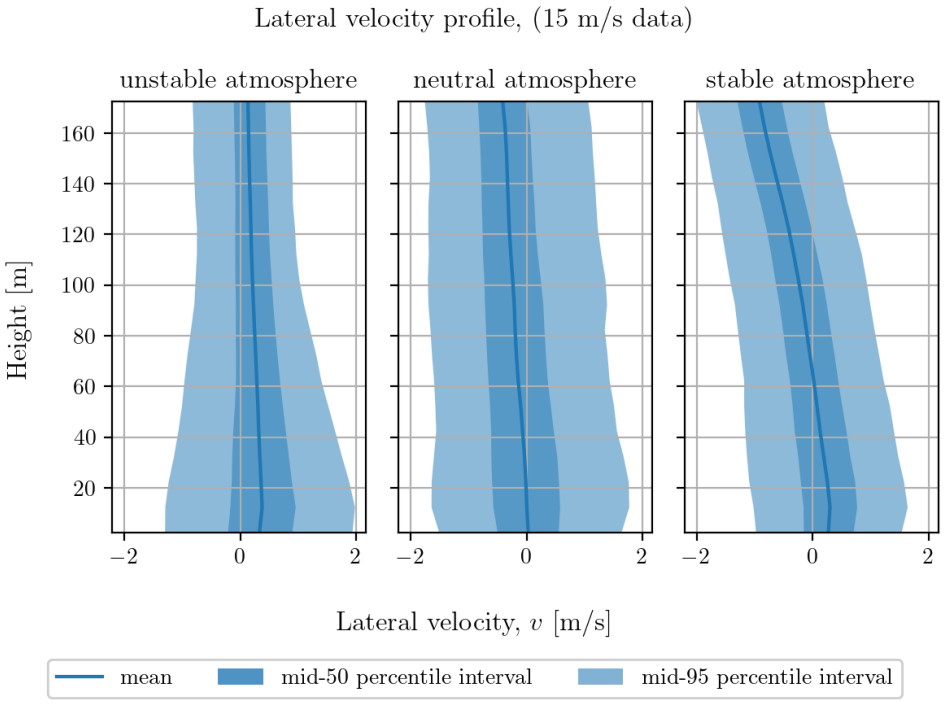

Figure B.4: Lateral velocity profile (Data set 2)

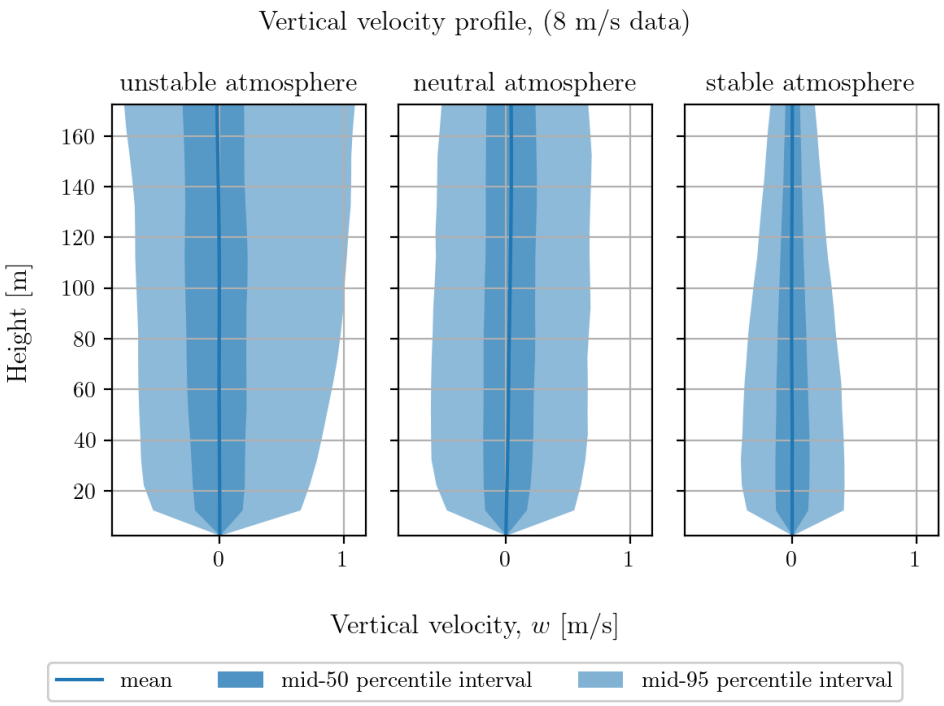

Figure B.5: Vertical velocity profile (Data set 1)

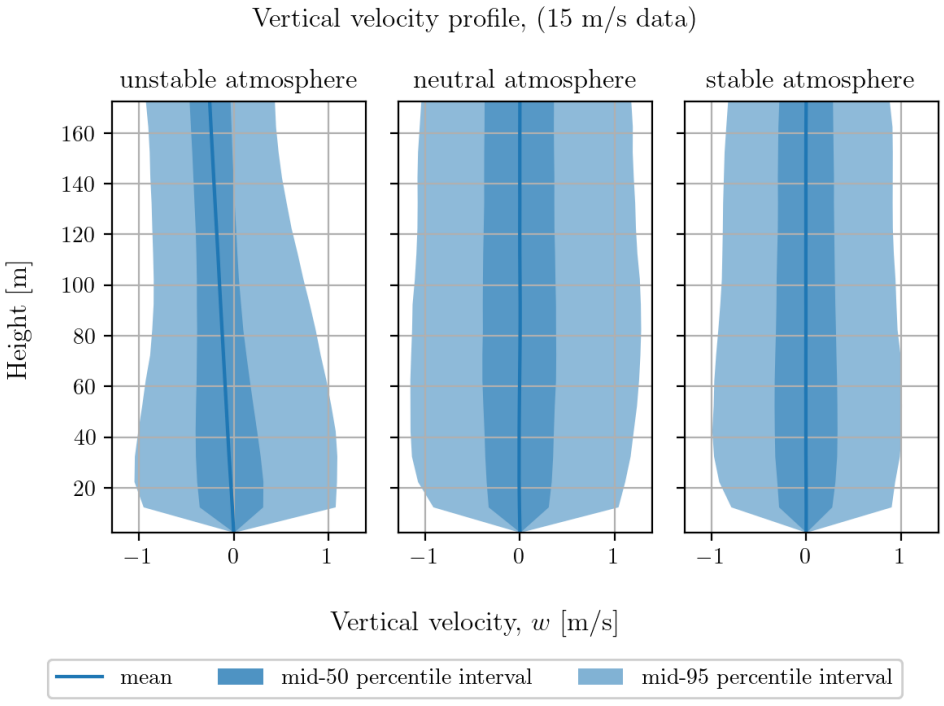

Figure B.6: Vertical velocity profile (Data set 2)

B.2 Time-averaged velocity profile

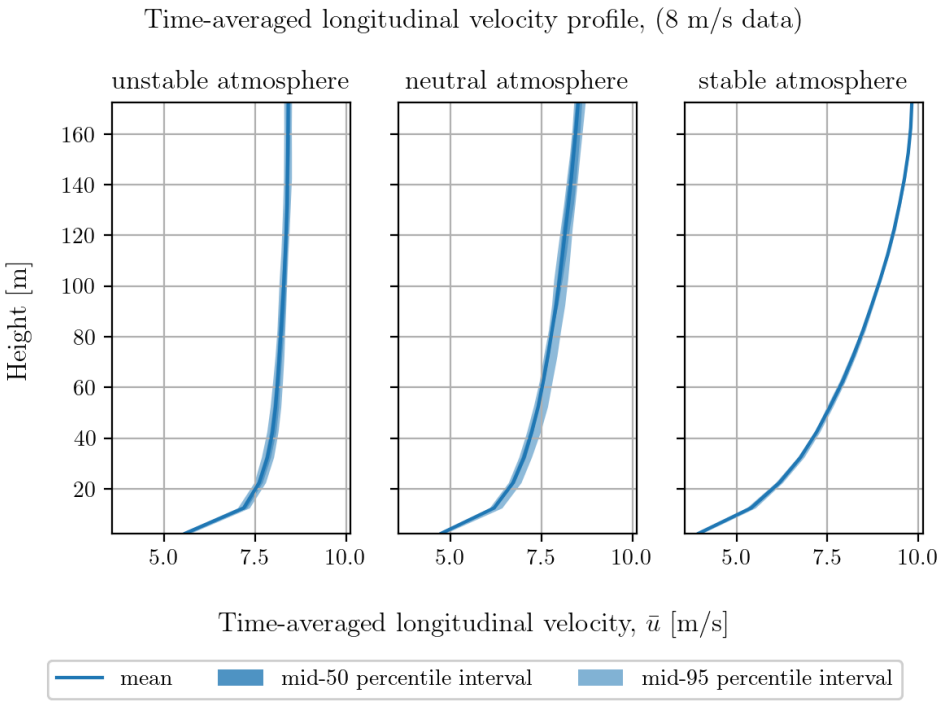

Figure B.7: Time-averaged longitudinal velocity profile (Data set 1)

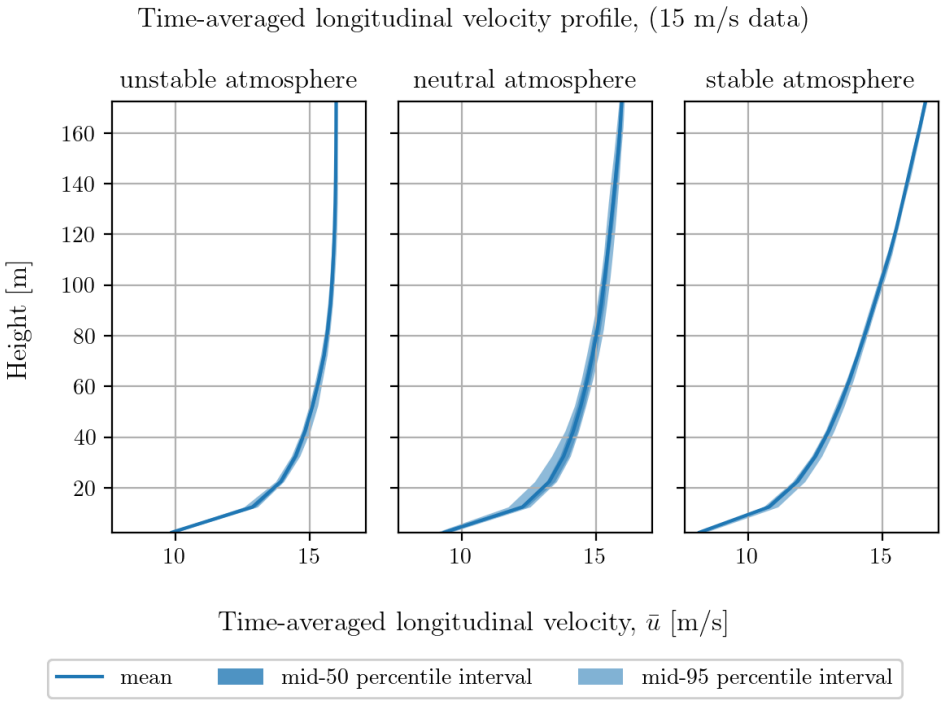

Figure B.8: Time-averaged longitudinal velocity profile (Data set 2)

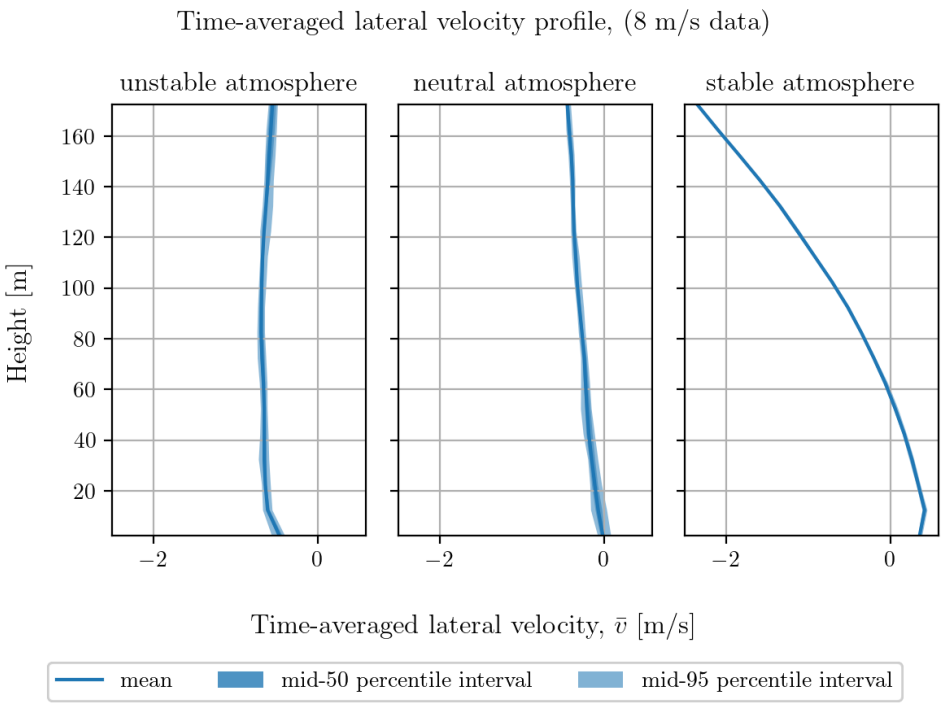

Figure B.9: Time-averaged lateral velocity profile (Data set 1)

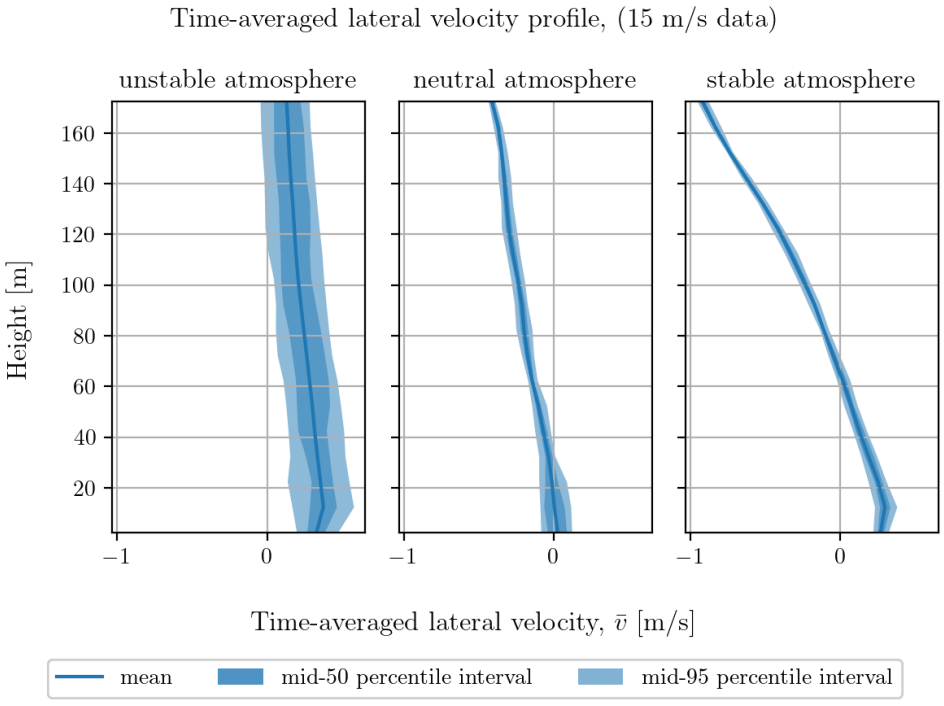

Figure B.10: Time-averaged lateral velocity profile (Data set 2)

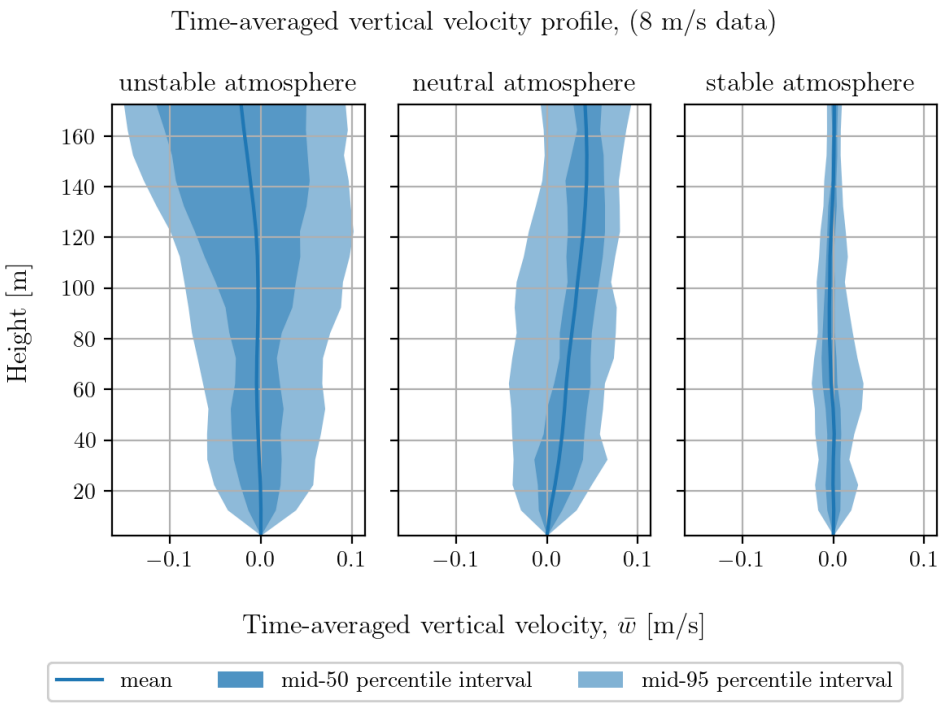

Figure B.11: Time-averaged vertical velocity profile (Data set 1)

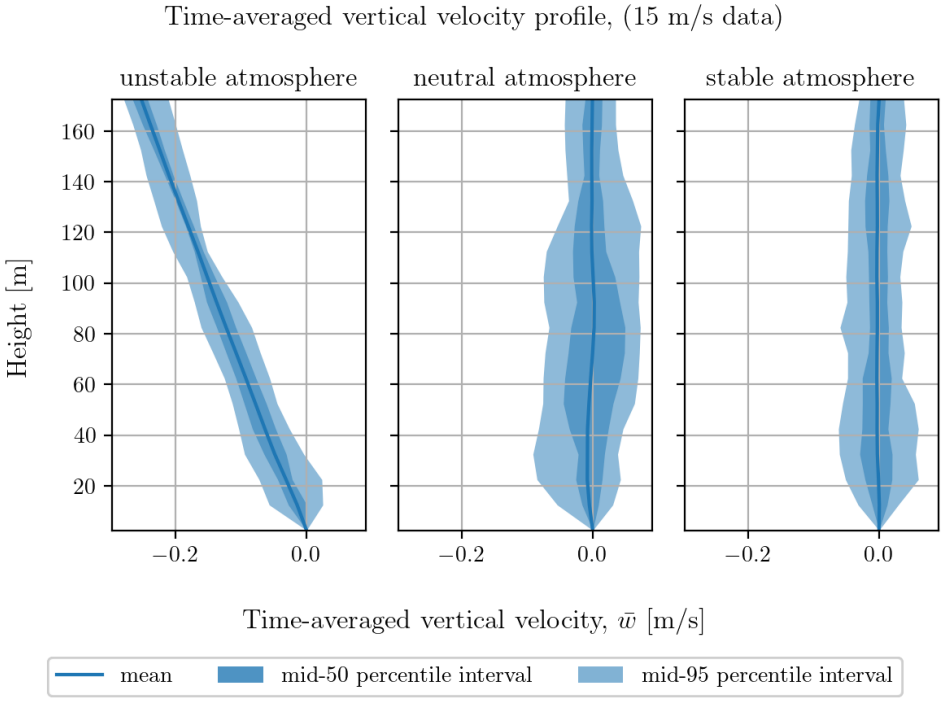

Figure B.12: Time-averaged vertical velocity profile (Data set 2)

B.3 Turbulence intensity profile

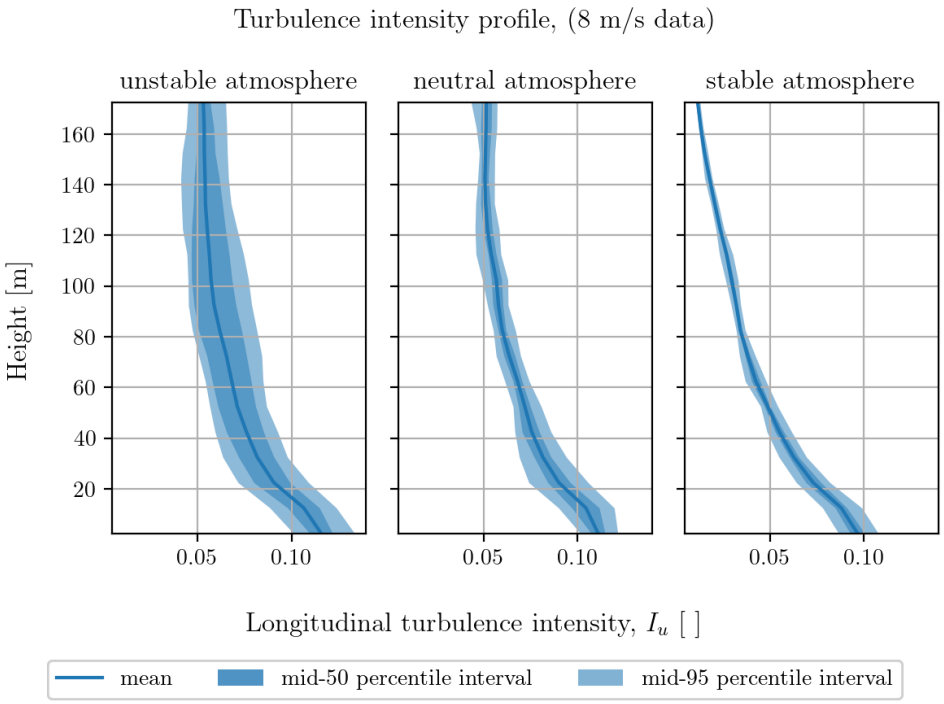

Figure B.13: Longitudinal turbulence intensity profile (Data set 1)

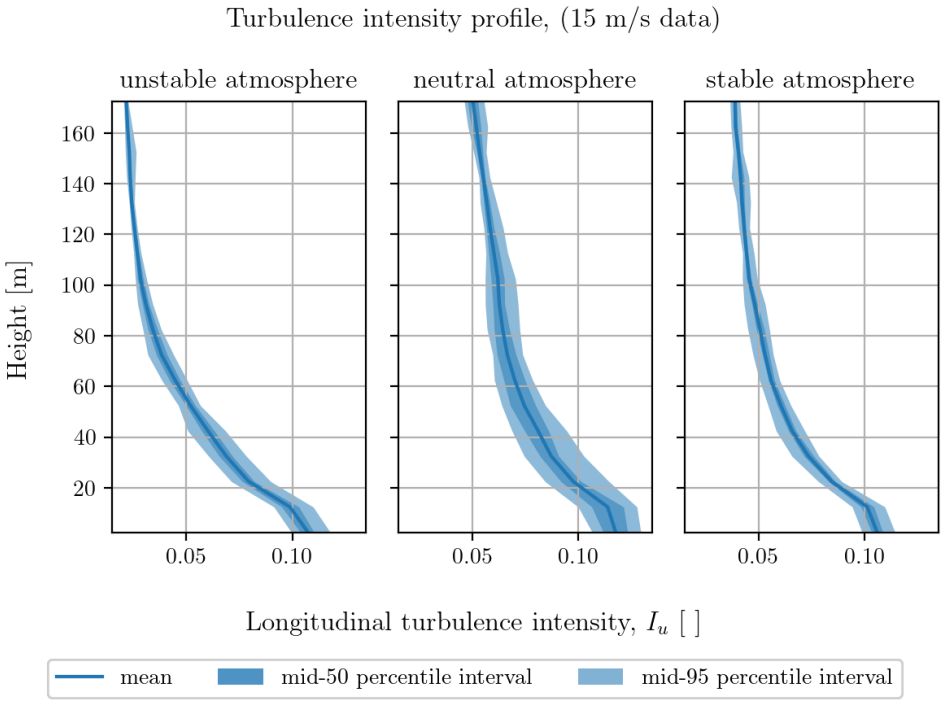

Figure B.14: Longitudinal turbulence intensity profile (Data set 2)

B.4 Turbulence kinetic energy profile

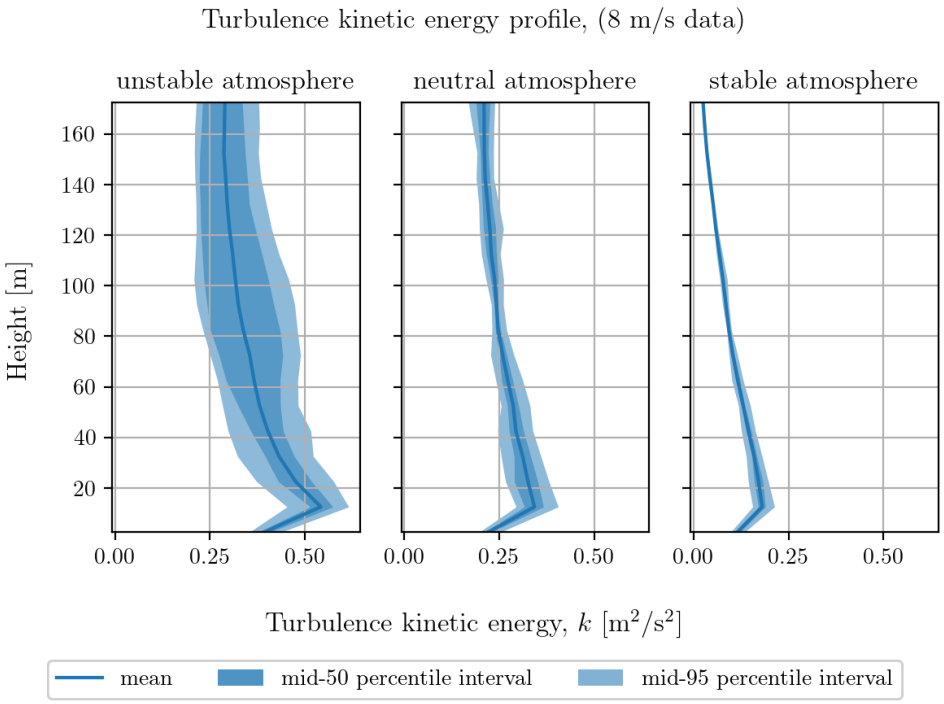

Figure B.15: Turbulence kinetic energy profile (Data set 1)

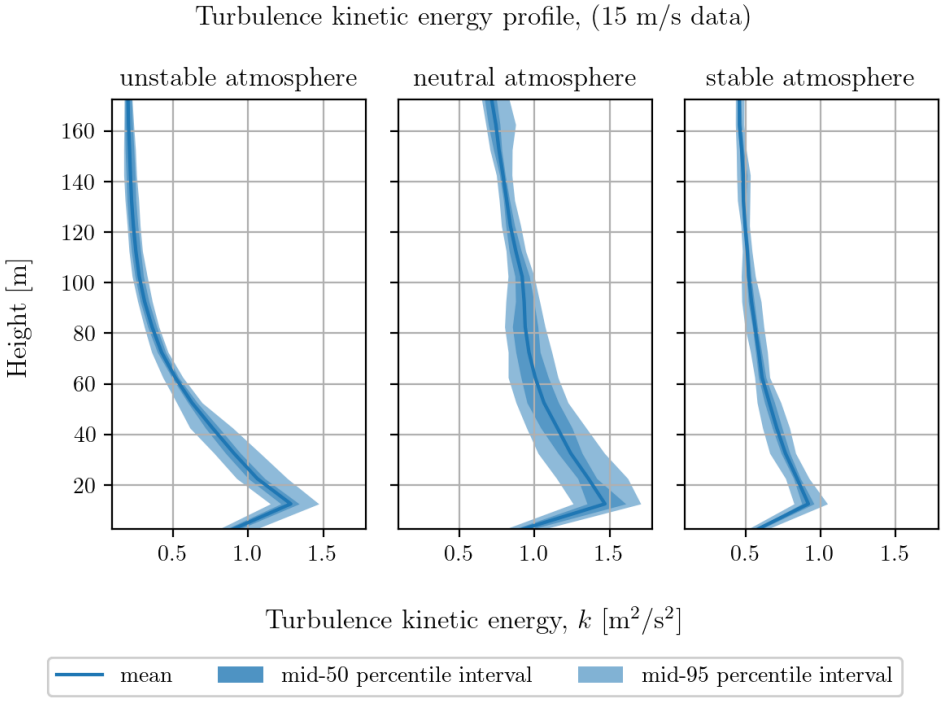

Figure B.16: Turbulence kinetic energy profile (Data set 2)

B.5 Virtual temperature profile

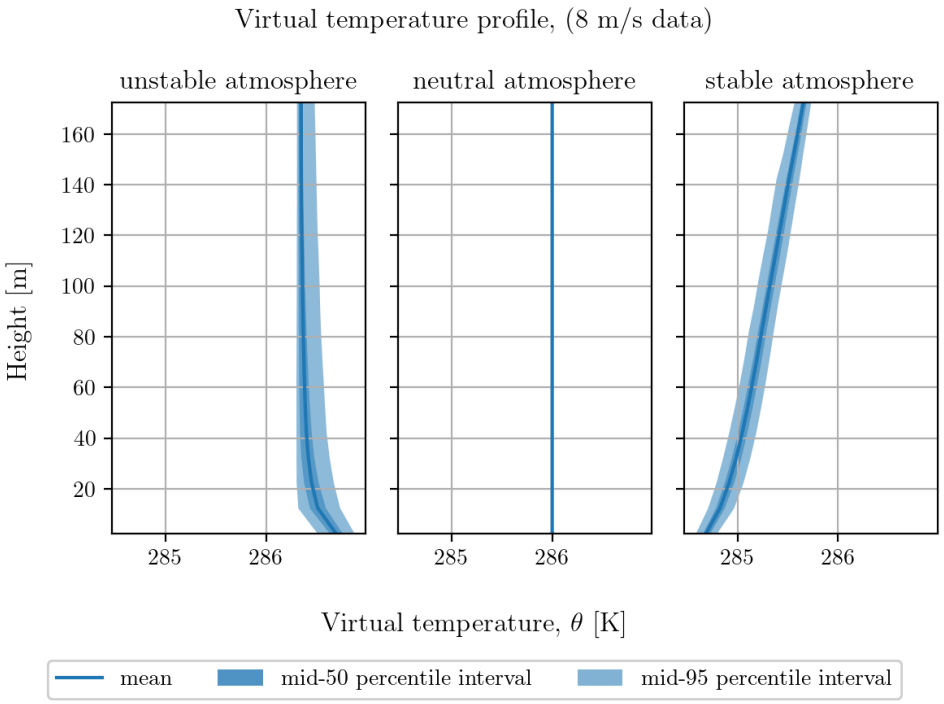

Figure B.17: Virtual temperature profile (Data set 1)

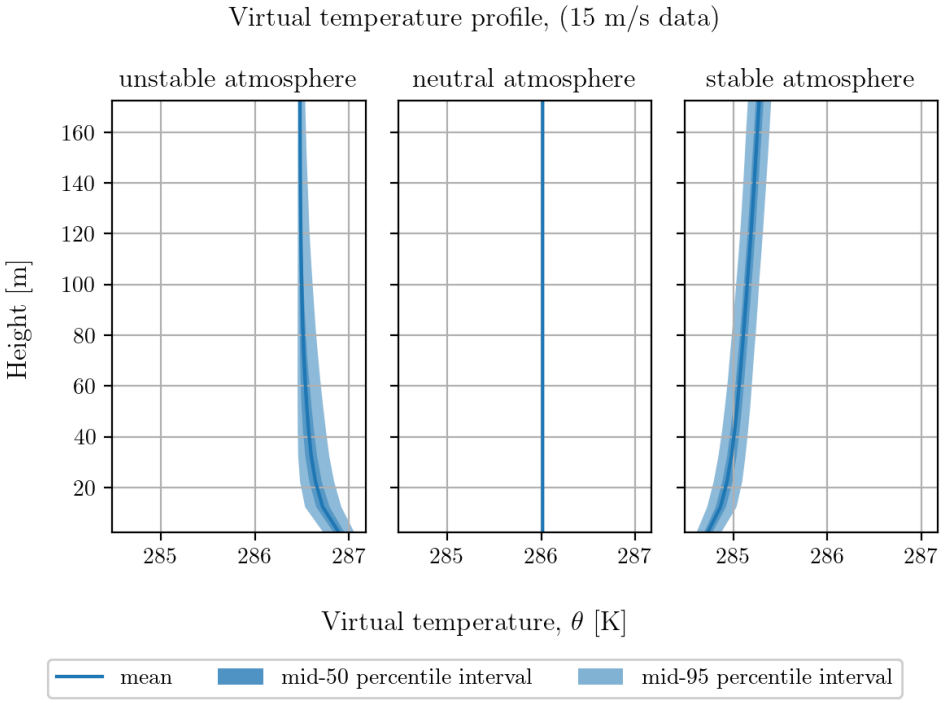

Figure B.18: Virtual temperature profile (Data set 2)

B.6 Friction velocity

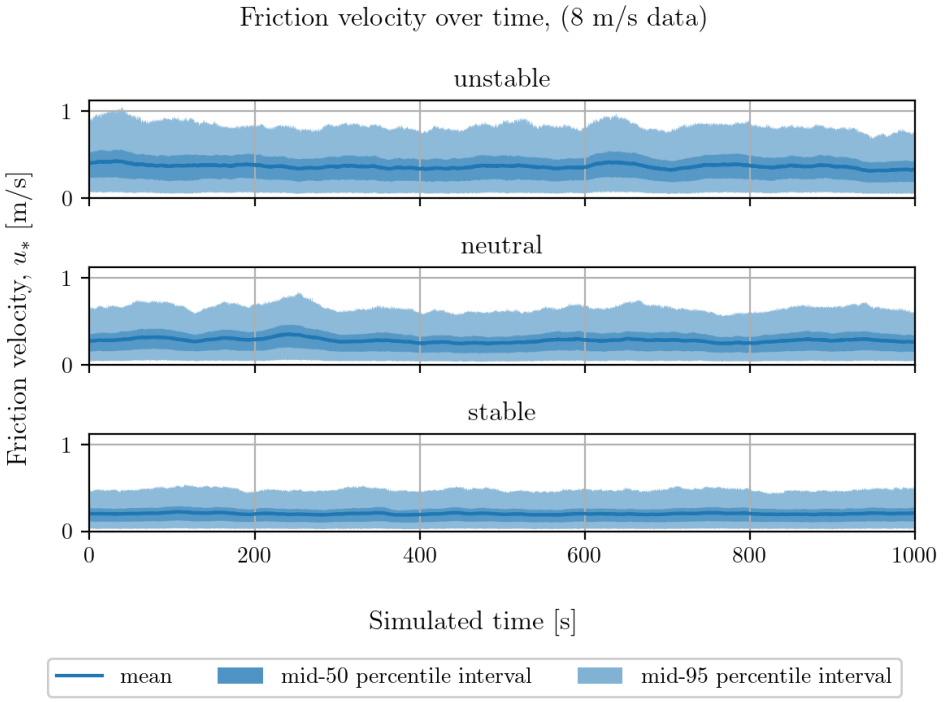

Figure B.19: Friction velocity (Data set 1)

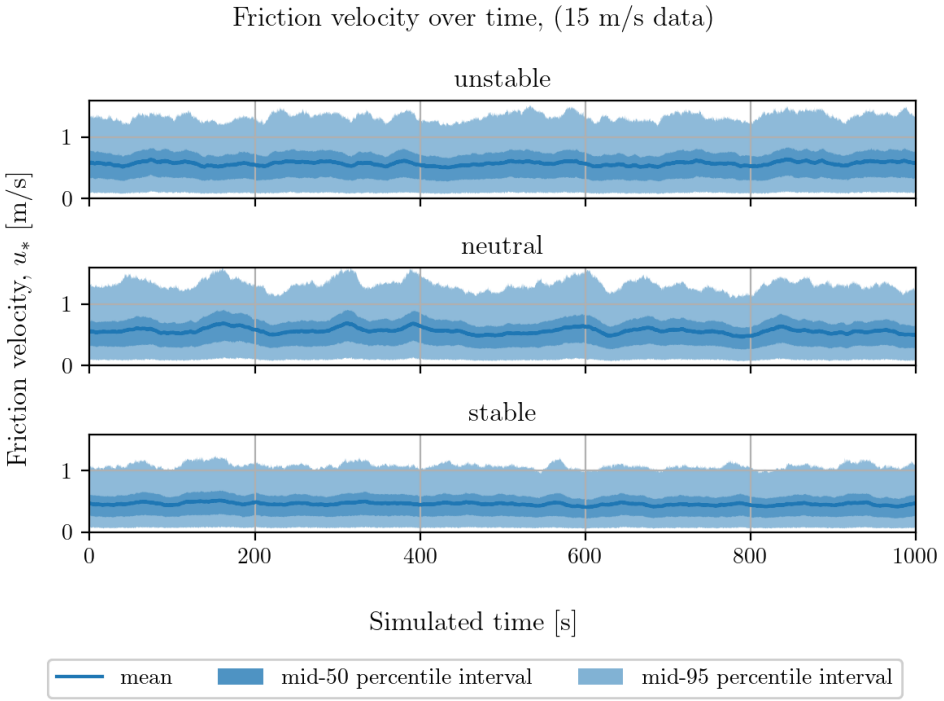

Figure B.20: Friction velocity (Data set 2)

B.7 Bulk Richardson number

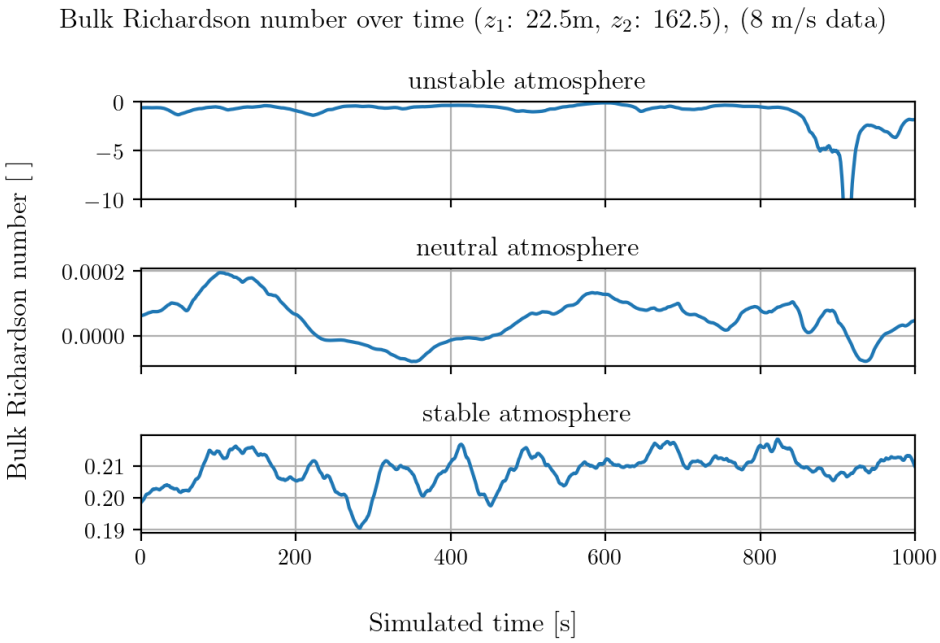

Figure B.21: Bulk Richardson number (Data set 1)

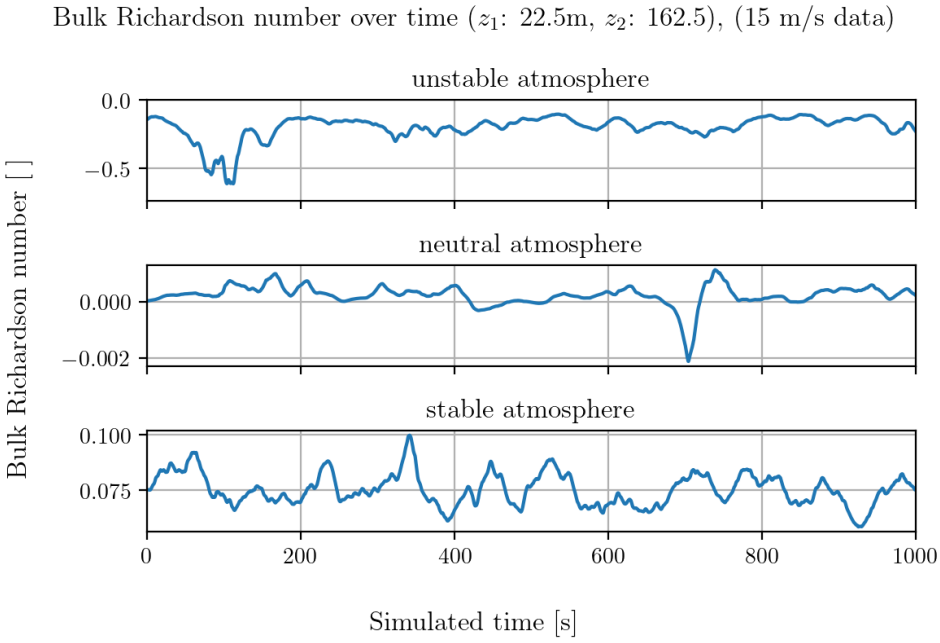

Figure B.22: Bulk Richardson number (Data set 2)

C Correlation and coherence related quantities

This section contains profiles and plots of various quantities related to the correlation and coherence investigated.

C.1 20% Auto-correlation cut-off time profile

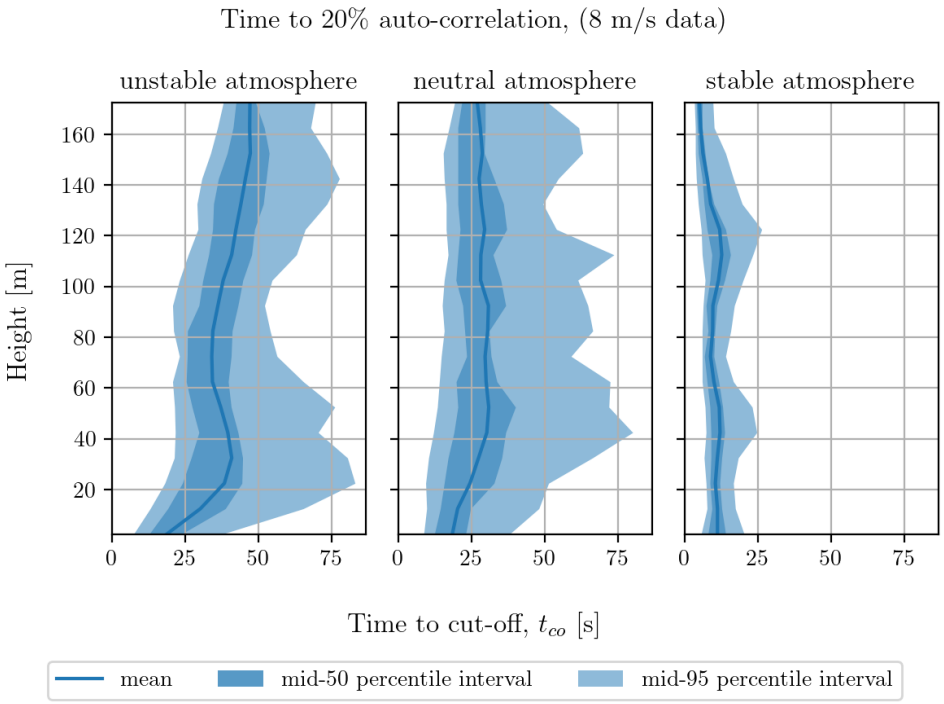

Figure C.1: 20% Auto-correlation cut-off time profile (Data set 1)

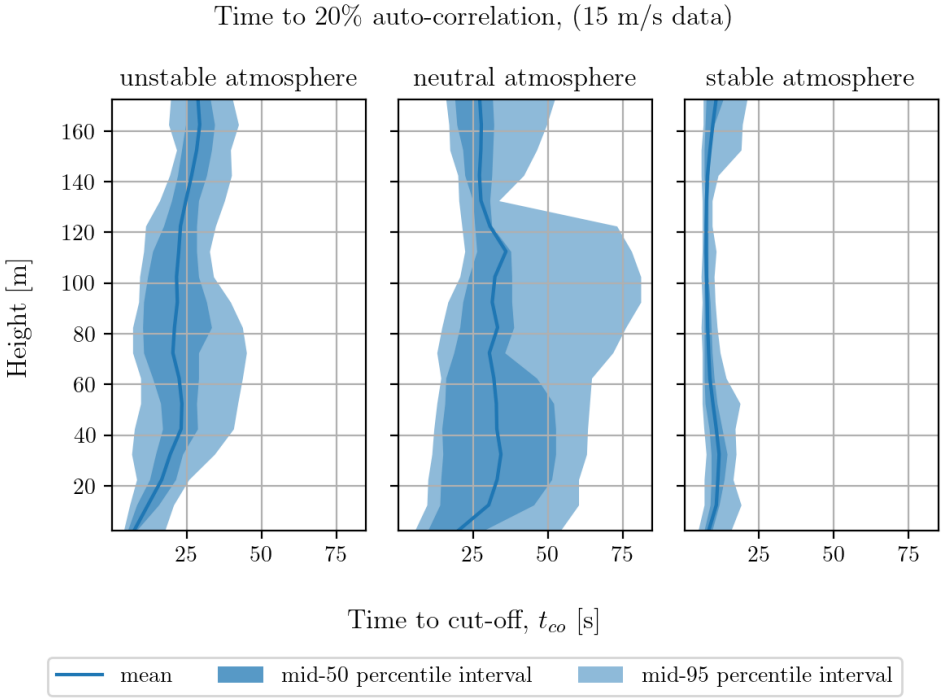

Figure C.2: 20% Auto-correlation cut-off time profile (Data set 2)

C.2 20% Auto-correlation cut-off distance profile

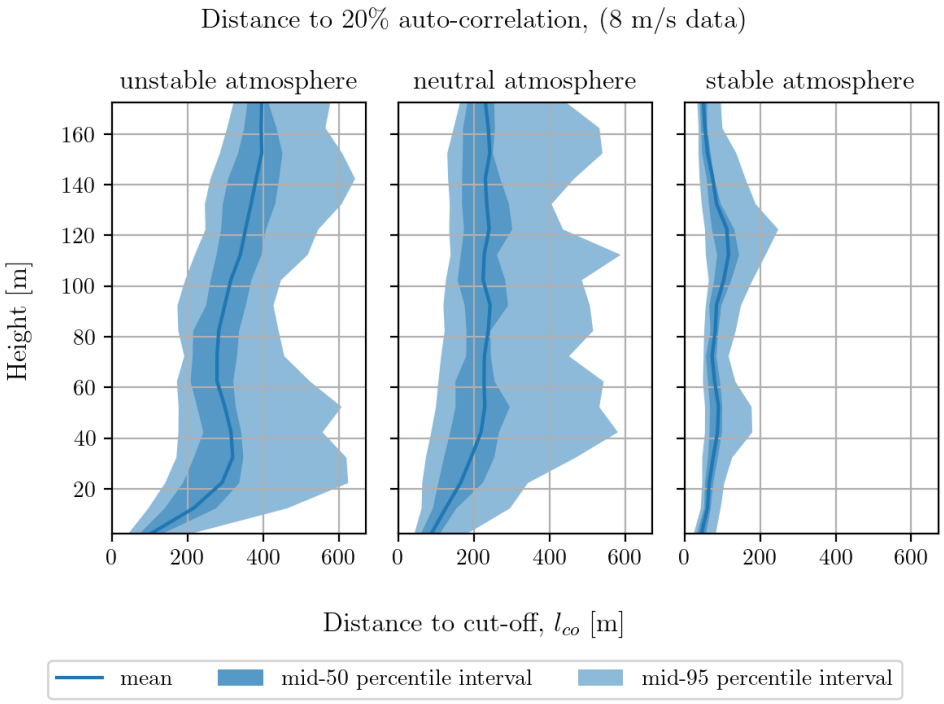

Figure C.3: 20% Auto-correlation cut-off distance profile (Data set 1)

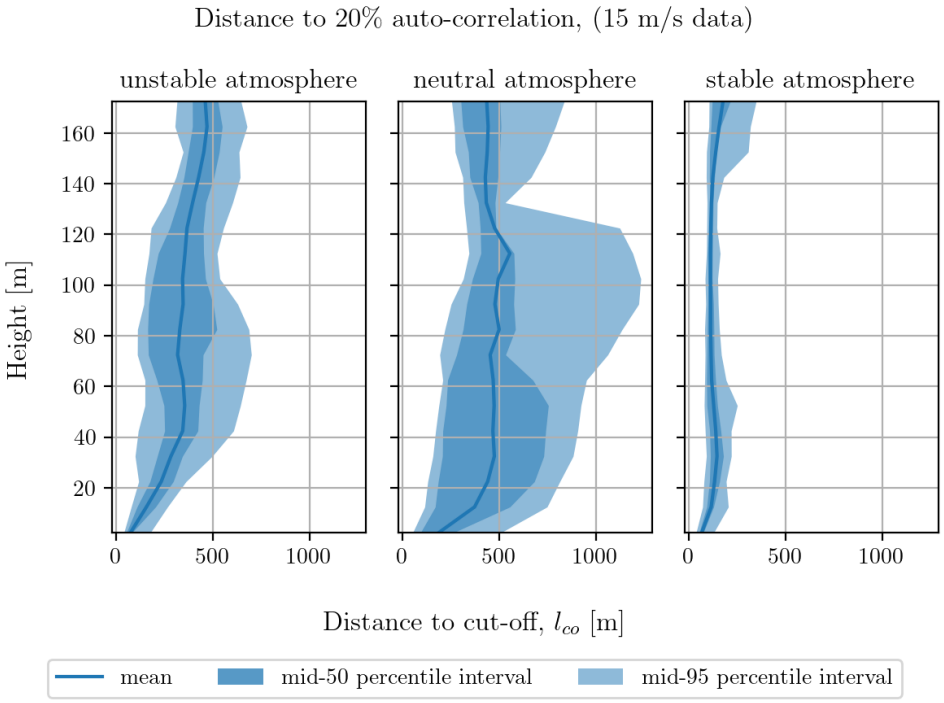

Figure C.4: 20% Auto-correlation cut-off distance profile (Data set 2)

C.3 Integral time scale profile

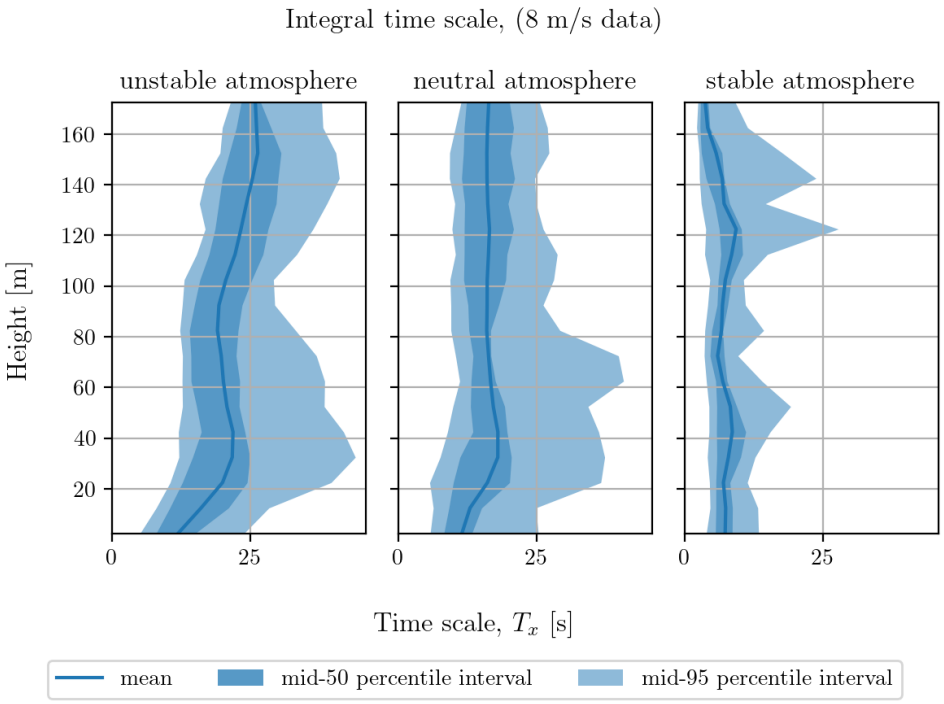

Figure C.5: Integral time scale profile (Data set 1)

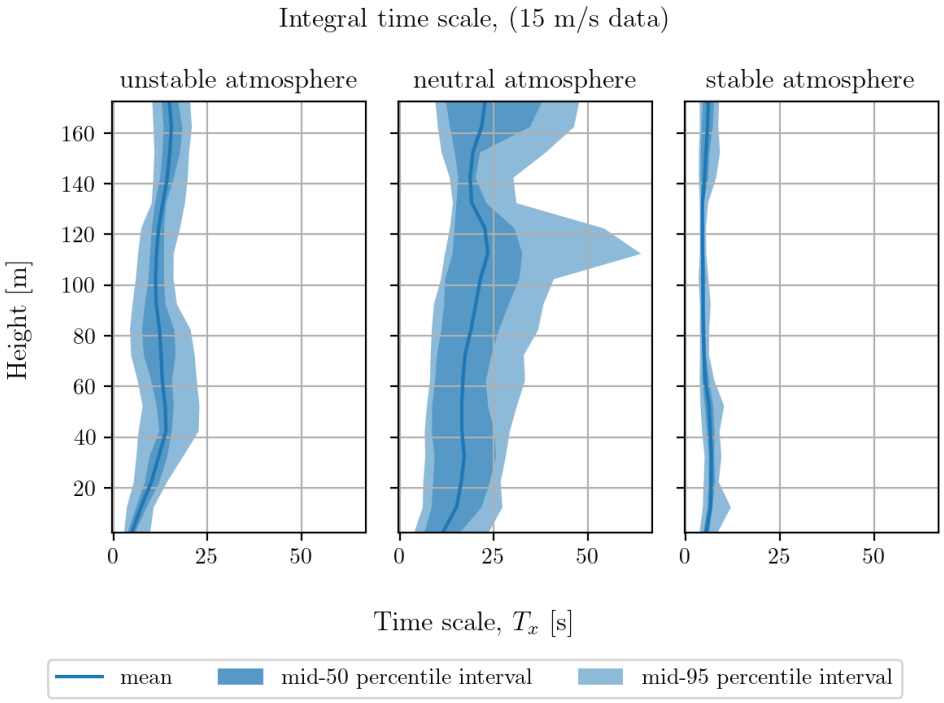

Figure C.6: Integral time scale profile (Data set 2)

C.4 Integral length scale profile

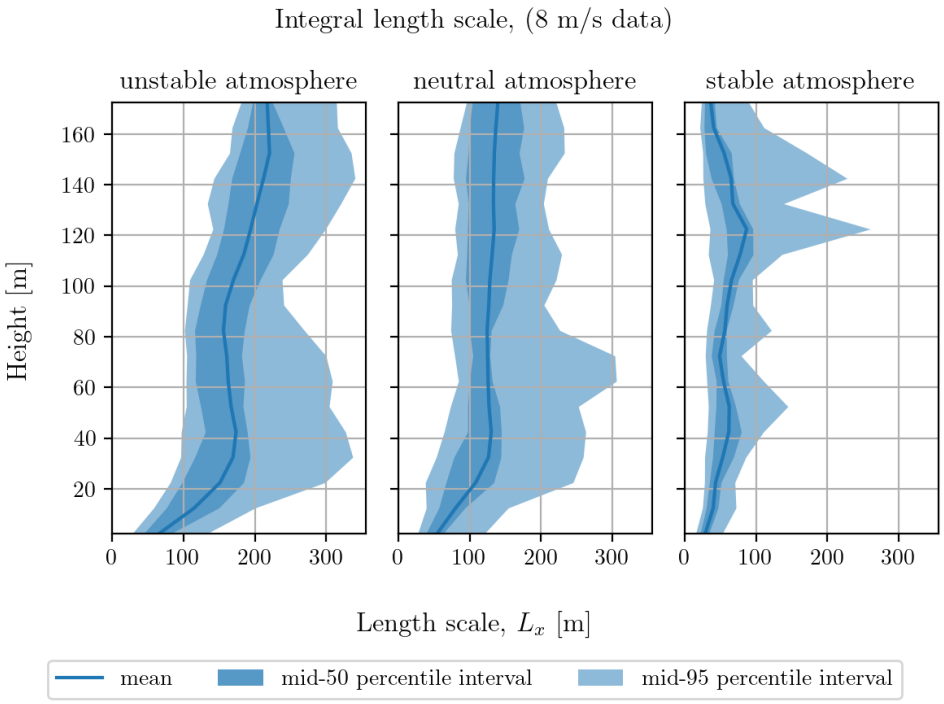

Figure C.7: Integral length scale profile (Data set 1)

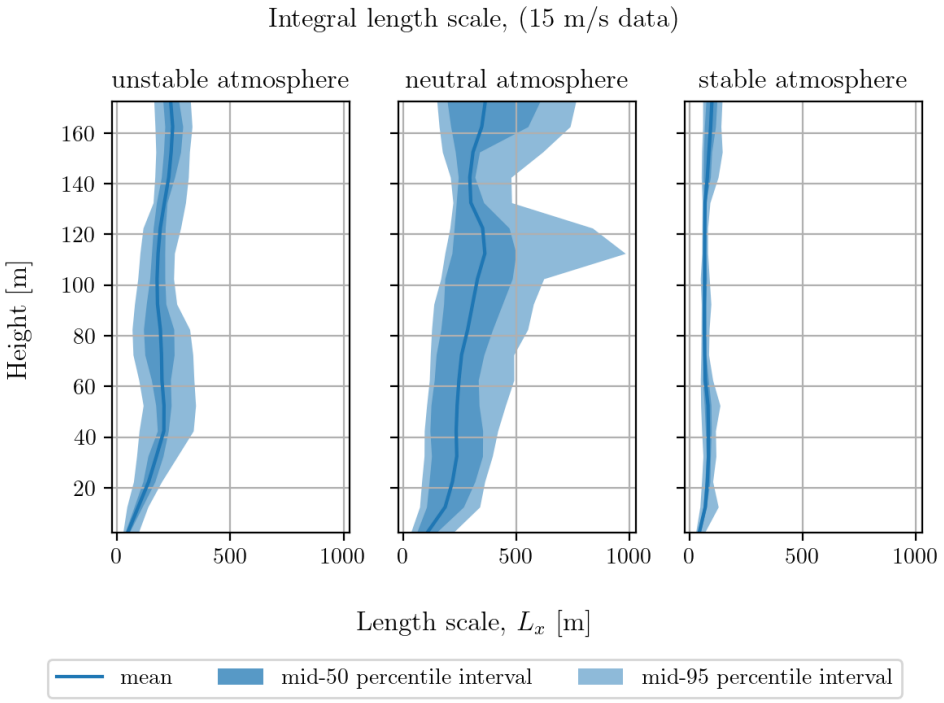

Figure C.8: Integral length scale profile (Data set 2)

C.5 Absolute delay difference

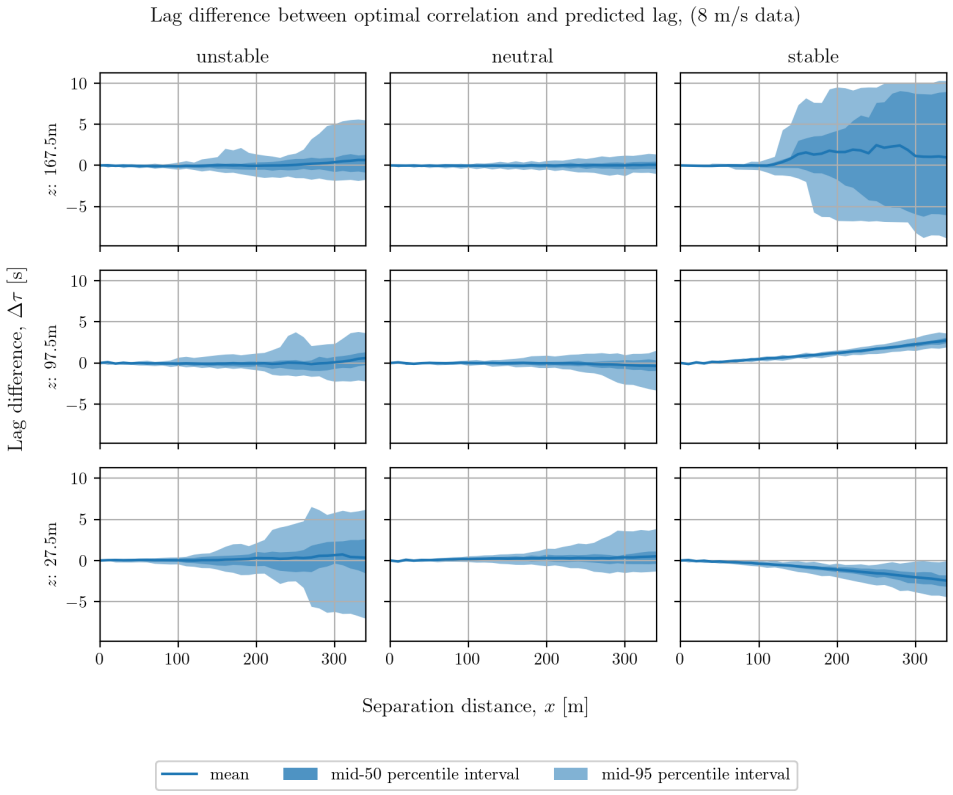

Figure C.9: Absolute delay difference between optimal and expected (Data set 1)

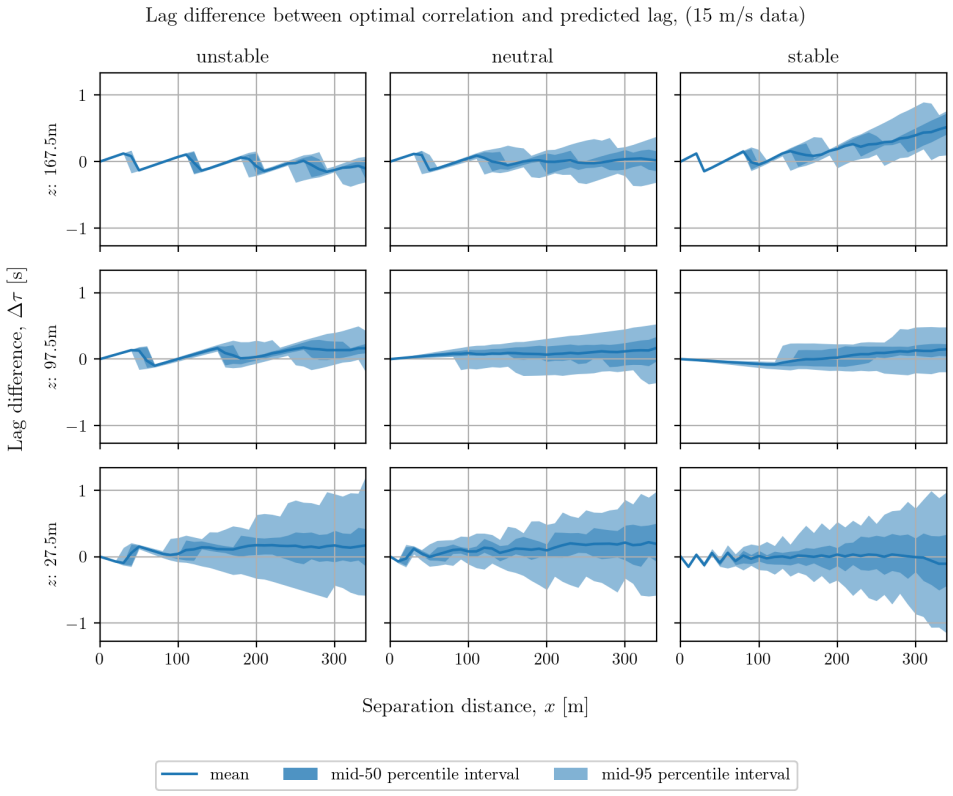

Figure C.10: Absolute delay difference between optimal and expected (Data set 2)

C.6 Longitudinal energy spectrum

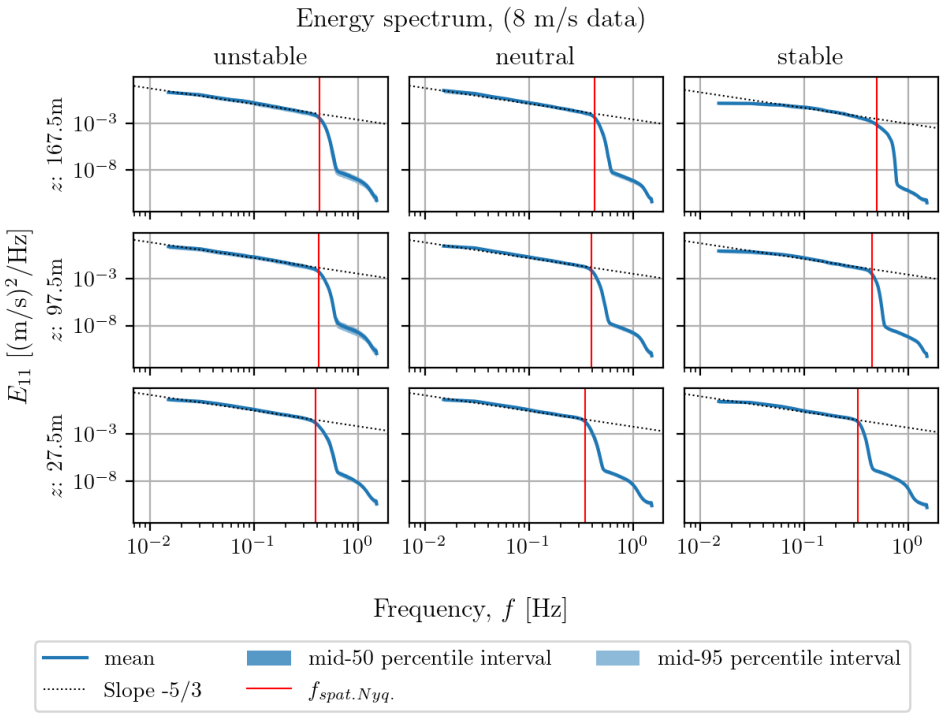

Figure C.11: Longitudinal energy spectrum in frequency (Data set 1)

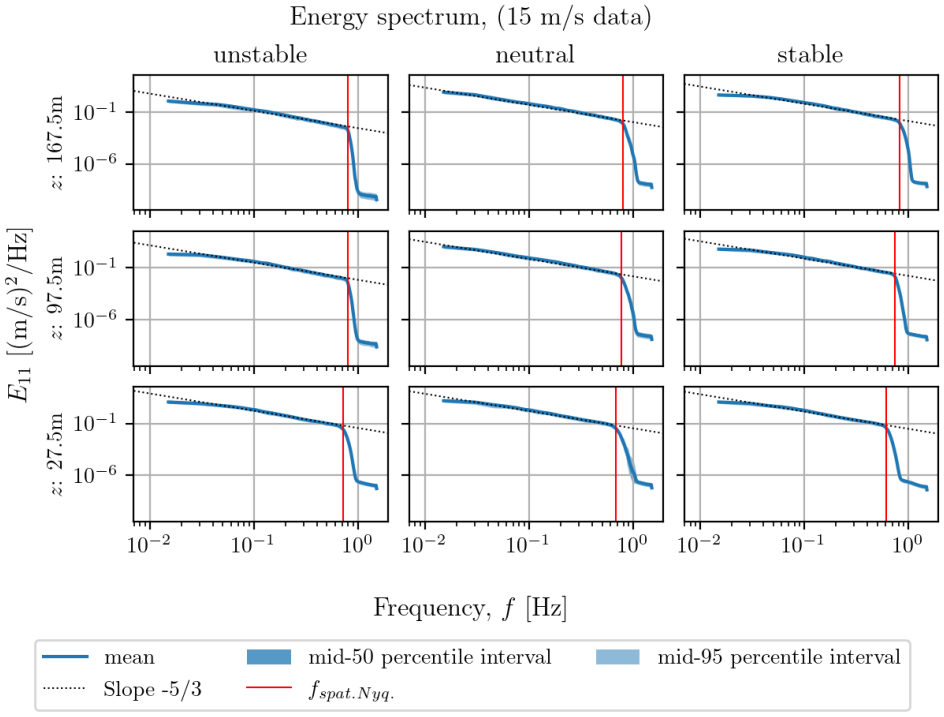

Figure C.12: Longitudinal energy spectrum in frequency (Data set 2)

C.7 Longitudinal magnitude-squared coherence (unstable atmosphere)

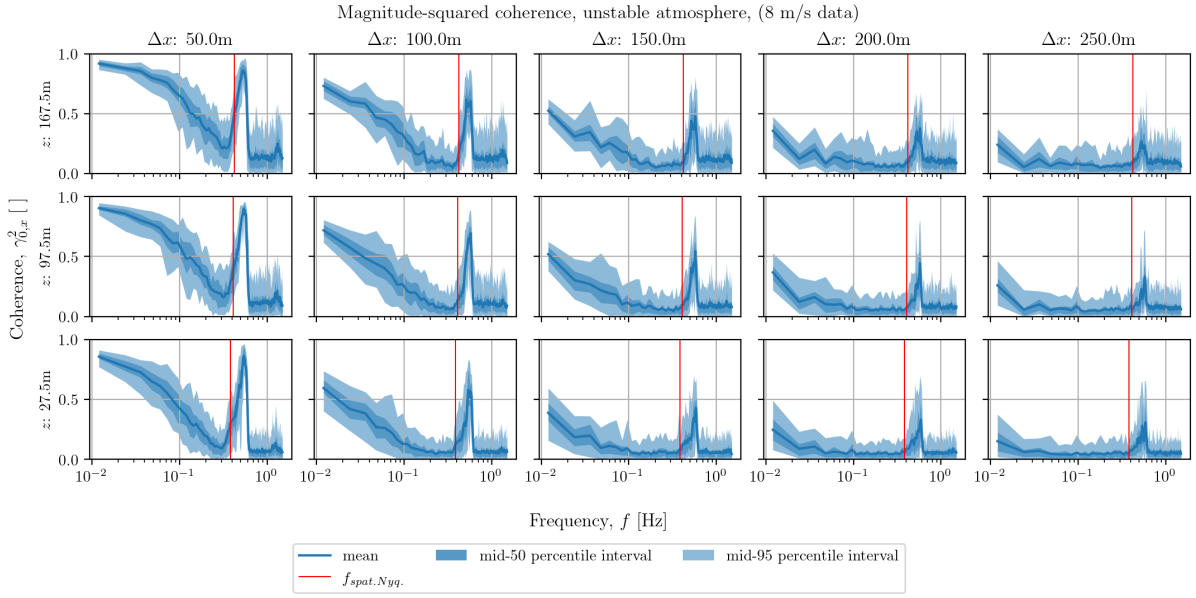

Figure C.13: Longitudinal magnitude-squared coherence in frequency, unstable atmosphere (Data set 1)

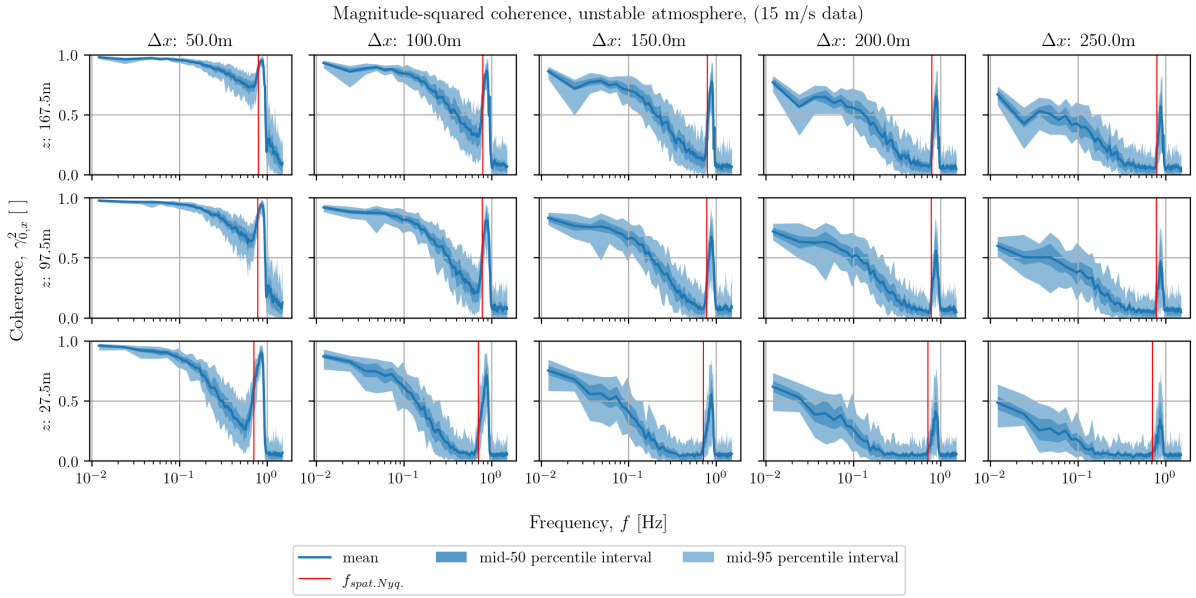

Figure C.14: Longitudinal magnitude-squared coherence in frequency, unstable atmosphere (Data set 2)

C.8 Longitudinal magnitude-squared coherence (neutral atmosphere)

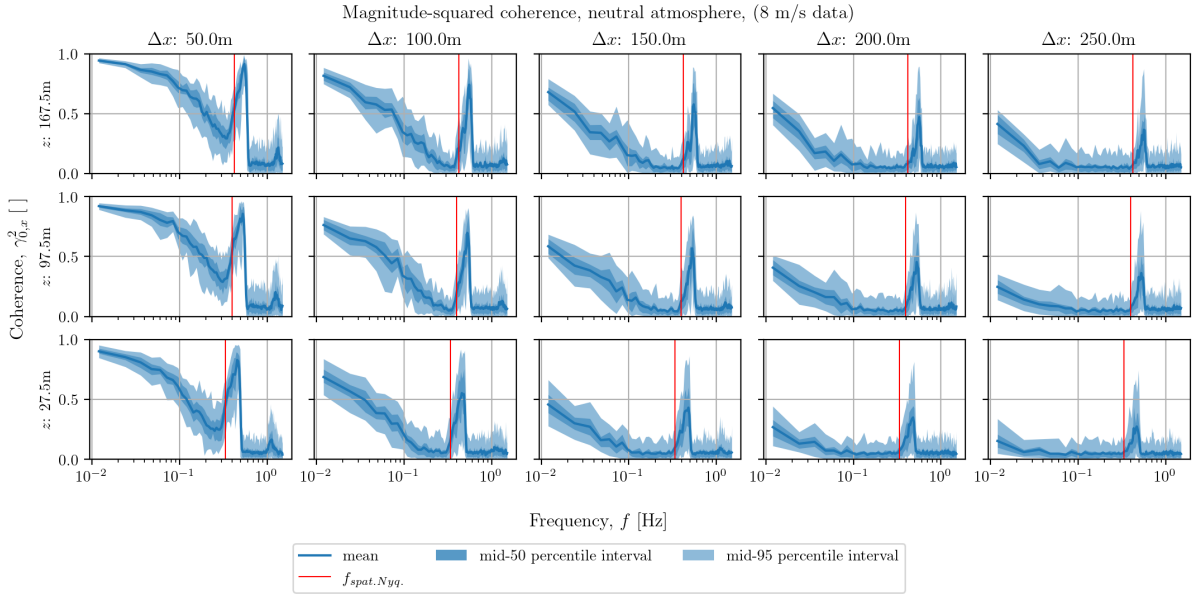

Figure C.15: Longitudinal magnitude-squared coherence in frequency, neutral atmosphere (Data set 1)

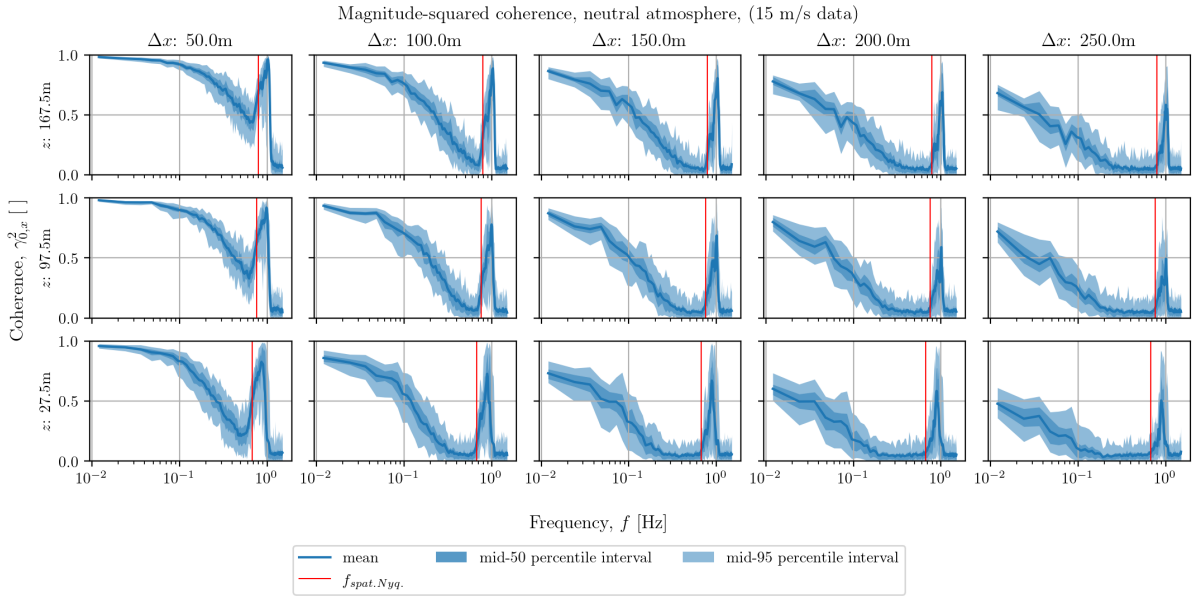

Figure C.16: Longitudinal magnitude-squared coherence in frequency, neutral atmosphere (Data set 2)

C.9 Longitudinal magnitude-squared coherence (stable atmosphere)

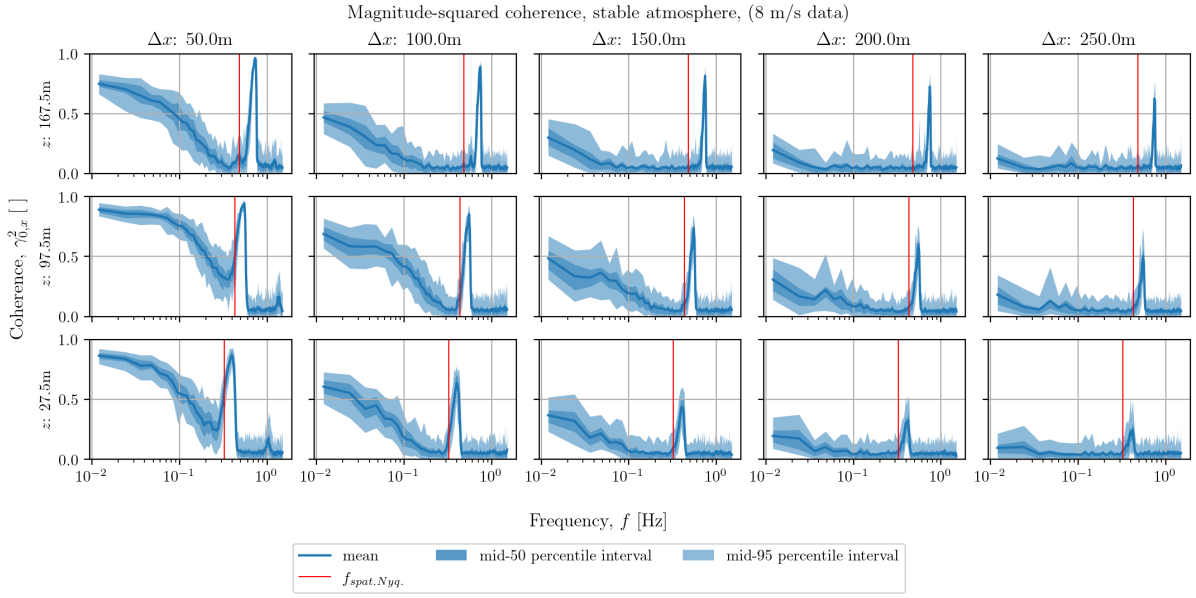

Figure C.17: Longitudinal magnitude-squared coherence in frequency, stable atmosphere (Data set 1)

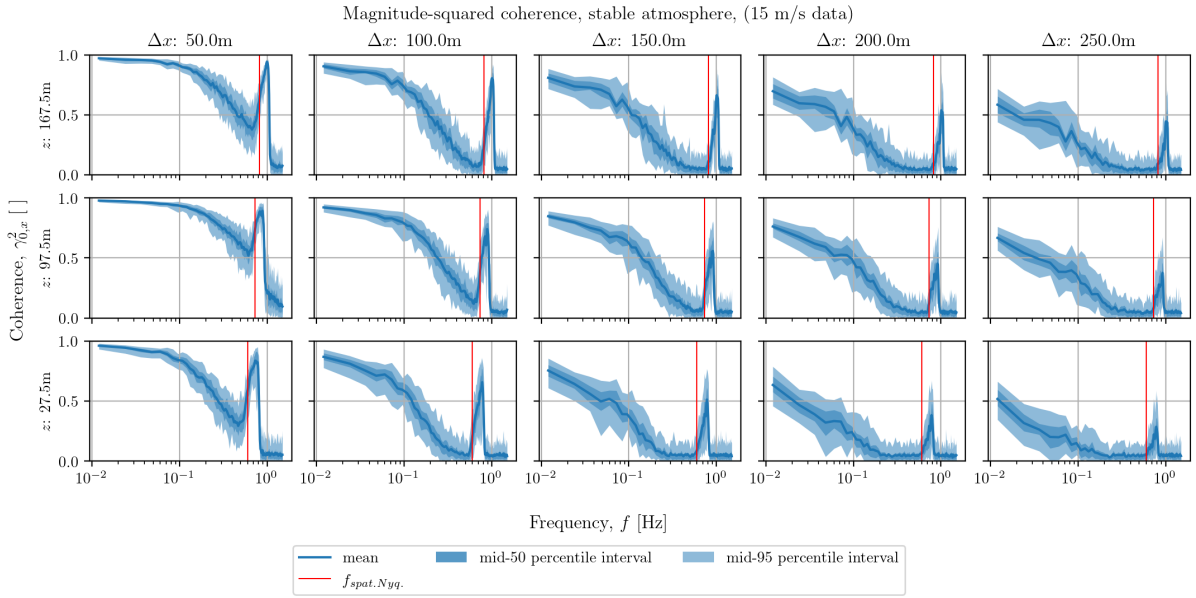

Figure C.18: Longitudinal magnitude-squared coherence in frequency, stable atmosphere (Data set 2)

C.10 Longitudinal phase delay (unstable atmosphere)

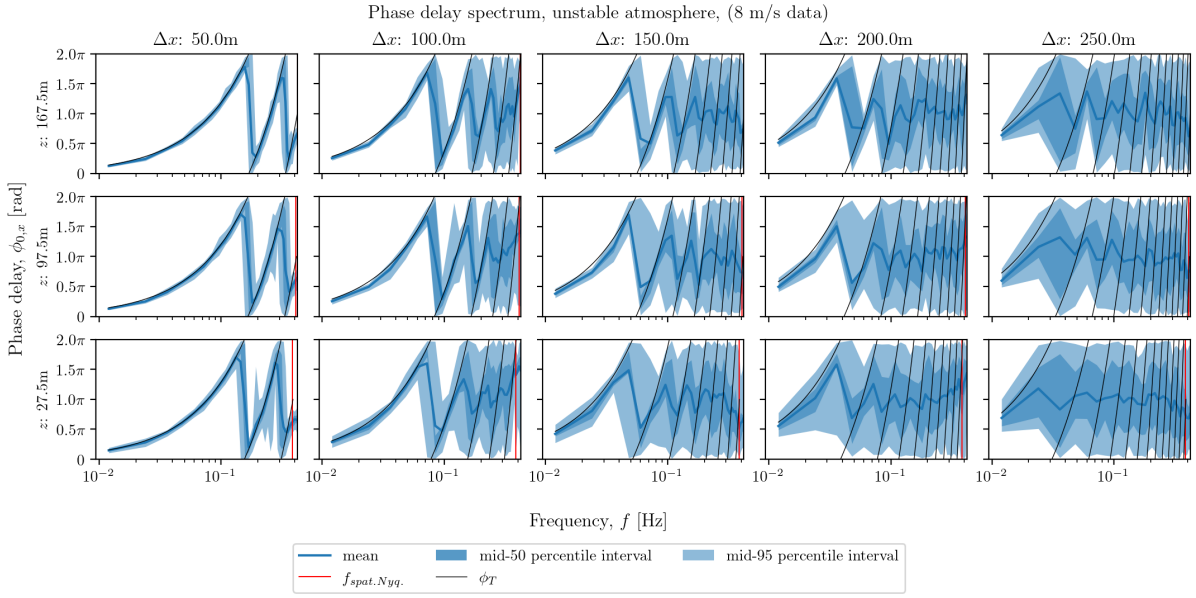

Figure C.19: Longitudinal phase delay, unstable atmosphere (Data set 1)

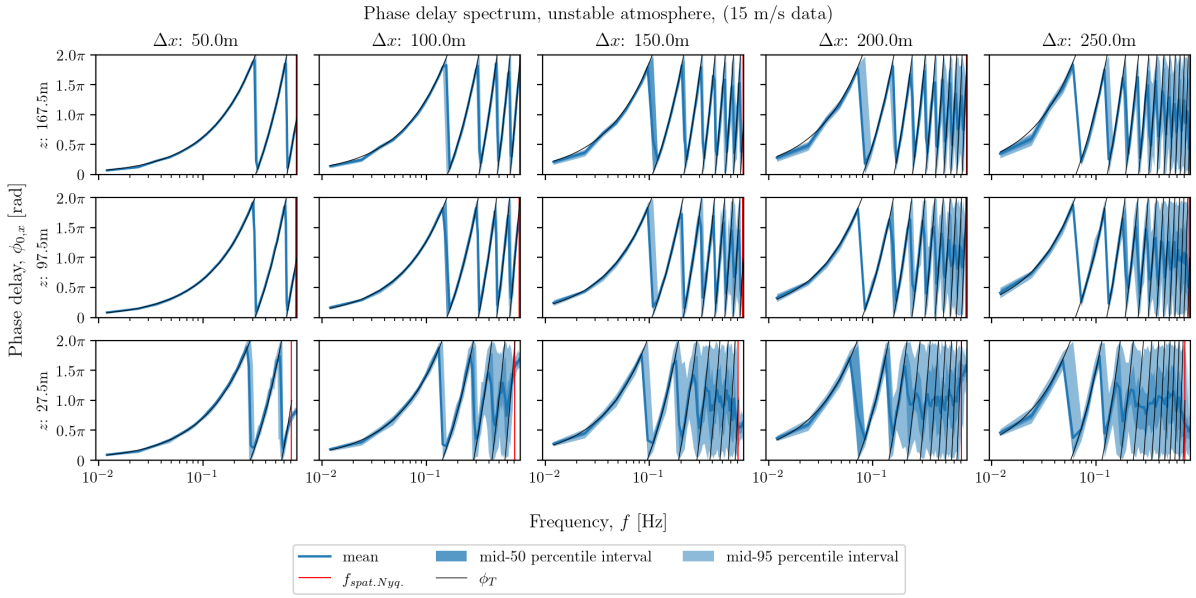

Figure C.20: Longitudinal phase delay, unstable atmosphere (Data set 2)

C.11 Longitudinal phase delay (neutral atmosphere)

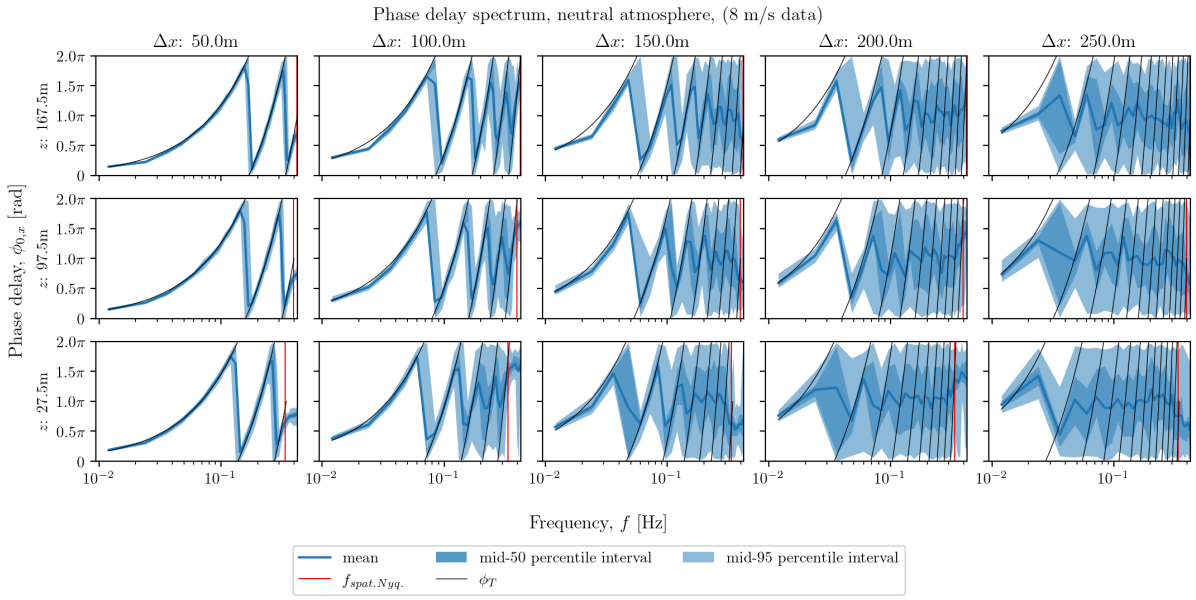

Figure C.21: Longitudinal phase delay, neutral atmosphere (Data set 1)

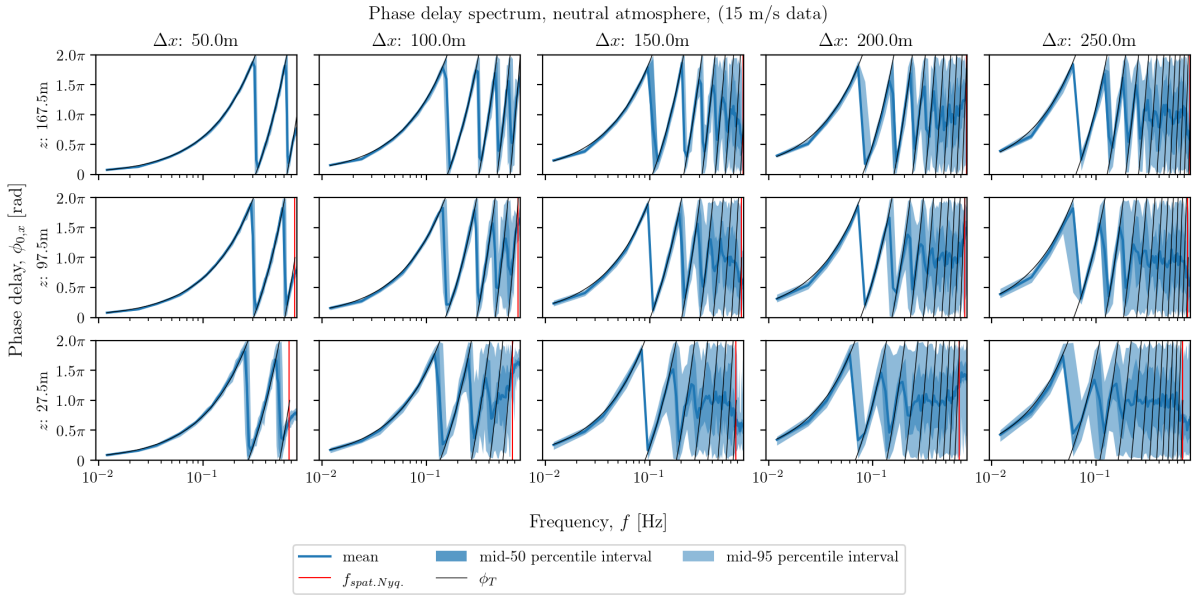

Figure C.22: Longitudinal phase delay, neutral atmosphere (Data set 2)

C.12 Longitudinal phase delay (stable atmosphere)

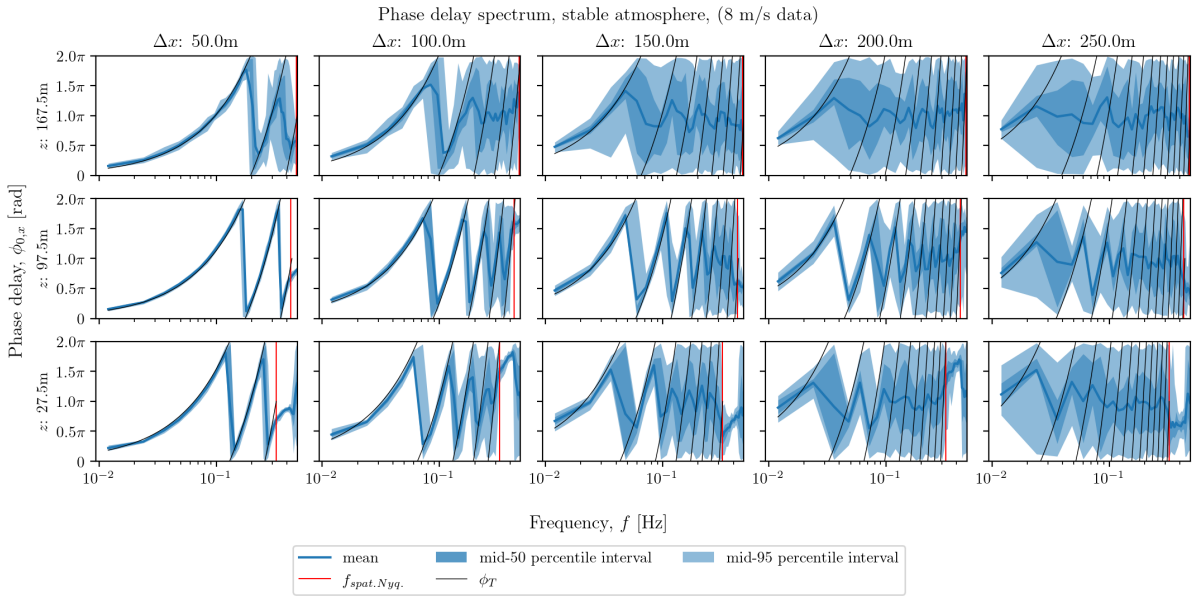

Figure C.23: Longitudinal phase delay, stable atmosphere (Data set 1)

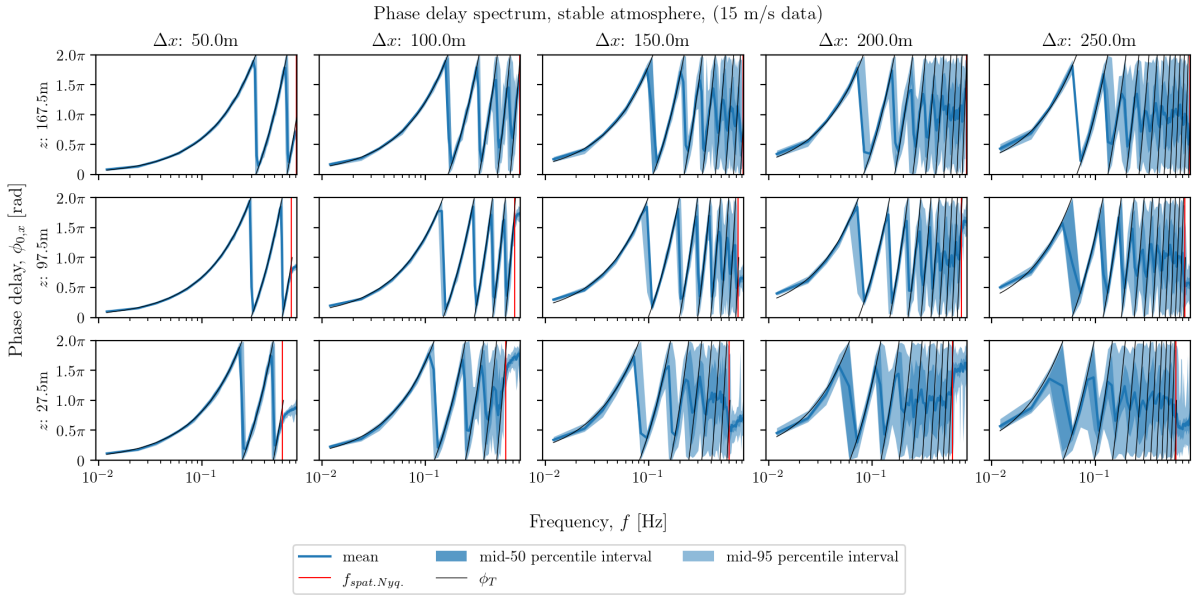

Figure C.24: Longitudinal phase delay, stable atmosphere (Data set 2)

C.13 Davenport decay parameters

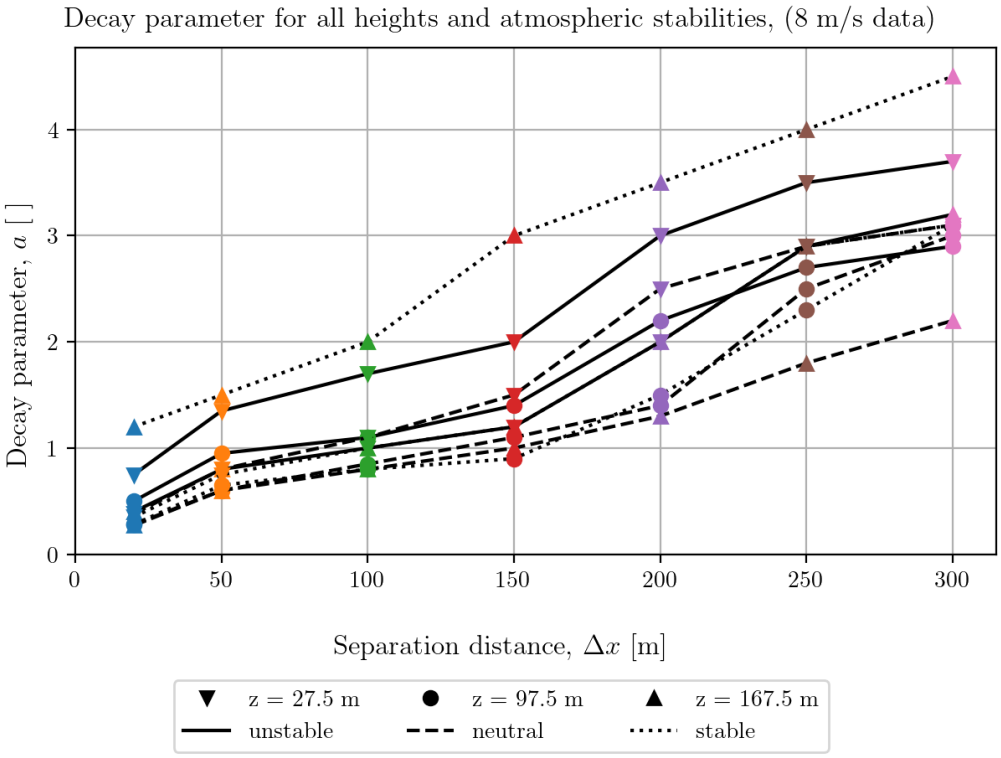

Figure C.25: Davenport decay parameter (Data set 1)

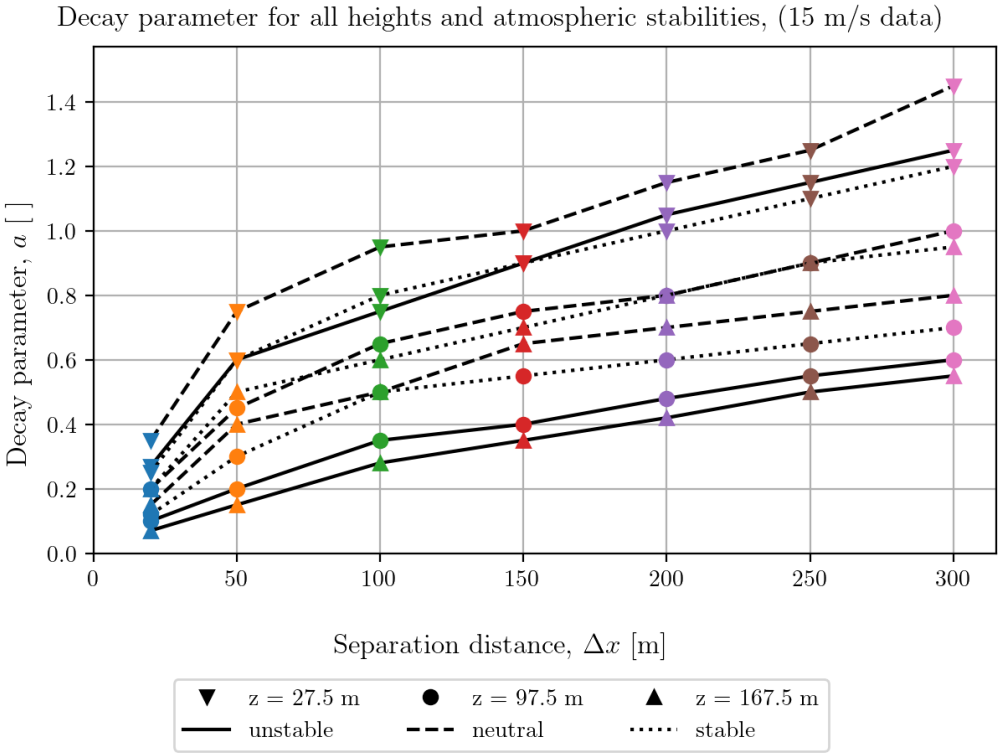

Figure C.26: Davenport decay parameter (Data set 2)